University of Alberta

Fabrication of Bragg Gratings in Silicon-On-Insulator Waveguides

by

Venkat Raghavan Subramanian ©

A thesis submitted to the Faculty of Graduate Studies and Research in partial fulfillment
of the requirements for the degree of *Master of Science*

Department of Electrical and Computer Engineering

Edmonton, Alberta

Fall 2002

Canada

University of Alberta

Library Release Form

Name of Author: Venkat Raghavan Subramanian

Title of Thesis: Fabrication of Bragg Gratings in Silicon-On-Insulator Waveguides

Degree: Master of Science

Year this Degree Granted: 2002

Permission is hereby granted to the University of Alberta Library to reproduce single copies of this thesis and to lend or sell such copies for private, scholarly or scientific research purposes only.

The author reserves all other publication and other rights in association with the copyright in the thesis, and except as herein before provided, neither the thesis nor any substantial portion thereof may be printed or otherwise reproduced in any material form whatever without the author's prior written permission.
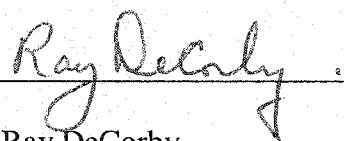
Venkat Raghavan Subramanian
407-114, Edinburgh Place
Saskatoon, Saskatchewan
Canada S7H 5J7

September 19th, 2002

University of Alberta

Faculty of Graduate Studies and Research

The undersigned certify that they have read, and recommend to the Faculty of Graduate Studies and Research for acceptance, a thesis entitled *Fabrication of Bragg Gratings in Silicon-On-Insulator Waveguides* submitted by *Venkat Raghavan Subramanian* in partial fulfillment of the requirements for the degree of *Master of Science*.

———————————————————
Dr. Ray DeCorby

———————————————————
Dr. Chris Backhouse

———————————————————
Dr. Rik Tykwinski

September 19ᵗʰ, 2002

FOR MY PARENTS

Abstract

A novel technique for the fabrication of Bragg gratings in rib waveguides on Silicon-On-Insulator (SOI) wafers was explored in this work. The rib waveguides were initially designed 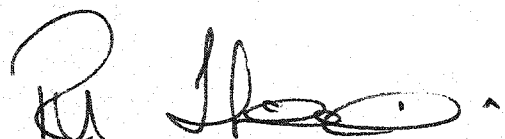to meet certain requirements for single-mode propagation in the waveguide, which was later verified using commercial softwares. The Bragg gratings are realized by changing the rib width along the length of the rib waveguide. Various simulations were carried out to study the performance of these Bragg gratings and the results were analyzed. Different techniques to improve and customize the spectral response of these gratings were explored by simulations. Simulations were also performed to study the effect of fabrication errors on the output characteristics of these gratings and it was found that very accurate fabrication is required to achieve the desired grating response.

A single prototype optical mask was designed incorporating different parameters of the waveguides and alignment marks for angular alignment of the grating pattern with the waveguides. The various fabrication processes of optical lithography, electron-beam (e-beam) lithography, liftoff and reactive ion etching (RIE) were tested and optimized for the fabrication of gratings and rib waveguides on SOI wafers. The optical lithography was used to pattern the waveguide and the e-beam lithography to pattern the grating sections. The RIE was used to create rib structures. It was found that inadequate control of the optical lithography resulted in rounding of square features. Also, the e-beam doses and resist thicknesses were also found to be very critical for the accurate definition of the grating pattern using e-beam lithography. Different etching recipes were studied and it

was found that the etching time and the amount of reactive gas for etching must be maintained at a minimal value to achieve good verticality and smooth sidewall features for both the gratings and the waveguides. Steam oxidation process was also explored as a means to smoothen the rough sidewalls that resulted from RIE. These results were encouraging, but require further study.

The rib waveguides fabricated were characterized using a fiber pigtailed 1550 nm laser and a 13 dB insertion loss was measured for an input power of 10.5 mW. Inefficient coupling between the optical fiber and the SOI waveguides was the major source of loss. This could be attributed to Fresnel loss, mode-mismatch loss, and scattering loss at the unpolished waveguide facets.

Due to unavailability of the e-beam lithography process during the final stages of this project, it was not possible to fabricate and test a completed waveguide Bragg grating.

Acknowledgements

Table of Contents

List of Figures

List of Tables

1. Introduction

1.1. Historical review

Communication of information has been essential for survival since life began on earth. The word *Telecommunication,* in the literal sense, means 'communication from a distance'. Light has always been a medium for telecommunication, even from the early stages of mankind. With the ever-increasing amount of knowledge and information in modern life, man has explored ways to efficiently and rapidly communicate information. Primitive methods of communications such as torches, heliograph, photophone [1], and blinker lights all had very low information carrying potential. Analog electrical and microwave communication systems are an improvement on the primitive techniques, but still suffer from limited signal bandwidth and considerable loss. The invention of the *laser* in 1960 as a radiation source suitable for use as a carrier of information and the *fiber optic cable* in mid 1970's as a medium to carry light signals with very minimal loss over longer distances, led to a major breakthrough in realizing high-capacity optical communication systems. Since those early days, the industry has come a long way; present day optical fibers having an astounding transmission rate capability of greater than Terabits (10^{12} bits) per second, as shown in Figure 1.1. As optical fibers have lowest loss in the 1.55 μm wavelength window, such wavelengths are used as carriers to transmit data over long distances.

1.2. Modern fiber communication technologies

As the demand placed on optical communications systems continues to grow, research strives to make full use of the information carrying potential of fiber networks. The need to feed more than one information channel through a single fiber led to the introduction of wavelength division multiplexed (WDM) networks, where information is transmitted simultaneously on multiple carriers with slightly different wavelengths.

1
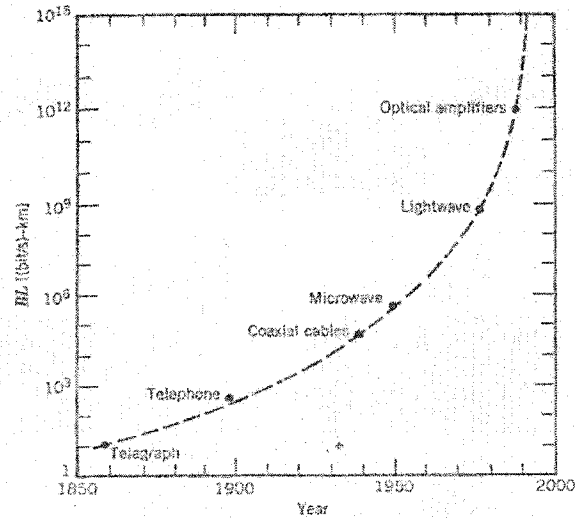
Figure 1.1: Improvement in transmission rate capability over the last century
(Source: [2])

Another major development, which led to the feasibility of long distance transmission without significant loss, was the invention of Erbium Doped Fiber Amplifiers (EDFAs). Prior to the availability of EDFAs, the signal transmitted through fibers had to be electrically regenerated every few kilometers (km) owing to the significant attenuation encountered during transmission. EDFAs for compensating fiber loss ($\approx$0.2 db/km) are widely used in long-distance optical networks, resulting in very low signal attenuation and link lengths on the order of 100 km. EDFAs operate in the wavelength range of 1520 nm to 1630 nm and can simultaneously amplify many wavelength division multiplexed signals carried by a single fiber in this range without causing them to interfere with each other. Thus, EDFAs and WDM are interdependent technologies.

Close on the heels of the invention of EDFA, it was demonstrated by Hill *et al.* in 1978 [3] that refractive index changes could be induced in the core of a fiber through exposure to an intense optical (ultraviolet (UV)) interference pattern. These periodic changes in the refractive index of the core along the length of the fiber are called Fiber Bragg Gratings (FBG) [3-8]. FBGs have found various key applications like filtering, routing and dispersion compensation of signals, thereby becoming one of the most important elements in WDM networks.

2

1.3. Need and advantages of optical and opto-electronic integrated circuits

An optical waveguide on a suitable substrate material is a structure that helps carry and couple signal from one fiber into another while simultaneously performing various operations on the transmitted signal like filtering, switching/routing, add/drop multiplexing, etc. Even though fiber-based devices performing the same functions are commercially available, they suffer from the drawback of not being suitable for mass-production and also being relatively expensive. Integration of such functionalities in optical waveguides provides us with the compatibility to develop active devices, allows flexibility of design, ruggedness, and reduced size and cost. Also, integrated optical circuits are capable of meeting future technological demands and are compatible with mass-production [9].

1.4. Grating devices

It was stated earlier that FBGs form an integral part of the present day optical networks, and are capable of performing various functions on optical signals carried by fibers. It was also mentioned that such devices are not ideal for mass production and are relatively expensive. Thus, researchers are seeking ways to integrate various functional devices on a single substrate. The advancement in modern microfabrication techniques and the growing awareness of the importance of integrated optics has certainly helped this cause.

Developing grating-based devices is one of the prime areas that many researchers across the globe have been working on for the past several years. Incorporation of such grating structures in integrated optical waveguides allows greater flexibility with the design and fabrication and is compatible with future optoelectronic integrated devices.

There are several different kinds of gratings commercially available, performing a wide range of functions. Integrated optical waveguides with such embedded grating structures have several potential applications within telecommunications networks. They can be

used to construct routers/switches, couplers, filters, add/drop multiplexers, dispersion compensators, mode converters, polarization converters, etc. This work is devoted to the investigation and development of Bragg gratings in Silicon-On-Insulator (SOI) waveguides, for use as optical filters in long-haul networks operating in the 1550 nm wavelength range.

1.5. Brief overview of telecommunication industry's growth

In order to emphasize the importance of this work, it is appropriate to look at the growth of telecommunication industry over the past couple of years. Though the industry is experiencing a slump in the last year, it is expected to rebound given the importance of telecommunications to human life.
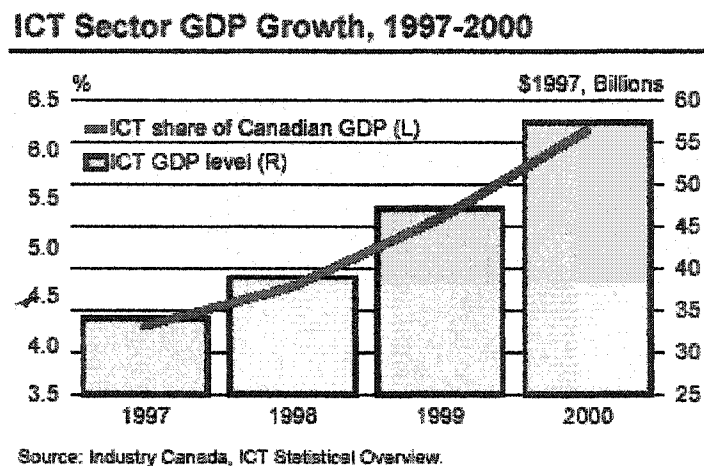
Figure 1.2: Chart showing ICT sector GDP growth over the last few years

The growth of the telecommunication industry has been phenomenal since the inception of lasers and optical fibers. An industry's growth can usually be judged by its contribution towards the country's economy and the number of new employment opportunities it creates. In the Information and Communications Technologies (ICT) sector, there has been tremendous annual growth over the past few years. From Industry Canada's statistical overview, the contribution of the ICT sector to the Canada's Gross Domestic Product (GDP) in the year 2000 (latest available figures) was a staggering $58 billion, which represents 6.2% of the total Canadian economy as seen from Figure 1.2.

This indeed is a great contribution from a single industry, considering there are hundreds of industries in Canada.

The ICT sector has also been a great source of employment and experienced a strong annual growth of 6.8% (as compared to the 2.1% economy-wide) for the years 1993-2000 (Figure 1.3).

ICT Sector Employment Growth, 1993-2000

Source: Industry Canada, ICT Statistical Overview.
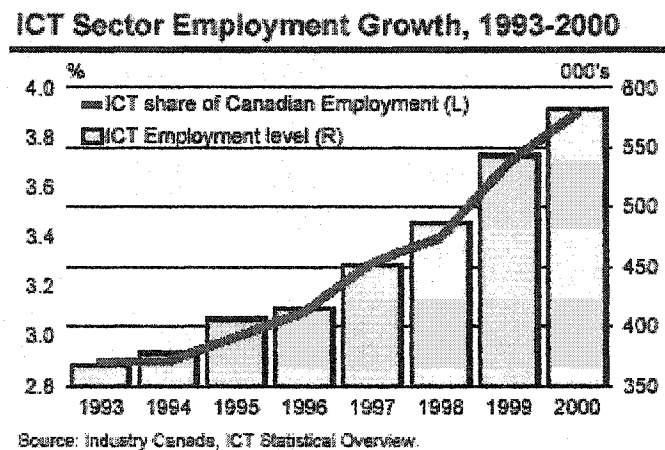
Figure 1.3: Chart showing ICT sector employment growth over the last few years

Distribution of R&D Expenditures by ICT Industry,
2001 Intentions ($5.3 Billion Total)
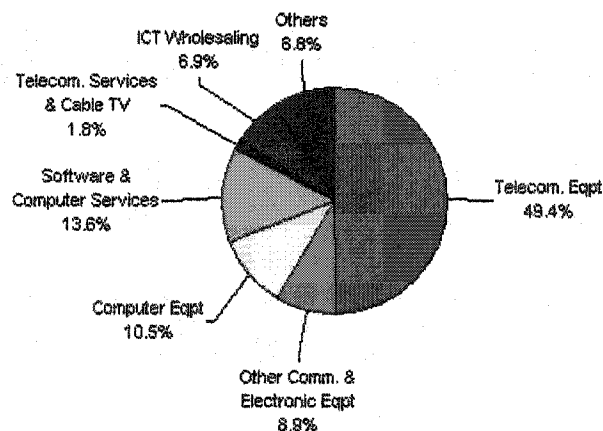
Figure 1.4: Chart showing the intended distribution of R & D expenditures for the year 2001

There has been a steady increase in the R & D expenditure of the ICT sector since 1993 and a closer look at the investment of the ICT sector in R & D for the year 2001 shows that it represented 45.8% of the total Canadian private sector R & D expenditure. Figure 1.4 shows that the telecommunication equipment industry was the largest spender on R & D, constituting almost half the total spending in the ICT sector.

These statistics reinforce the fact that the ICT industry is a huge contributor to Canada and a boon to the Canadian economy. This thesis work is a small contribution to this hugely important industry.

1.6. Thesis Outline

This work can be categorized into two segments, theoretical design and modeling (Chapter 3) and experimental work (Chapters 4,5).

Chapter 2 basically provides a brief literature survey of the existing technologies in making integrated optical devices and the motivation for the materials and technology investigated and used in this work. Different types of waveguide structures are discussed and the importance of rib waveguides in integrated optical devices is reviewed. An introduction to basic principles and theoretical analysis of Bragg gratings is presented and the significance of non-uniform Bragg gratings, especially Sampled Bragg gratings, for WDM networks is highlighted. A review of the different materials currently used in making integrated optic waveguides is provided and the advantages of SOI substrates are discussed. Finally the different technologies available to make grating devices are discussed and the advantages of the electron-beam (e-beam) lithography tool are outlined.

Chapter 3 deals with the design and modeling of the waveguide and grating structures. Initially, the single-mode condition for the rib waveguides is provided. It is then followed by the verification of single-mode existence for SOI rib waveguides using the effective index method (EIM). The spectral response characteristics for the grating devices were simulated using the transfer matrix method (TMM). Apodization

techniques to reduce 'noise' in the spectral response are simulated and discussed, as are the effects of fabrication errors.

In Chapter 4, design of an optical lithography mask and various fabrication techniques and processes for realizing SOI rib waveguides and gratings are discussed. In particular, the e-beam lithography used for patterning gratings is discussed in detail. A simple technique to integrate optical lithography and e-beam lithography is proposed. Some techniques to smoothen the rough sidewalls of waveguides formed by dry etching were studied and the results are analyzed.

The optical characterization of the SOI rib waveguides for different rib widths and two different lengths is described in Chapter 5. The coupling and propagation losses in these waveguides are shown and discussed.

Finally, a conclusion of this overall work and some recommendations for future work is presented in Chapter 6.

2. Background details and literature survey

This chapter provides a brief description of the different types of waveguides, substrate materials and technologies available for integrated optics. The advantages and disadvantages of each are discussed and the reasons and motivation for our choice of material and technology in this work is provided.

2.1 Rib waveguides

Integrated optics requires optical fields to be confined in the lateral directions of X and Y (with Z assigned as the direction of propagation of a guided mode). Such *channel waveguides* are realized on a planar substrate and are very much compatible with planar processing technology borrowed from the microelectronics industry. Some of the general structures providing 2-dimensional confinement of light and realized using the standard thin film and microfabrication techniques are: 1) General channel waveguide 2) Buried channel 3) Raised strip 4) Rib guide 5) Embedded strip 6) Ridge guide. These are shown in Figure 2.1, where n_f, n_c, and n_s are the core, upper cladding and lower (substrate) cladding indices. All of the structures are very similar (with very few modifications in geometry) and produce very similar modal behavior. Functional devices in channel waveguides are usually only a couple of centimeters long and hence dispersion, which is important for long distance propagation in optical fibers, is no longer an issue. Many such short functional structures can be integrated on a single substrate.

The buried waveguides are usually obtained by making some material modification, such as in-diffusing another material into the substrate to obtain an index contrast. However, the index change obtained by this method is very small [12-14]. This results in poor optical confinement and power loss into the cladding whenever the waveguide is curved.

With the above limitation in mind, the strip, ridge and rib structures are often used in integrated optics, mainly due to the ease of making such step index structures by patterning and etching. Here, the total internal reflection takes place at the sides of the

guide, as well as from the top and bottom faces. Much higher field confinement is possible when using a large index contrast waveguide and hence can be bent more tightly without suffering from excessive radiation loss.
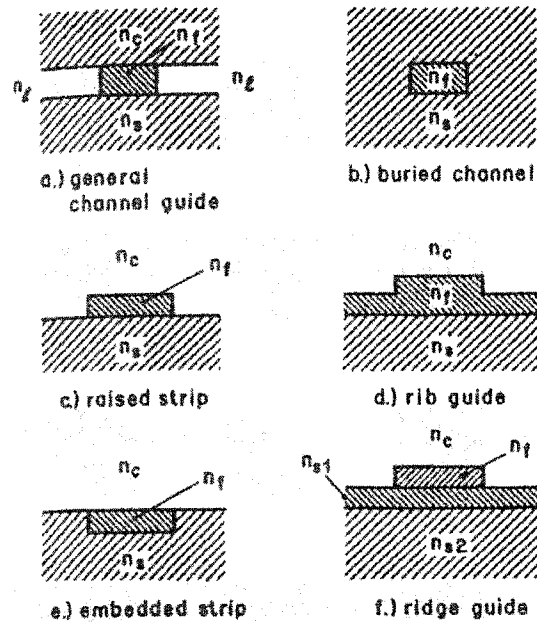
Figure 2.1: General waveguide structures for 2-D light confinement (Source: [11])

A rib waveguide is just an extension of the ridge waveguide where the ridge is not etched the full way down to the substrate. Guiding in the direction transverse to the plane of the layer is due to the effective index offset between the rib and the etched regions adjacent to the rib. The rib is a very widely used structure in integrated optics because of its capability to support and maintain single-mode condition even for large waveguide cross sections [15]. This helps in better coupling between the waveguide and a fiber or laser source, thus resulting in low coupling loss. The modal field in the rib waveguide can also be made to match that of a fiber quite well, in terms of the overall shape and dimension of the mode, by proper tuning of the refractive indices.

2.2 Bragg Gratings - Basic Principles

Waveguide Bragg gratings are reflection grating filters that produce contra-directional coupling between forward and backward modes. These gratings can be made by periodically changing the refractive index in the core of the waveguide, such as through exposure to a holographic interference pattern. Alternately, they can be realized by etching a periodic corrugation on the surface of the waveguide. In these structures, the Bragg effect causes coupling of energy from the forward traveling mode into the backward traveling mode. The corrugation or periodic index modulation in the core acts as a weak mirror that reflects a particular wavelength. When all the reflection from a number of periods of index modulation add constructively in phase, the entire energy in a particular mode can be coupled into the reflected mode. The optical path for one period is $n_{eff}\Lambda$, where Λ is the period of the gratings and n_{eff} is the effective refractive index in the core for a particular mode. For each of the components reflected from every corrugation to add in phase with each other, the optical path must be an integer number of half the optical wavelength. Thus, the equation for first order Bragg reflection is of the form:

$$2\,n_{eff}\Lambda = \lambda_0 \tag{2.1}$$

and the grating vector is given by:

$$K = \frac{2\pi}{\Lambda} \tag{2.2}$$

where λ_0 is the first-order Bragg wavelength and n_{eff} is the guided mode effective index.

When the Bragg condition is satisfied, the magnitude of the grating vector is twice the propagation constant as given by:

$$K = 2\beta, \tag{2.3}$$

where β is the propagation constant of the guided mode and is equal to $\dfrac{2\pi n_{eff}}{\lambda_0}$.

2.2.1 Theoretical analysis of Bragg grating filters

Analysis of Bragg reflection gratings is done here by using scalar coupled-mode theory [16]. The analysis is based on the assumption that the guide is single-moded. The forward propagating mode $E_y(x, y, z) = E(x, y)\exp(-i\beta z)$ and the backward propagating mode $E_y(x, y, z) = E(x, y)\exp(+i\beta z)$ both satisfy the wave equation (2.4) [11]:

$$\frac{\partial^2 \psi}{\partial x^2} + \frac{\partial^2 \psi}{\partial y^2} + [k_0^2 n^2(x, y) - \beta^2]\psi = 0. \tag{2.4}$$

The periodic index change $\partial n(x, y, z)$, is defined by a periodic function as given by [16]:

$$\partial n(x, y, z) = \Delta n(x, y)\cos(Kz), \tag{2.5}$$

where $\Delta n(x, y)$ represents the index perturbation in the transverse direction and the periodicity of the grating along the z direction is given by the cosine term in equation (2.5). The scalar wave equation is given by [16]:

$$\nabla^2 E_y(x, y, z) + [n(x, y) + \partial n(x, y, z)]^2 k_0^2 E_y(x, y, z) = 0. \tag{2.6}$$

Assuming small perturbation, (2.6) can be approximated as:

$$\nabla^2 E_y + [n^2 + 2n\partial n]k_0^2 E_y = 0 \tag{2.7}$$

At the Bragg condition, $K \approx 2\beta$, the solution to equation (2.7) can be written as a sum of the forward travelling and reflected mode in the form [16]:

$$E_y(x, y, z) = A_F(z)E(x, y)\exp(-i\beta z) + A_R(z)E(x, y)\exp[-i(\beta - K)z] \tag{2.8}$$

where A_F and A_R are amplitudes of the forward propagating and reflected mode, respectively.

Neglecting second order derivatives of A_F and A_R (as they vary slowly) and also the higher diffraction orders of the gratings, (2.8) can be written in the form:

$$\{-2i\beta\frac{dA_F}{dz}\exp(-i\beta z)-[2i(\beta-K)\frac{dA_R}{dz}+[(\beta-K)^2-\beta^2]A_R]\exp[-i(\beta-K)z]+$$
$$n\Delta n k_0^2[A_F\exp(-i(\beta-K)z)]+A_R\exp(-i\beta z)]\}E=0 \tag{2.9}$$

Equation (2.9) holds for the entire length of the grating when the exponential terms vanish. After equating the coefficients of the exponential terms to zero and applying the approximation, $\beta-K/2=\Delta\beta$, the resultant coupled differential equations are integrated over the entire section of the waveguide. The result is:

$$dA_F/dz+i\kappa A_R=0$$
$$dA_R/dz-i2\Delta\beta A_R-i\kappa A_F=0 \tag{2.10}$$

Equation (2.10) represents the coupled-mode equations where the rate of change of the amplitude of forward and backward propagating modes depend on the amplitude of the other mode and is related by the coupling coefficient κ given by:

$$\kappa=(k_0^2/2\beta)\left(\iint n\Delta n E\bullet Edxdy\right)/\frac{1}{2\eta}\left(\iint E\bullet Edxdy\right) \tag{2.11}$$

It is seen that the coupling coefficient, κ, is dependent on the overlap between the transverse electric field E and the index perturbation Δn. If the index perturbation created by the corrugations is low, then it requires that a longer grating section be defined to get a stronger reflection.

2.3 Platforms for integrated optics

Silica waveguides [17-20] have been used extensively for planar waveguide technology until now because of their low propagation loss (0.1 dB/cm) and low coupling loss to fiber (0.1 dB/chip). To realize waveguides in silica glass, a thick cladding layer is required to totally confine light inside the waveguide. Silica waveguide structures are

usually grown by chemical vapor deposition (CVD) or flame hydrolysis [21]. However, growing of such thick cladding layers usually results in high amount of stress being accumulated that could effectively bend the wafer, induce Polarization Dependent Loss (PDL) or even scattering loss. Techniques for reducing such stress and PDL have been discussed in the literature [22-26].

Of late, polymers have been explored extensively for use in integrated optical circuits. Again, a number of applications have been reported in the literature for use of polymers in lasers [27], switches [28-30], and filters [28-34]. Even though these polymer devices offer potential for low cost and have highly tunable optical properties, they still suffer from processing difficulties and poor stability.

Silicon oxynitride (SiON) [35] has also been recently explored for use as an alternative to silica technology for making planar waveguides. It offers reasonably high refractive index contrast (~0.5-0.6) when compared to silica waveguides resulting in strong confinement and smaller bend radius, as discussed in Section 2.1. Some of the devices realized on SiON materials are filters [36, 37], switches [38], attenuators [39].

Lithium niobate [40, 41] has been used extensively for active device fabrication because of its high electro-optic and acousto-optic coefficients. However, waveguides on Lithium niobate substrates are realized by indiffusion and typically offer very low refractive index contrast.

Indium Phosphide [42-44] and Gallium Arsenide [45-47] based semiconductors have been used extensively in optical communication for the manufacture of both active and passive devices.

In recent years, Silicon-On-Insulator (SOI) has been explored as an alternative to the Silica-on-Silicon technology. This is a very critical material as it bridges the well-established microfabrication techniques on Si with future optoelectronic integrated devices [48,49]. It offers a very high refractive index contrast (n_{Si} = 3.5, n_{SiO2} = 1.5).

This helps in strong optical confinement and thus makes it possible to have smaller waveguide components and tighter bend radii. As with SiON, ribs are highly recommended structures for SOI waveguides because of the high index contrast. With rib structure, fairly large cross-sectional waveguides could be formed on SOI with propagation loss as low as 0.1 dB/cm [50], while maintaining single-mode propagation. Large rib cross-sections reduce the coupling loss between the waveguide and the fiber (source). A detailed discussion on how the single-mode condition is achieved and maintained on rib structures will be given in Chapter 3. These waveguides on SOI substrates are of great importance to integrated optics. Researchers have shown that phase-arrayed demultiplexers [51], interferometers [52] and couplers [53] could be realized on SOI substrates. However, the area of formation of Bragg gratings on SOI substrates has been left relatively unexplored.

Even though there are several advantages of this material, some technologies involved with SOI formation result in non-uniform Si overlayer, which can affect optical properties of waveguide devices. Several technologies for SOI formation have been reported so far. The three main technologies are:

1. Separation by implanted oxygen (SIMOX) [54]

2. Bond-and-Etchback SOI (BESOI) [55]

3. Smart cut process [56].

The various steps involved in each of the technologies are shown in the Table 2.1 [57].

SOI		
SIMOX	**BESOI**	**Smart Cut**
1) Oxygen ion implantation on pure Si 2) High temperature annealing	1) Oxidation of Si wafer 2) Hydrophilic bonding with pure Si 3) Annealing 4) Polishing	1) Hydrogen ion implantation on SiO_2 2) Hydrophilic bonding to Si 3) Heat treatment 4) Polishing

Table 2.1: Steps involved with SOI fabrication

Of the three processes, Smart Cut yields the best quality Si layer with greater uniformity when compared to the BESOI. Moreover, a wide-range of thickness of Si overlayer can be obtained by varying the Hydrogen implantation in the Smart cut process. It is desired that voids in the Si layer and in the bonding (of the oxide layer) should be minimal as they could induce scattering loss in waveguides formed on them.

The optical properties of all the materials discussed above are tabulated in Table 2.2 [59].

2.4 Techniques of grating formation

Fiber Bragg gratings are the typical waveguide gratings and were first demonstrated by Hill *et al.* [4]. They were formed as a result of photosensitive characteristics of the fiber, whereby a periodic index modulation could be induced along the length of the fiber using a coherent ultraviolet light source of high intensity launched into the fiber core [4, 60]. This technique of 'internal writing', however, produced Bragg wavelengths close to the visible range and did not provide much control over the index modulations realized.

Almost a decade later, it was shown by Meltz *et al.* [61] that gratings could be realized as a result of interference caused by two intersecting UV light beams, irradiated from the sides of the core rather than by launching intense visible light through the core of the fiber. This technique of transverse holography was highly flexible in terms of controlling the magnitude of index modulation in the core of the fiber and the period of the grating. Index modulation is dependent on several factors, such as the wavelength of the UV light source, intensity, exposure time, and photosensitivity of the fiber core [62, 63]. Furthermore, the Bragg grating period is controlled simply by the angle of the interfering UV beams. It does not necessitate the removal of the fiber cladding, as the cladding is relatively transparent to UV radiation and also because of the high Germanium (Ge) concentration in the core, which in turn leads to high refractive index contrast. In spite of all these advantages of this technique over internal writing, it is a fairly complex set up, requires careful alignment, is sensitive to vibrations of the apparatus, and is not compatible with mass production.

15

Material	Propagation Loss (dB/cm)	Fiber Coupling Loss (dB/chip)	Refractive Index (n)	Typical core-cladding index offset (Δn) in waveguide	Typical Thermo-Optic Coefficient dn/dT (K^{-1})	Maximum Modulation Frequency/ Switching speed
Silica [SiO_2]	0.1	0.5	1.44-1.47	0-1.5% (Channel)	10^{-5}	$\approx$1 kHz (T/O)
Silicon [Si] (Silicon-On-Insulator etc)	0.1	1.0	3.4757	70%[range=0] (SOI Rib)	1.8×10^{-4}	$\approx$1 kHz (T/O)
Silicon Oxynitride [SiO_xN_y]	0.1	1.0	SiO_2: 1.44-1.47 Si_3N_4: 1.9905	0-30% (Si_3N_4 core, SiO_2 clad)	10^{-5}	$\approx$1 kHz (T/O)
Sol-Gel glasses	0.1	0.5	1.2-1.47	0-1.5% (Channel)	10^{-5}	$\approx$1 kHz (T/O)
Polymers	0.1	0.5	1.3-1.7	0-35% (Channel)	$-1 - -4 \times 10^{-4}$	>100 GHz (E/O) 1 kHz (T/O)
Lithium Niobate [$LiNbO_3$]	0.5	2.0	n_0=2.2125 n_e=2.2137	0-0.5% (Channel)	10^{-5}	$\approx$ 40 GHz (E/O)
Indium Phosphide [InP]	3	10	3.1	0-3% (Channel)	0.8×10^{-4}	$\approx$ 40 GHz (E/O)
Gallium Arsenide [GaAs]	0.5	2.0	3.3737	0-14% (Rib)	2.5×10^{-4}	20 GHz (E/O)

Table 2.2: Typical optical properties of some key material systems at 1550 nm wavelength [59]

In order to overcome the limitations of the two methods discussed above, a new technique of Bragg grating formation using a diffractive element called a p*hase mask* was proposed in the early 90's [64]. Figure 2.2 describes the formation of Bragg gratings using phase masks. Phase masks are periodic surface relief structures varying in a single dimension formed on glass substrates. Gratings are imprinted onto fibers and waveguides by placing the phase masks in close proximity to the fiber/substrate and illuminating it with UV light. The phase masks diffract this incident light into three distinct orders, namely, 0, +1 and -1. The interference of the two first order diffractions are responsible for the grating formation and the zeroth order is usually suppressed because of its deleterious effects on the grating characteristics, as discussed elsewhere [65]. By controlling the depth of the surface relief in the phase mask, the zeroth order could be reduced to as low as 1%. Each phase mask is designed for specific grating periods and suppression of the zeroth order is customized for a single UV illumination wavelength. This technique did eliminate most of the limitations imposed by the holographic method by yielding a high throughput and also allowed flexibility to introduce chirp and aperiodicity in the period. But, it still had a major drawback in not being flexible with the different Bragg wavelengths, i.e., a single phase mask could be used to form Bragg gratings for just a single wavelength.
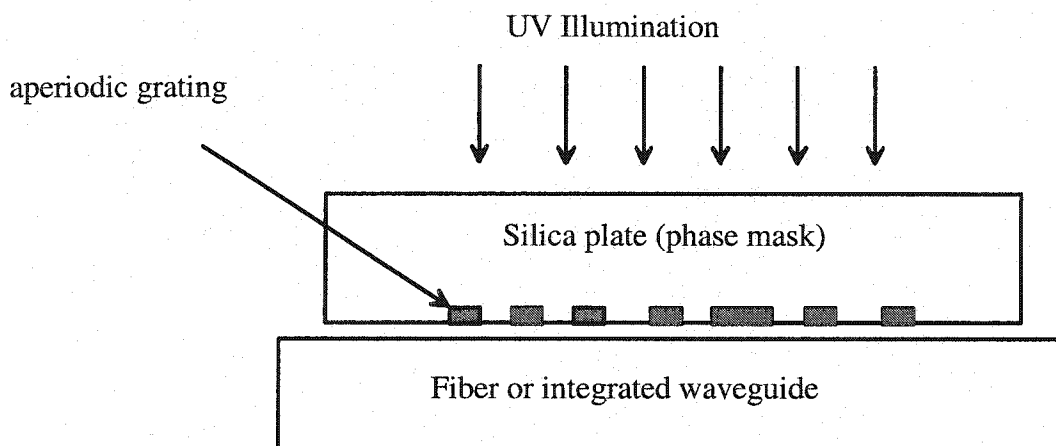
Figure 2.2: Schematic showing the formation of Bragg gratings using phase masks

When using silicon waveguides ($n_{eff} \approx 3.5$), Bragg gratings have smaller periods of ~ 200 nm for operation around the 1550 nm wavelength range. Also, it is of absolute importance in these grating structures that there be strict control of the grating periods for its application to filtering as will be shown by some simulation results in Chapter 3. Such high accuracy with small periods is very difficult to obtain using the techniques discussed earlier. A more flexible and highly accurate lithography tool, Electron-beam (E-beam) lithography, is more suited for the fabrication of such small grating periods. However, E-beam lithography does introduce stitching errors since it is only possible to write continuous fields on the order of ~100 μm^2. A single uniform Bragg grating typically needs to be several hundred microns long to act as a good mirror (with nearly 100% reflection at the Bragg wavelength). Such length makes it necessary to stitch together a number of e-beam fields. As the performance of these Bragg gratings relies heavily on the phase coherence of the light propagating through the device, it is of absolute importance that the e-beam fields are stitched with very high accuracy. It has been shown elsewhere [66] that error as small as 5 nm can introduce several unwanted effects in the filter responses. In spite of the handicap of stitching errors and non-compatibility with bulk production, e-beam lithography is still the state-of-art and highest accuracy lithography tool.

It is clear from the discussions above that Bragg gratings in integrated SOI waveguides would have many attractive features. Our work is focused on methods to form rib waveguides and sampled grating structures on SOI substrates using e-beam lithography.

3. Device Design and Modeling

In this chapter, the design of waveguide and grating structures on SOI substrates will be presented. Also, simulation results of these waveguides and gratings and study of their spectral response characteristics will be discussed. An analysis of various techniques to reduce 'noise' in the spectral response and the effects of fabrication errors is also included.

3.1 Design of Single-mode waveguides

3.1.1 Single-mode requirement

The goal of this work is to explore methods to fabricate grating devices to be used in WDM networks for long-haul transmission. Multi-mode transmission in such devices is a serious problem as the different modes could interfere with each other resulting in an uneven distribution of light at the end of the waveguide in what is called modal 'noise' or 'crosstalk'. Moreover, the grating filter devices we study here depend on phase coherence of the reflected wavelengths from each of the corrugations as seen from the principles of the Bragg gratings in Chapter 2. This phase coherence can be seriously affected by the modal 'noise' that arises as a result of multi-mode propagation. Thus it is required that just the fundamental (lowest order) mode be supported by these waveguide devices.

3.1.2 Single-mode condition for rib waveguides

It was believed that rib waveguides fabricated on SOI with larger cross section would in general be multi-moded due to the large refractive index contrast ($n_{Si} \approx 3.5$, $n_{SiO2} \approx 1.5$). It was however, first shown by Soref *et al.* [15] that they could be made to support just one single (lowest order) mode by carefully defining the height and width of the rib section to satisfy the following two conditions [15]:

$$\frac{w}{H} \leq 0.3 + \frac{r}{\sqrt{1-r^2}}$$

$$r = \frac{h}{H}, \ 0.5 \leq r \leq 0.9$$

(3.1)

where $'w'$ is the width of the rib section, $'H'$ is the height of the rib section, and $'h'$ height of the slab section outside the rib as shown in Figure 3.1. The upper limit of 0.9 in equation (3.1) is chosen as a practical fabrication limit for achieving some lateral confinement. However, the theoretical condition for single-mode existence is $0.5 \leq r < 1$. Such a change in confinement from the typically multi-moded waveguide into one supporting just the fundamental mode is explained in terms of the effective refractive index [15, 67]. When the above two conditions are satisfied, the higher order modes in the horizontal direction are not guided in the rib because of the sufficiently small rib widths. Even though the rib might be multi-moded in the vertical direction initially, satisfying equation (3.1) ensures that the effective indices of the higher-order vertical modes are less than the effective indices of the slab modes outside the rib. Thus, the higher order modes will leak into the slab region as radiation modes, and only the fundamental vertical mode in the rib remains confined.
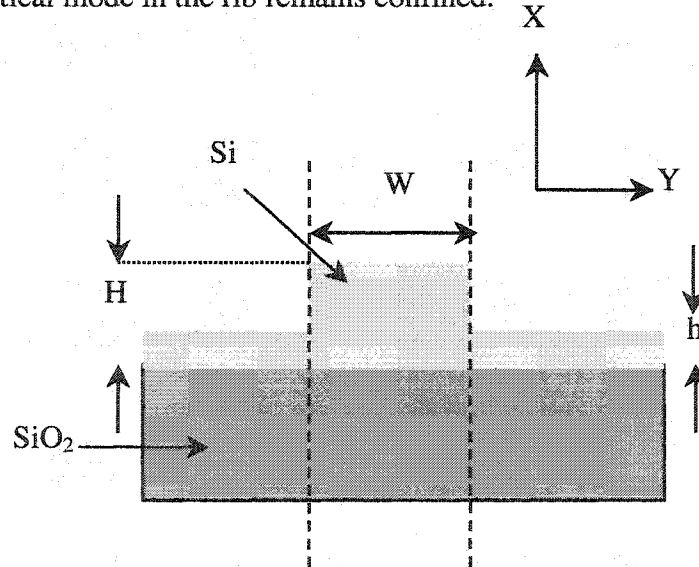
Figure 3.1: Schematic of a SOI rib waveguide

3.13 Choice of silicon thickness in SOI wafers

Two different SOI wafers were obtained for this work, as outlined in Table 3.1:

Diameter	Handle thickness (Substrate)	Buried oxide	Device thickness (Upper Si layer)	Non-uniformity (Device layer)
100 mm	525 µm	1.0 µm	1.5 µm	± 5% µm
100 mm	500 µm	1.0 µm	3.0 µm	± 0.1-0.2 µm

Table 3.1: SOI wafer specifications (Source: [68, 69])

It could be seen that with an increase in thickness of the device layer, the non-uniformity increases. Also, the amount of voids in the Si layer increases with higher thicknesses, as was mentioned in Chapter 2 while discussing the merits of SOI fabrication.

It is necessary that the non-uniformity of the Si layer be as small as possible. Non-uniformity could affect the single-mode criteria when the etch depth is shallow and very close to the upper limit or deep and close to the lower limit of $\dfrac{h}{H}$, as could be seen from the following Table 3.2:

Device thickness (Si layer) (µm)	Etch depth (µm)	$\dfrac{h}{H}$	
3.0	0.3	0.9	Chosen as a practical limit for fabrication
3.0	1.5	0.5	
2.9	1.5	0.483	$\dfrac{h}{H}$ value outside the limits of single-mode condition

Table 3.2: Table showing the effects of Si layer non-uniformity on the single-mode condition

It is seen from Table 3.2 that when the Si layer thickness increases or decreases by ± 0.1 μm as a result of (unknown) non-uniformity introduced during fabrication of SOI, etching to the same depth as for uniform Si layer can change the $\dfrac{h}{H}$ to a value outside the limit for the existence of the single-mode condition. This can be avoided by choosing $\dfrac{h}{H}$ values that are not near the endpoints.

3.1.4 Verification of Single-mode condition

A Beam Propagation Method (BPM) simulation using a commercial software package (BeamPROP) was done to verify the confinement of just the fundamental mode in the rib SOI waveguide when the single-mode conditions are satisfied. The simulation was done for a SOI waveguide with Si thickness of 1.5 μm, width 'w' of the rib of 3.0 μm and $\dfrac{h}{H} =$ 0.9 and a circular mode was used to launch power into the waveguide. The simulation result is shown in Figure 3.2.

It is seen from the transverse mode profile of the plot that the fundamental mode is very much confined in the rib section. All of the power carried by the mode (shown by the red circle) is shown to be confined under the rib.

When checked for higher order mode existence, it is seen from Figure 3.3 that the first order modes leak out of the rib section (shown by the blue rectangle in the center) as radiation modes into the slab regions. The effective refractive indices of the fundamental and the first order modes from the plots in Figures 3.2 and 3.3 are found to be 3.465378 and 3.461155, respectively. As was mentioned earlier, it is this small difference in the effective refractive index that is responsible for the radiation of the higher order modes out of the rib.
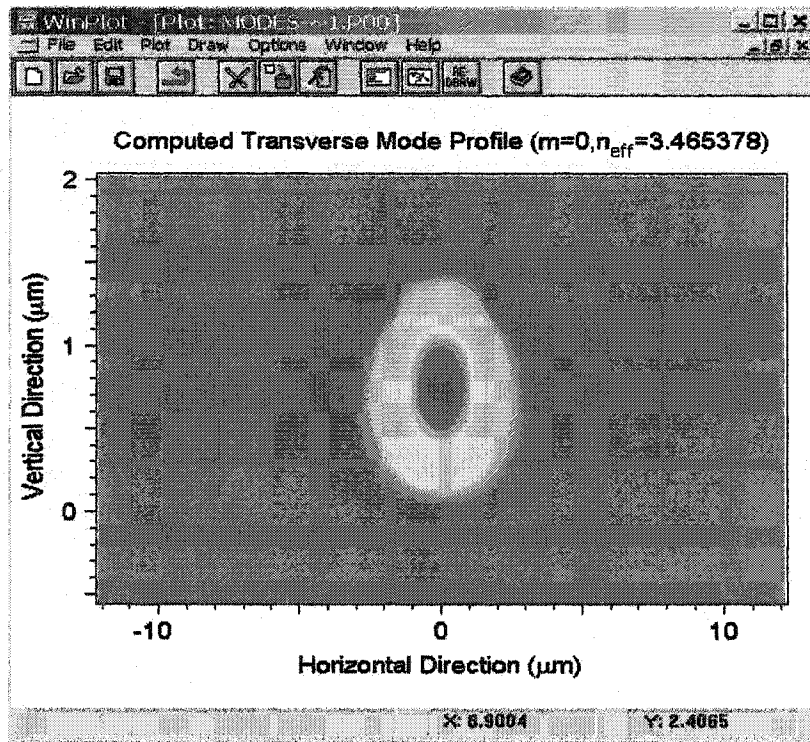
Figure 3.2: Verification of fundamental mode confinement
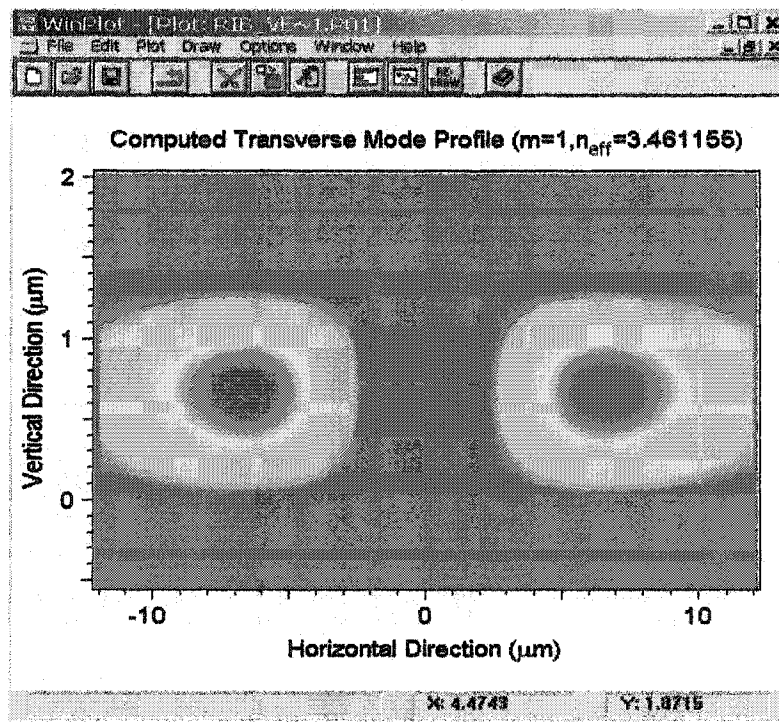
Figure 3.3: Higher order radiation modes
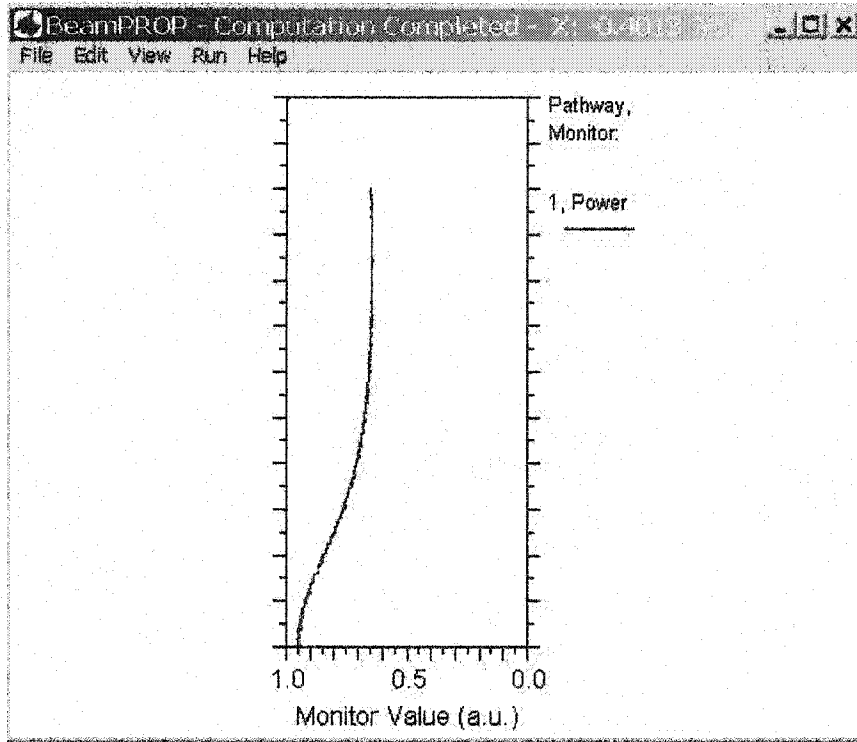
Figure 3.4: Power confinement in the fundamental mode

To estimate waveguide loss due to radiation of higher order modes, the power in the waveguide is monitored as shown in Figure 3.4. The initial higher power in the waveguide and the subsequent loss is because of the higher order modes that exists initially, but radiate out over a distance. After propagating a certain distance, the power in the waveguide levels out. This power in the waveguide is just the power carried by the fundamental mode.

More simulations were carried out using another commercial BPM software (PROMETHEUS) to check for confinement of energy for different lengths of the SOI rib waveguide and the results are shown in Figure 3.5 and Figure 3.6.
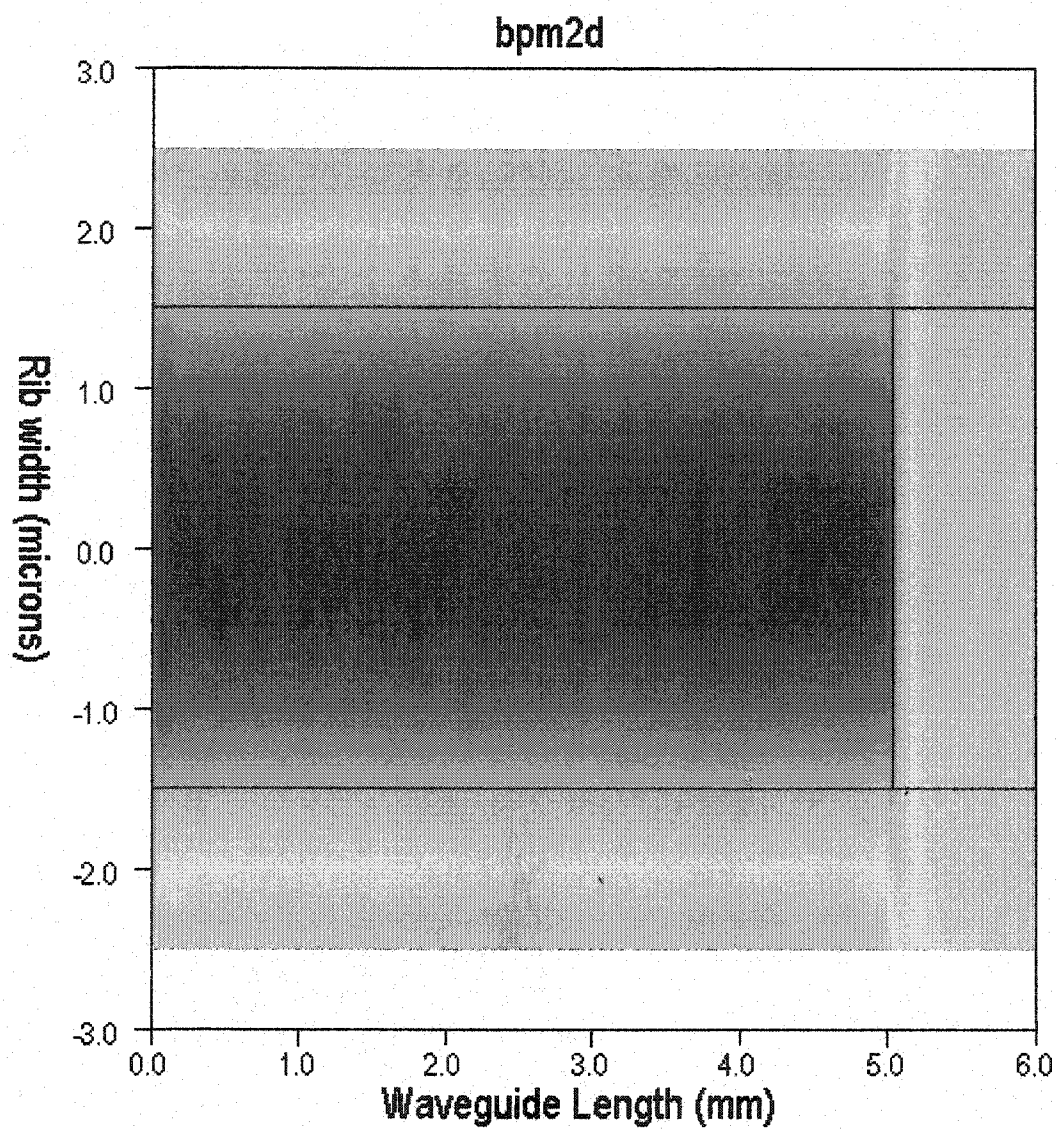
Figure 3.5: BPM simulation to study confinement of energy for a 5 mm long waveguide with a rib width of 3 μm

bpm2d
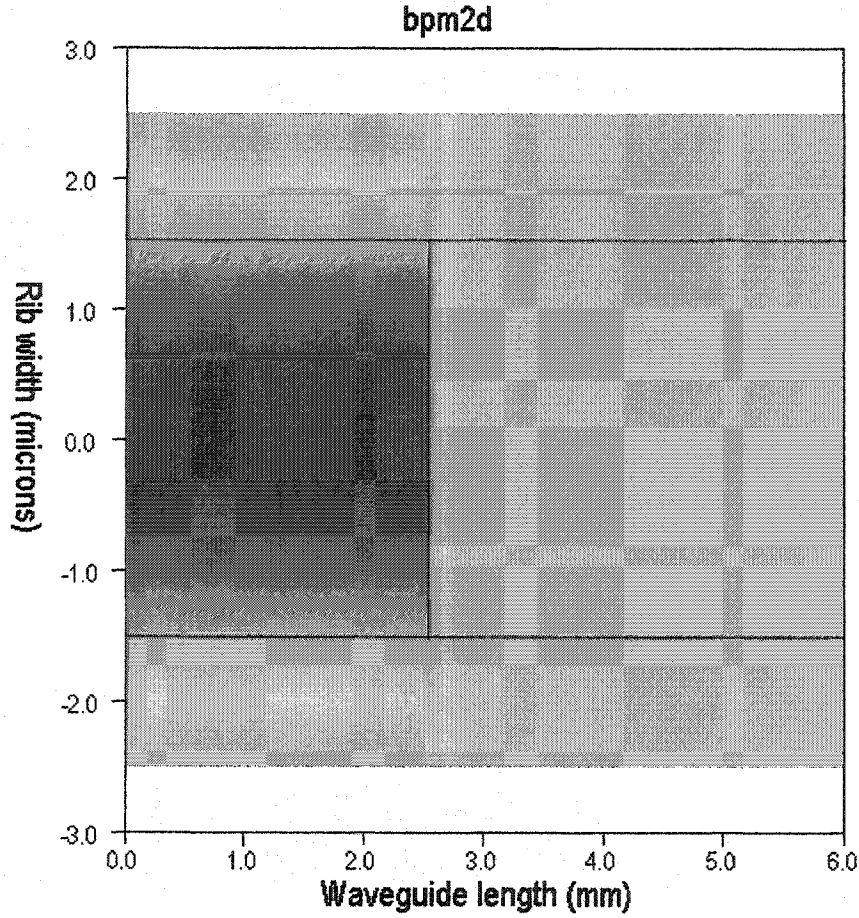
Figure 3.6: BPM simulation to study confinement of energy for a 2.5 mm long waveguide with a rib width of 3 μm

It is seem from Figures 3.5 and 3.6 that only the fundamental mode exists in both cases and the mode power is highly confined in the rib section.

3.2 Effective Index Method (EIM)

As seen from Chapter 2, gratings are realized by modulating the effective refractive index of a waveguide. In the approach used here (see Figure 3.7), this change in refractive index is achieved by changing the width of the rib. Thus, the effective index of the waveguide for different rib widths must be found in order to know the amount of index modulation that can be obtained. In order to find the range of rib widths for which the waveguide is single-moded (satisfying the single-mode conditions (Equation 3.1)), and as

well find the effective refractive index for each of those widths, a method known as effective index method (EIM) [70, 71] was used. In this method, the two-dimensional rib waveguide is divided into two one-dimensional slab structures as shown in Figure 3.8.
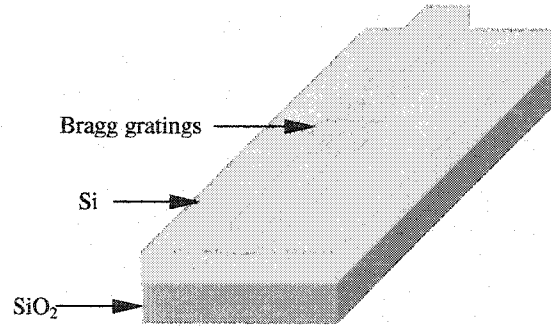
Figure 3.7: Bragg gratings on rib waveguides

(a) Step 1   (b) Step 2
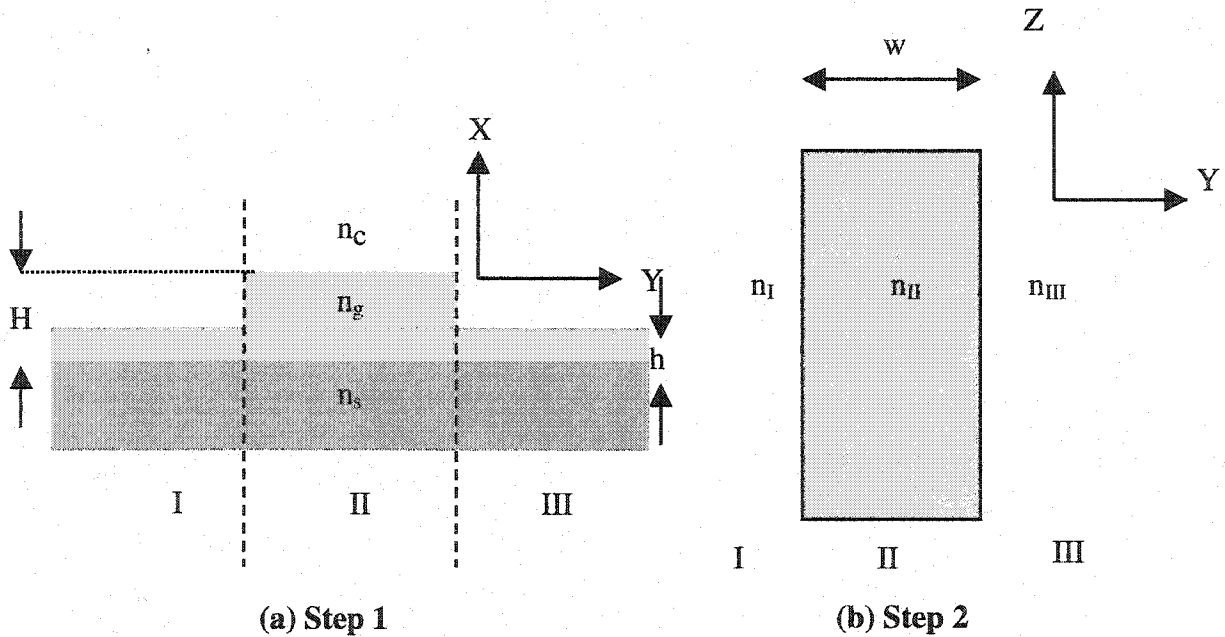
Figure 3.8: Schematic of EIM implementation for a rib waveguide

Slab waveguide solutions are obtained analytically for each of the regions I, II and III in Step 1. The effective indices of these slab regions are used to model a slab waveguide in the Y direction in Step 2. This method provides a relatively simple technique for fast analysis of rectangular waveguide structures. However, it suffers from some inherent limitations [72, 73] in terms of overestimating the propagation constants. In spite of the limitations, this technique still has been widely used for analyzing 3-D waveguides.

The EIM was encoded using Matlab [80] (Appendix I). This was used to find the effective refractive index as a function of rib width.
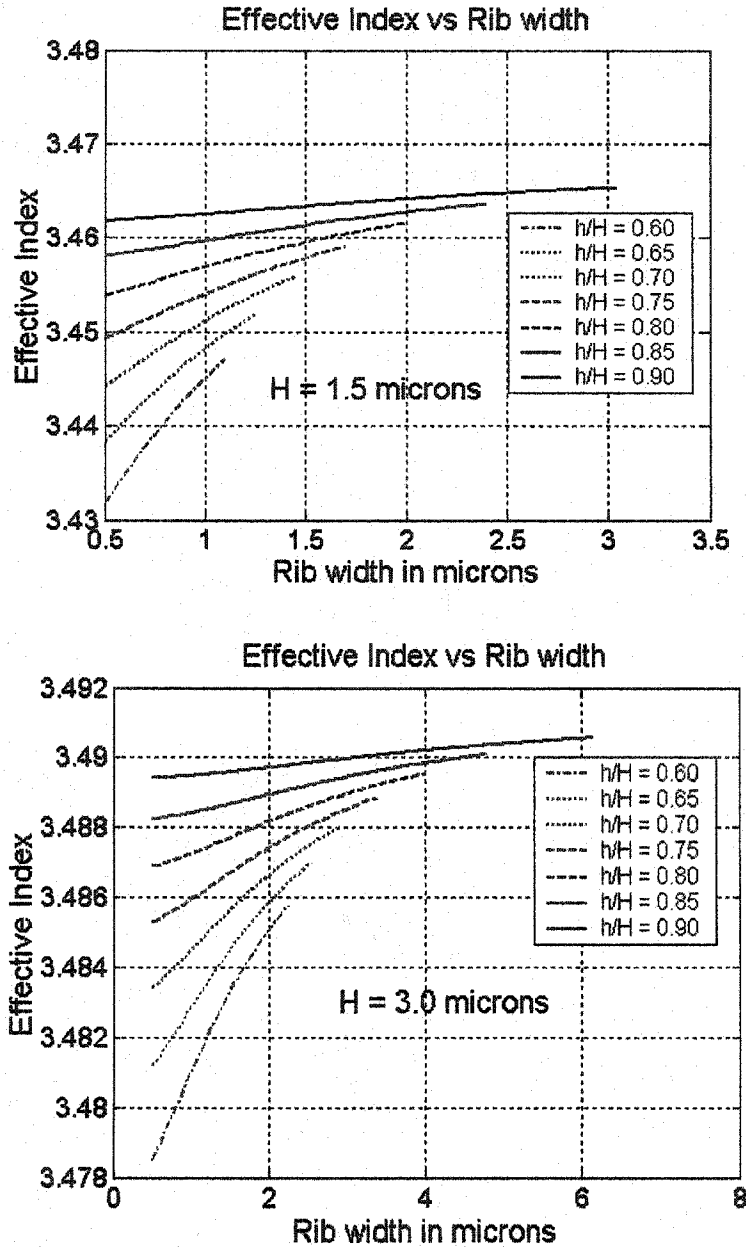
Figure 3.9: Effective refractive index Vs Rib width for the various single-mode conditions

Figure 3.9 shows the plots of Effective refractive index vs Rib width for the two SOI wafers mentioned in Table 3.1. All the curves in both of the plots satisfy the single-mode

condition stated earlier in equation 3.1. Each curve is for a certain ratio of '$\frac{h}{H}$' for the range 0.6-0.9. As the rib width changes the effective refractive index changes and, as mentioned earlier, we can make use of this property to realize gratings. Also, it is observed that the range of rib widths for which the SOI rib waveguide with a Si layer thickness of 3.0 µm is single-moded is greater than that of the SOI waveguide with Si thickness of 1.5 µm. Thus, larger cross-section waveguides could be formed on the 3.0 µm wafer and will result in lower coupling loss between the waveguide and the fiber. However, it is to be noted that the maximum index modulation obtained with SOI waveguide of 1.5 µm Si thickness is greater than for the 3.0 µm SOI waveguide. Some of the important observations are tabulated below in Table 3.3 for the two single mode waveguides:

SOI	Maximum rib width	Maximum index modulation
1.5 µm	3.0 µm	0.01
3.0 µm	6.0 µm	0.0075

Table 3.3: Max. index modulation and corresponding max. rib widths for SOI wafers with different Si layer thickness

It is to be noted that the maximum rib width is obtained for the maximum $\frac{h}{H}$ condition, while the maximum index contrast is obtained for the minimum $\frac{h}{H}$. Therefore, a compromise is necessary between coupling loss (rib width) and grating strengths (refractive index contrast).

Given the index contrasts possible using the approach described here, a single uniform Bragg grating would need to be several hundred microns long to act as a good mirror (with nearly 100% reflection at the Bragg wavelength). Such length makes it necessary to stitch together a number of e-beam fields while using e-beam lithography. As the

performance of these Bragg gratings rely heavily on the phase coherence of the light propagating through the device, it is of absolute importance that the e-beam fields are stitched with very high accuracy. It has been shown elsewhere [68] that error as small as 5 nm can introduce several unwanted effects in the filter responses. As discussed below, stitching error is still critical in the sampled gratings, since the grating sections must be 'phase-locked' to each other (i.e., separated by an integral number of grating periods). The main reason sampled gratings were explored was to get high reflectivity in spite of the limited e-beam field (80 μm).

3.3 Sampled gratings

The Bragg gratings discussed in Chapter 2 have a constant period and hence a constant coupling strength through the length of the grating structure. Furthermore, these gratings exhibit a single reflection stop band.

With the evolution of Wavelength Division Multiplexed (WDM) network and also with the increasing amount of information passed over hundreds of channels (wavelengths), it is useful to have grating filters that reflect multiple wavelengths. Sampled Bragg Gratings (Superstructures) [74] are grating devices that reflect more than one wavelength. A typical overview of Sampled gratings is shown in Figure 3.10.
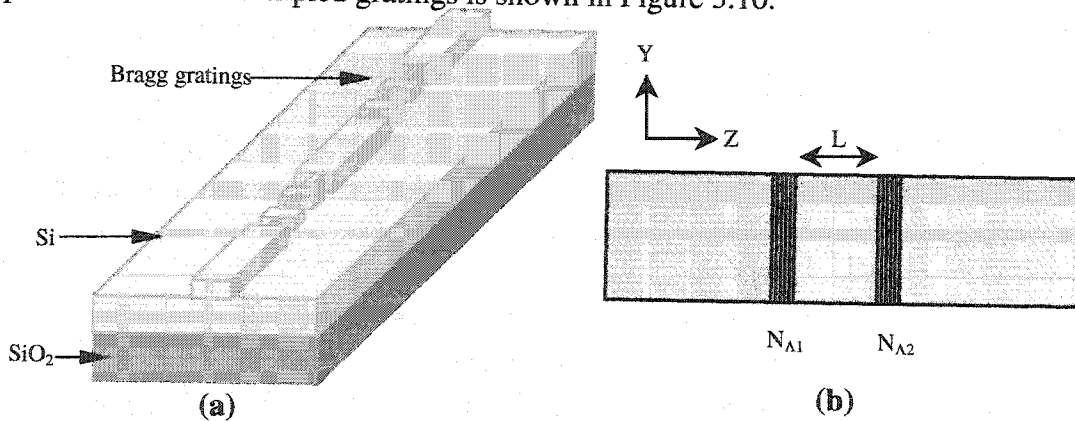
Figure 3.10: (a) 3D view of a sampled Bragg grating structure with 2 grating sections, (b) Top view of the rib with sampled Bragg gratings - grating sections separated by a distance L and each section having a certain number of periods as given by $N_{\Lambda 1}$ and $N_{\Lambda 2}$

Sampled gratings are devices having a number of grating sections arranged periodically on a waveguide. Such periodic arrangement results in a reflection spectrum having periodic maxima in the wavelength region of interest.

3.3.1 Analysis of sampled Bragg gratings

Sampled gratings are conventional gratings multiplied by a sampling function. The reflections at various wavelengths occur because of the individual contributions of the different Fourier components of the sampled gratings. The sampled gratings contain a series of Fourier components centered around the Bragg wavelength which can be understood as a combining of the Fourier component of the sampling function with the Fourier component of the normal unsampled grating [75] as shown in Figure 3.11. In other words, the underlying grating is like a 'carrier' that is 'modulated' (spatially) by a sampling function. This produces spatial harmonic sidebands each corresponding to a reflection stop band at the corresponding wavelength that satisfies the Bragg condition.
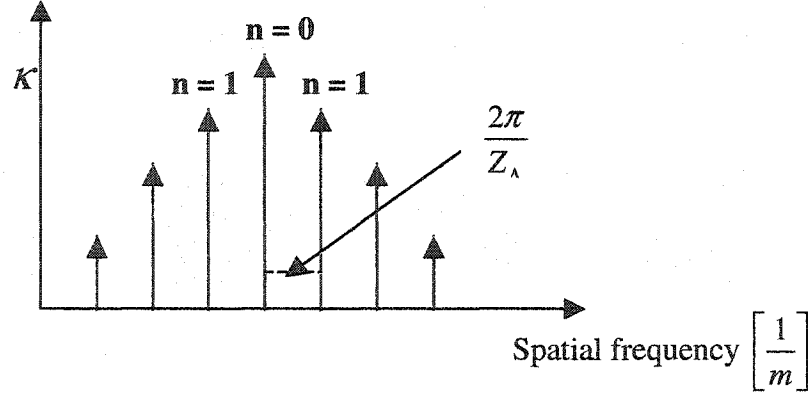
Figure 3.11: Spatial Fourier frequencies of sampled gratings [Source: [75]]

The peak reflectivity of each of the Fourier components is related to the coupling coefficient of the particular component. This coupling coefficient is in turn directly dependent on the coupling coefficient of the unsampled grating over its entire length [76]:

$$\kappa(n) = \kappa_0 \frac{Z_g}{Z_\Lambda} \frac{\sin \pi n Z_g / Z_\Lambda}{\pi n Z_g / Z_\Lambda} e^{-i\pi n Z_g / Z_\Lambda} \qquad (3.2)$$

where $\kappa(n)$ is the coupling coefficient for the nth Fourier component, κ_0 is the coupling coefficient of the unsampled grating, Z_g is the length of each grating section and Z_Λ is the period of the sampled grating. Each Fourier component of the coupling coefficient produces a stopband, with peak reflectivity given by [74]:

$$\tanh^2(\kappa(n)L_{Total}) \hspace{3cm} (3.3)$$

where $\kappa(n)$ is the coupling strength of each Fourier component and 'L_{Total}' is the length of the sampled grating. It could be seen from Figure 3.11 that the peak reflectivity decreases with increasing order of the Fourier components as a result of decreasing coupling coefficients.

Thus, the resultant spectrum for a sampled grating is a series of stop and pass bands over the wavelength region of interest.

3.3.2 Modeling sampled gratings

Two popular techniques for modeling grating structures (periodic or almost periodic structures) are coupled mode theory (CMT) [77] and transfer matrix method (TMM) [79].

TMM is a numerical analysis technique which uses a second order matrix formulation to represent the Bragg mirrors. The elements of the matrix are expressed in terms of plane-wave reflection and transmission coefficients and propagation constants derived using effective indices of the modes, obtained using the EIM [11] (see Section 3.2). This technique is well suited to numerical implementation and thus can be used to model aperiodic gratings with less computational difficulty. This so-called effective index transfer matrix method (EI-TMM) is valid for relatively weak grating structures. It does not accurately treat modal overlap between high and low index regions of the grating and therefore does not take scattering loss into account.

Because of the benefits of fast and reasonably accurate calculations, our modeling of the sampled grating device was based on the TMM.

3.3.3 TMM - Brief theoretical background

The periodic corrugation of the surface of the waveguide resulting in a periodic index modulation in the z direction can be represented as a multilayer 'high-low' structure as shown in Figure 3.12.
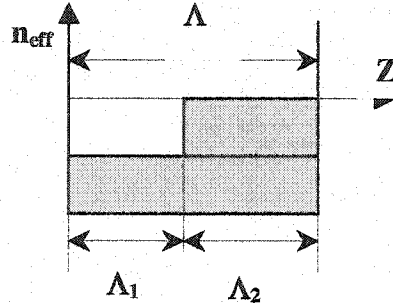
Figure 3.12: Multilayer 'high-low' structure (Source: [78]) – One period of a Bragg grating is shown schematically

The electric field amplitudes of the forward and the backward traveling modes in two arbitrary cross-sectional planes are related by [74]:

$$\begin{bmatrix} E^+(z1) \\ E^-(z1) \end{bmatrix} = \underbrace{\begin{bmatrix} M_{11} & M_{12} \\ M_{21} & M_{22} \end{bmatrix}}_{M} \begin{bmatrix} E^+(z2) \\ E^-(z2) \end{bmatrix} \tag{3.4}$$

where $z1$ and $z2$ are two interfaces of the periodic structure, the '+' and '-' indicate the forward and backward traveling modes, and M_{11}, M_{12}, M_{21}, M_{22} are the coefficients of the transfer matrix.

The overall transfer matrix 'M' is derived by multiplying a number of 'interface matrices' and 'layer matrices' in order to represent the whole grating structure. Note that the mathematical formalism is equivalent to that used to describe plane wave propagation in a thin film stack. The guided modes are analogous to plane waves and the real indices in the thin film stack are replaced by the effective indices of the waveguide Bragg grating.

The 'interface matrix' for the interface between two adjacent layers and the 'layer matrix' for the layer sandwiched between two interfaces are given by [79]:

$$M_{Interface} = \frac{1}{2n_i}\begin{bmatrix} n_i + n_{i+1} & n_i - n_{i+1} \\ n_i - n_{i+1} & n_i + n_{i+1} \end{bmatrix}$$

$$M_{Layer} = \begin{bmatrix} e^{jk_0 n_i d_i} & 0 \\ 0 & e^{-jk_0 n_i d_i} \end{bmatrix} \qquad (3.5)$$

where n_i and n_{i+1} are the effective refractive indices of the two adjacent layers, k_0 is the wavevector in vacuum and d_i the length of a given layer.

The transfer matrix 'M' for a single period in a uniform grating is:

$$M = \underbrace{M_{Interface_1} x M_{Layer_1}}_{Low-High} x \underbrace{M_{Interface_2} x M_{Layer_2}}_{High-Low} \qquad (3.6)$$

For simplicity in periodic and uniform gratings, once the transfer matrix for one period of the grating is found then the whole grating section could be represented by a transfer matrix, M^N, where N is the number of periods.

3.3.4 Modeling Results

A Matlab code was written [80] to design a scalar model of the sampled grating and study the spectral response. It is attached in Appendix II. Being a scalar model it doesn't take the polarization effects into consideration. The EIM is used to provide the effective refractive index of the different regions in the sampled grating. This is an approximate model because it doesn't account for field discontinuities in the transverse direction when the structural dimensions of the gratings change. In spite of its approximate nature, the TMM method is useful for analyzing the spectral response of aperiodic gratings and for studying random errors in the grating period that could arise during actual fabrication.

Figure 3.13 shows a plot of the spectral response characteristics of a sampled grating structure with 3 grating sections, a refractive index modulation of 0.01 and a Bragg grating period of 224 nm to produce a fundamental Bragg reflection at a wavelength of 1550 nm.

Case #1

No. of grating sections	Spacing between grating sections (μm)	Max. index modulation	No. of grating periods in each of the sections
3	268.8	0.01	313, 313, 313
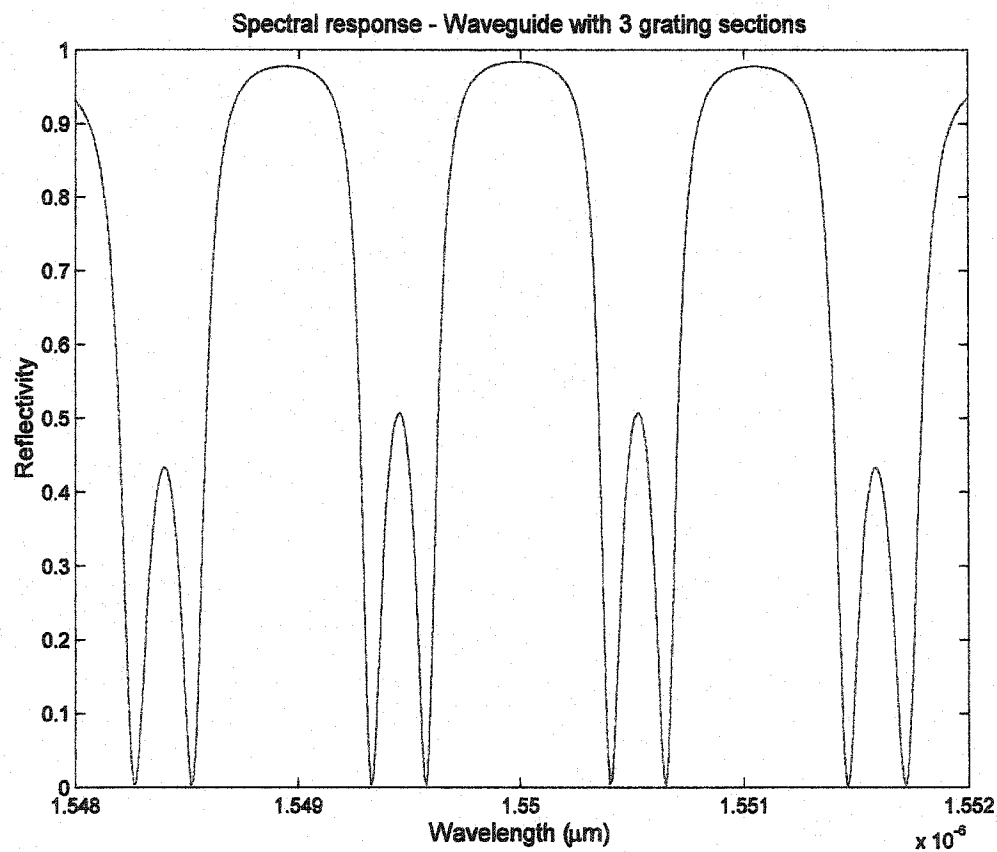
Figure 3.13: Modeling result - Case #1

As could be seen from Figure 3.13, the spectral response is a series of reflection stop-bands, each corresponding to a Fourier spatial harmonic of the index modulation in the waveguide with the peak reflectivity of nearly 100% at the fundamental Bragg

wavelength (1550 nm). However, it is noted that large amounts of 'noise' accompany this output. The 'noise' between stop-bands is due to the abrupt discontinuity between the uniform waveguide and the region of sampled grating. Such 'noise' is undesirable if the grating is used as a wavelength filter, where it is required that only the desired channels be dropped from a number of wavelength channels. The presence of this 'noise' corresponds to partial reflection of unintended wavelength channels, resulting in attenuation and crosstalk. So, in order to suppress this 'noise', apodization is performed on the grating. Apodization is performed by gradually decreasing the coupling strength of the grating towards the ends, often using a Gaussian taper function [81]. Apodization is an example of aperiodicity in grating strength that can improve and customize the optical response for certain applications.

Apodization could be introduced in the sampled grating by two means: 1) Decreasing the reflection from the ends by reducing the number of grating periods in sections nearer the ends and 2) By varying the corrugation depth (index modulation) according to a Gaussian function.

3.3.4.1 Apodization by varying the number of periods

In this method the apodization was performed by varying the number of periods in each of the grating sections as a Gaussian function and is shown in Case #2.

When apodization is performed, the stop and pass bands smoothen out and the 'noise' is reduced when compared to the non-apodized grating section. However, it is noted that the peak reflectivity at the Bragg wavelength of 1550 nm is reduced from the non-apodized Case #1. Thus, there is a compromise between the peak reflectivity and 'noise' level for sampled gratings having the same number of grating sections.

Case #2

No. of grating sections	Spacing between grating sections (μm)	Max. index modulation	No. of grating periods in each of the sections
3	268.8	0.01	225, 313, 225
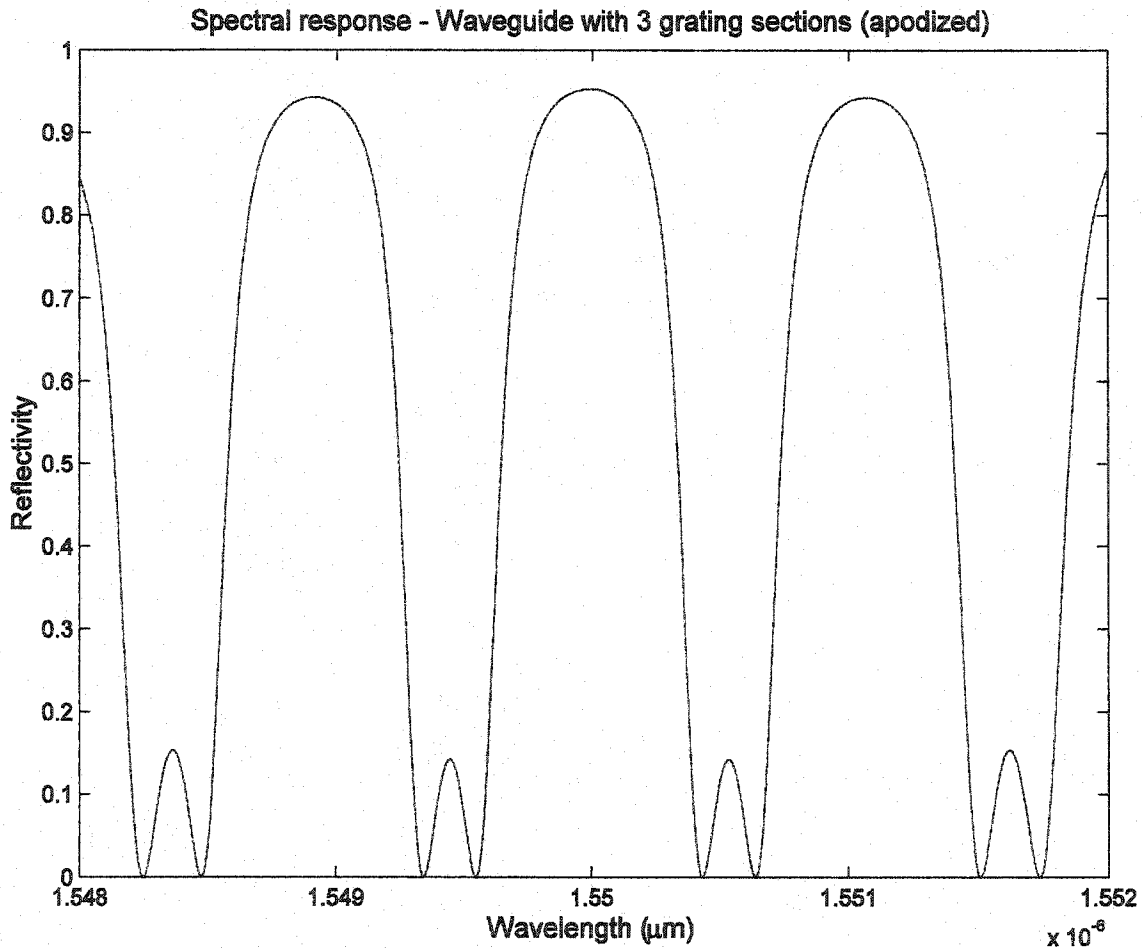
Figure 3.14: Modeling result - Case #2

In order to increase the peak reflectivity at the Bragg wavelength but still reduce the 'noise' by apodization, we look at one other simulation (Case #3).

Case #3

No. of grating sections	Spacing between grating sections (μm)	Max. index modulation	No. of grating periods in each of the sections
5	268.8	0.01	75, 225, 313, 225, 75
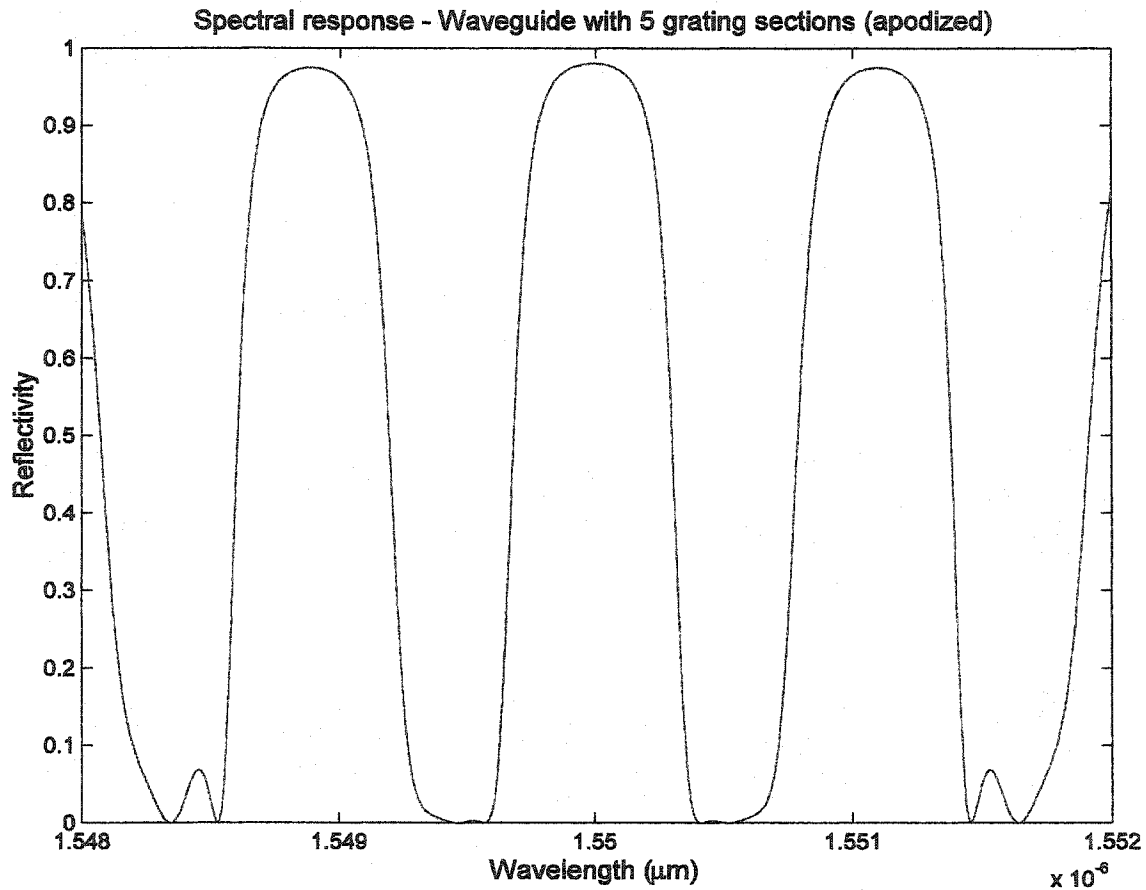
Figure 3.15: Modeling result - Case #3

As could be seen from Case #3, the peak reflectivity has increased to almost 100% for the Bragg wavelength and other stop bands but with very little 'noise' when compared to Case #2.

Cases #4 and #5 show the effect of changing the spacing between grating sections.

Case #4

No. of grating sections	Spacing between grating sections (μm)	Max. index modulation	No. of grating periods in each of the sections
5	145.6	0.01	75, 225, 313, 225, 75
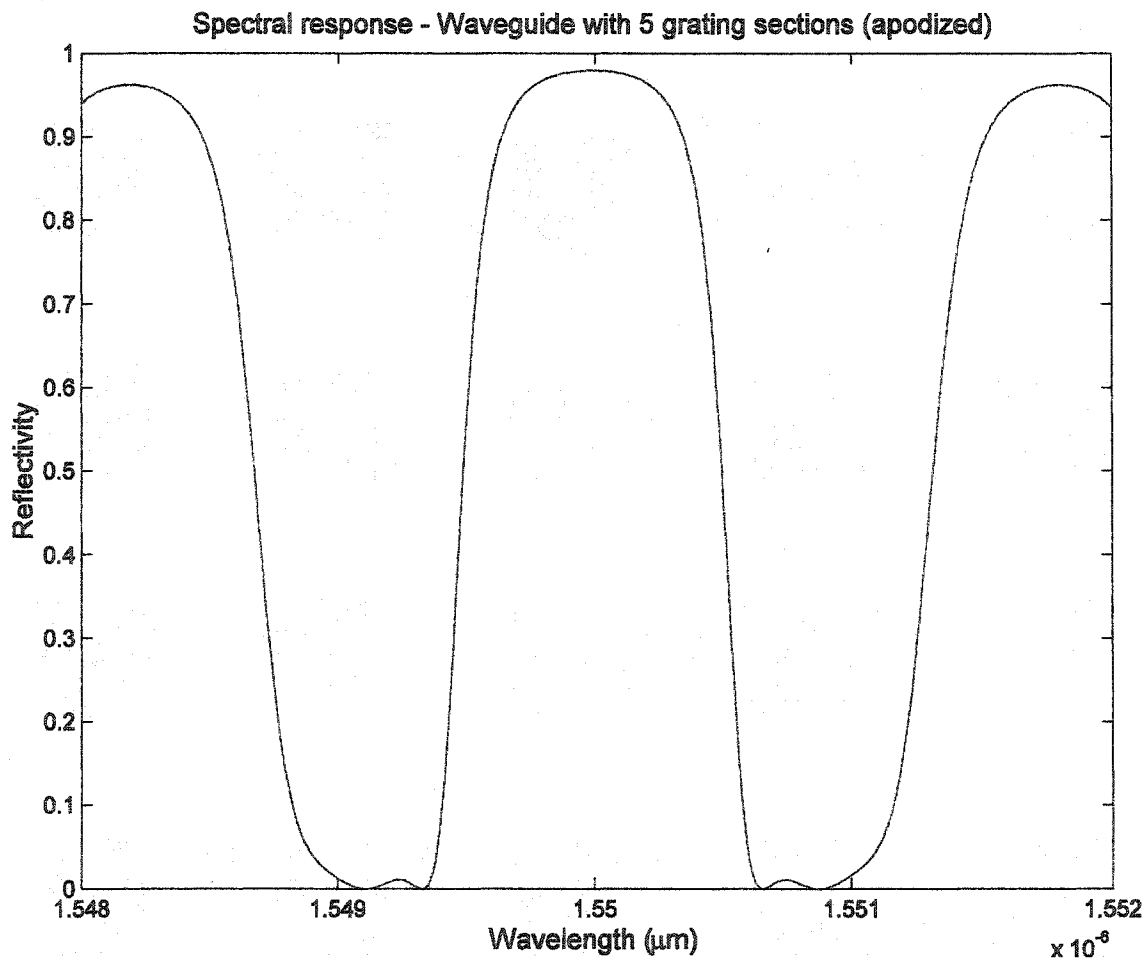
Figure 3.16: Modeling result - Case #4

Case #5

No. of grating sections	Spacing between grating sections (μm)	Max. index modulation	No. of grating periods in each of the sections
5	179.2	0.01	75, 225, 313, 225, 75
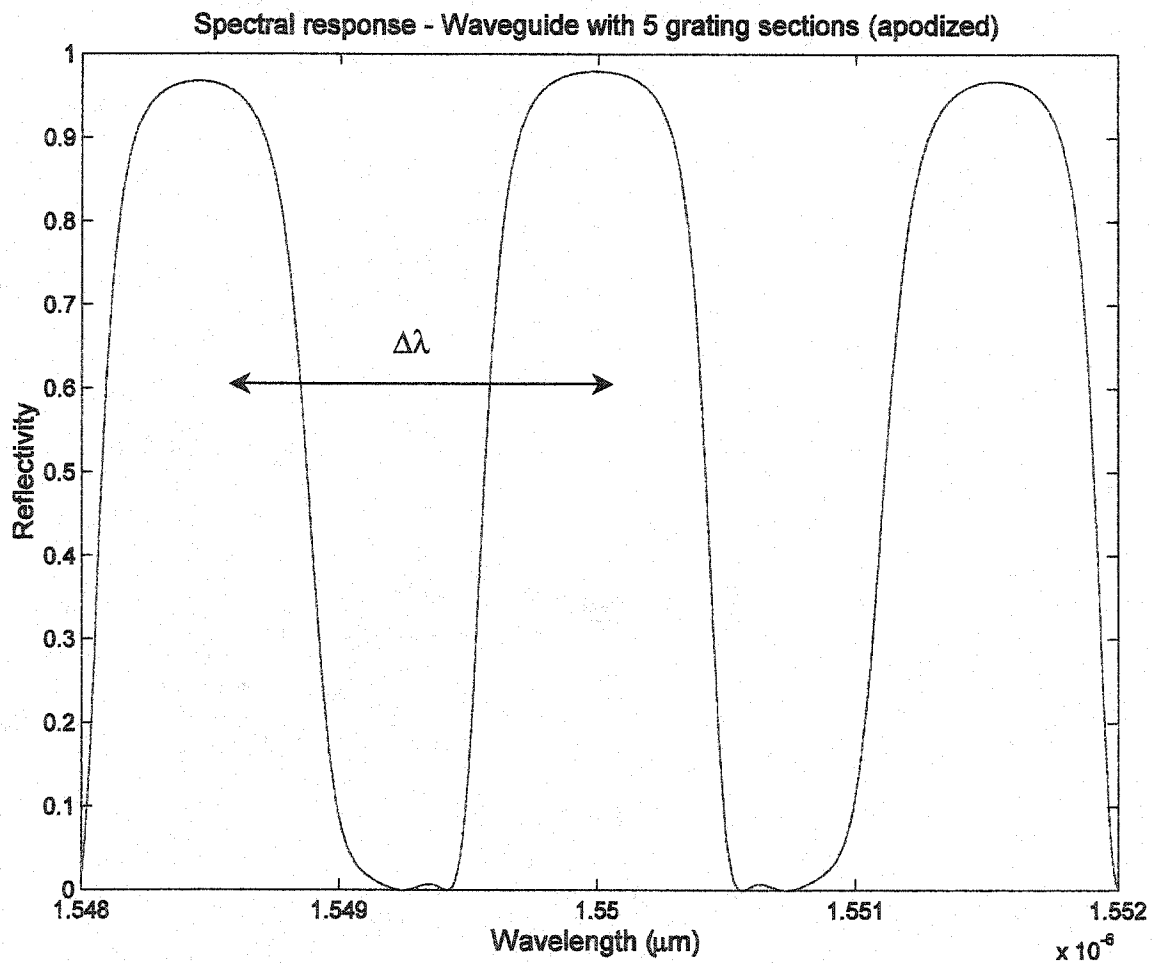
Figure 3.17: Modeling result - Case #5

Analyzing cases #3,4 and5, we observe that as the spacing between the grating sections is varied, the spacing between the stop bands varies inversely as per the relation [75]:

$$\Delta\lambda = \frac{2\Lambda_{Bragg}^2 n_{eff}}{\Lambda_{ss}}$$

(3.7)

where $\Delta\lambda$ is the stop band width, Λ_{Bragg}, the Bragg grating period, n_{eff}, the effective refractive index and Λ_{ss} is the period of the sampled grating.

The equation 3.7 gives the spacing as shown in Figure 3.17. The width of each stop band is dependent in the size of the corresponding Fourier component κ (n).

Thus, overall, it could be concluded that increasing the number of grating sections results in increased peak reflectivity and the 'noise' can be effectively minimized through apodization. However, it needs to be observed that increasing the amount of apodization results in lower peak reflectivities, so there is an inherent tradeoff between the spectral 'noise' level and the reflectivity.

3.3.4.2 Apodization by varying the refractive index modulation along the grating length

In this method of apodization, the refractive index modulation of the grating is varied as a Gaussian function about the center of the sampled grating, by changing the rib widths. The amount of index modulation is determined by a Gaussian variable. The Matlab code [80] is attached in Appendix III. The results of a few more case studies are shown below:

Case #6

No. of grating sections	Spacing between grating sections (μm)	No. of periods in each grating section	Maximum index modulation	Gaussian Variable (Gv) for apodization
5	268.8	313	0.01	1
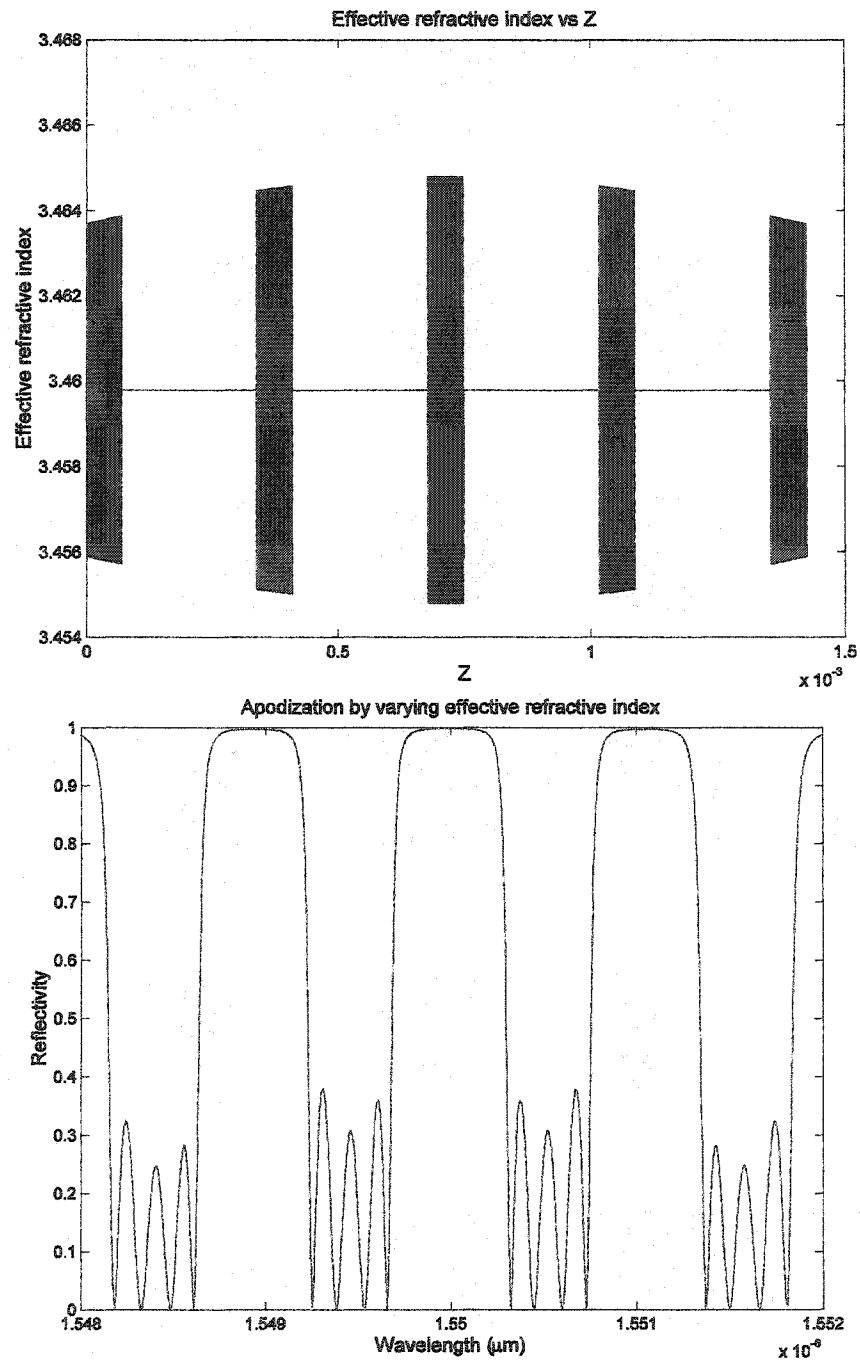
Figure 3.18: Modeling result - Case #6

Case #7

No. of grating sections	Spacing between grating sections (µm)	No. of periods in each grating section	Maximum index modulation	Gaussian Variable (Gv) for apodization
5	268.8	313	0.01	2
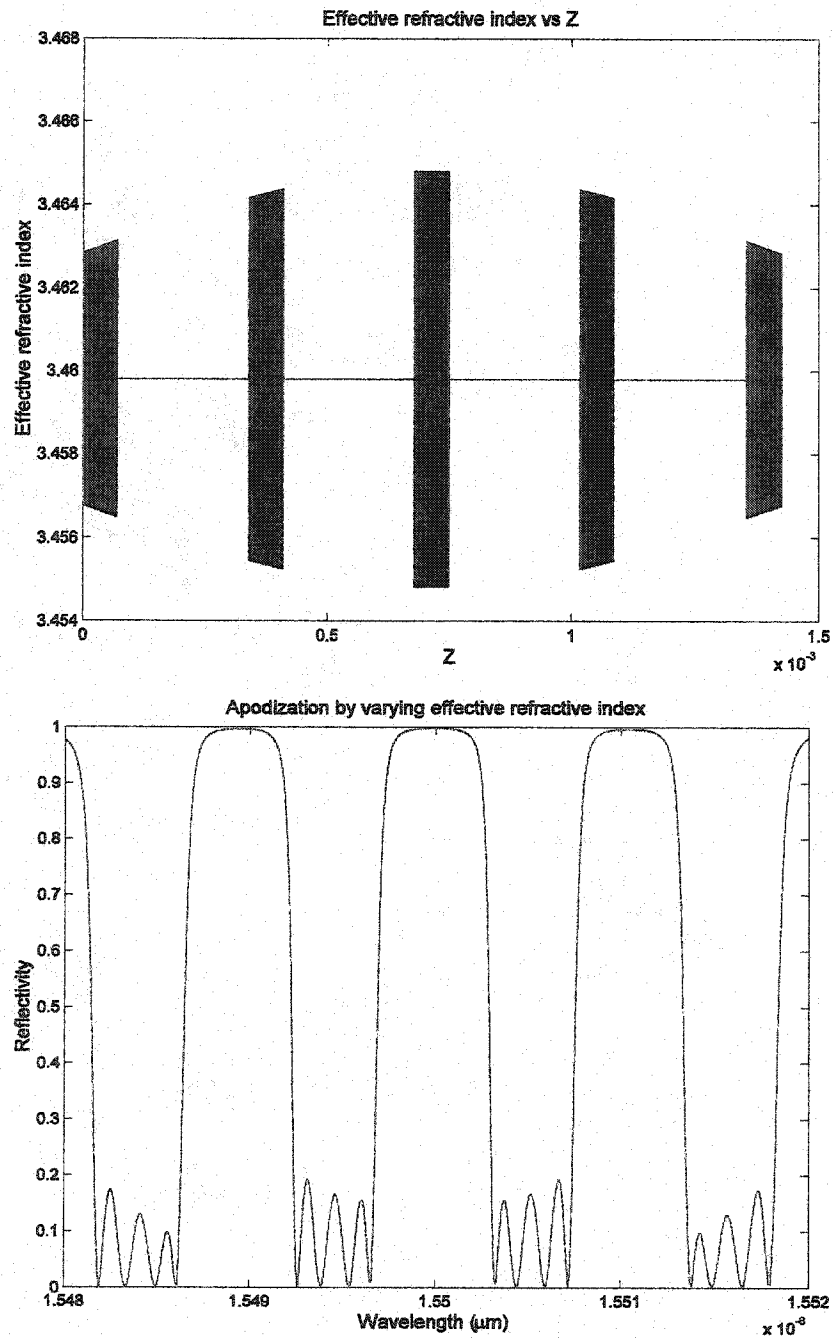
Figure 3.19: Modeling result - Case #7

Case #8

No. of grating sections	Spacing between grating sections (μm)	No. of periods in each grating section	Maximum index modulation	Gaussian Variable (Gv) for apodization
5	268.8	313	0.01	3.0
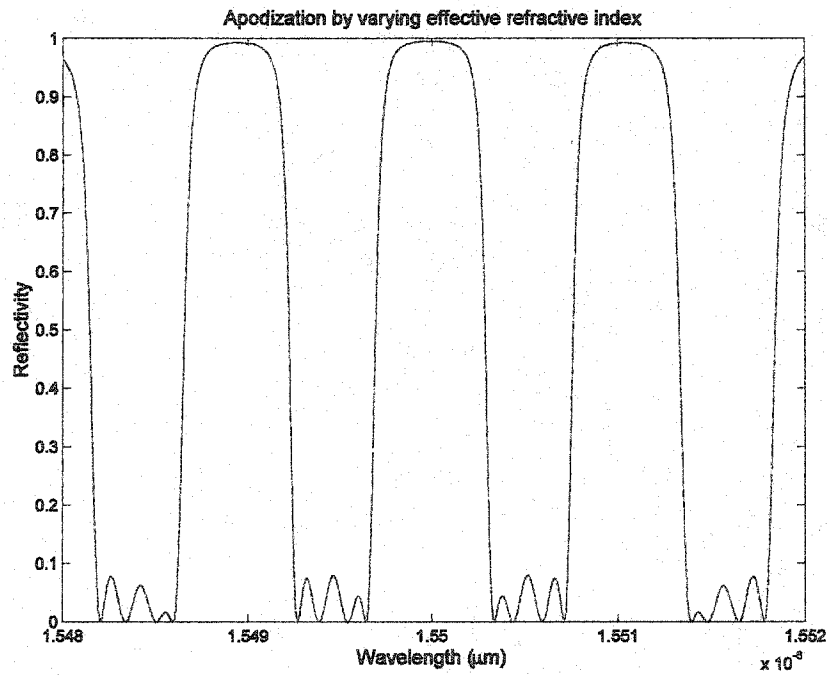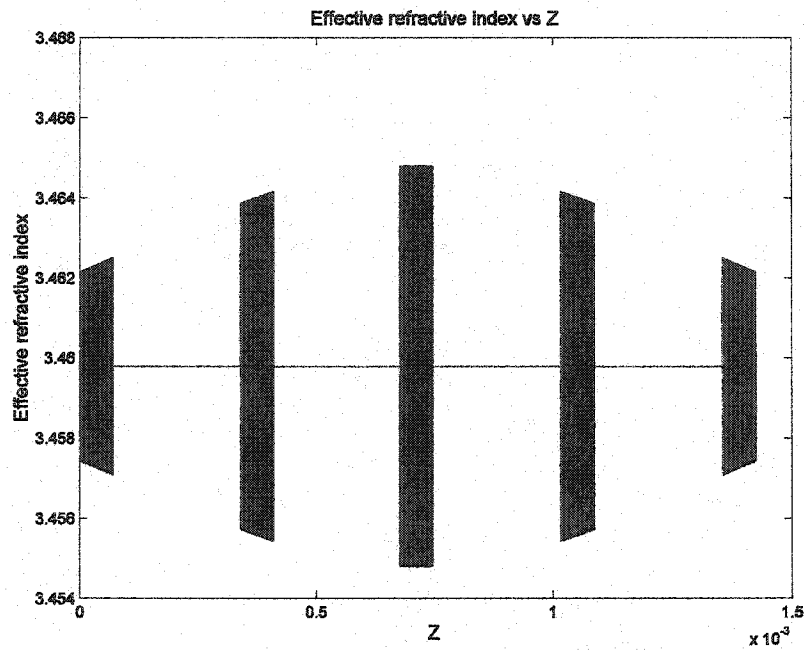
Figure 3.20: Modeling result - Case #8

Case #9

No. of grating sections	Spacing between grating sections (µm)	No. of periods in each grating section	Maximum index modulation	Gaussian Variable (Gv) for apodization
5	268.8	313	0.01	3.5
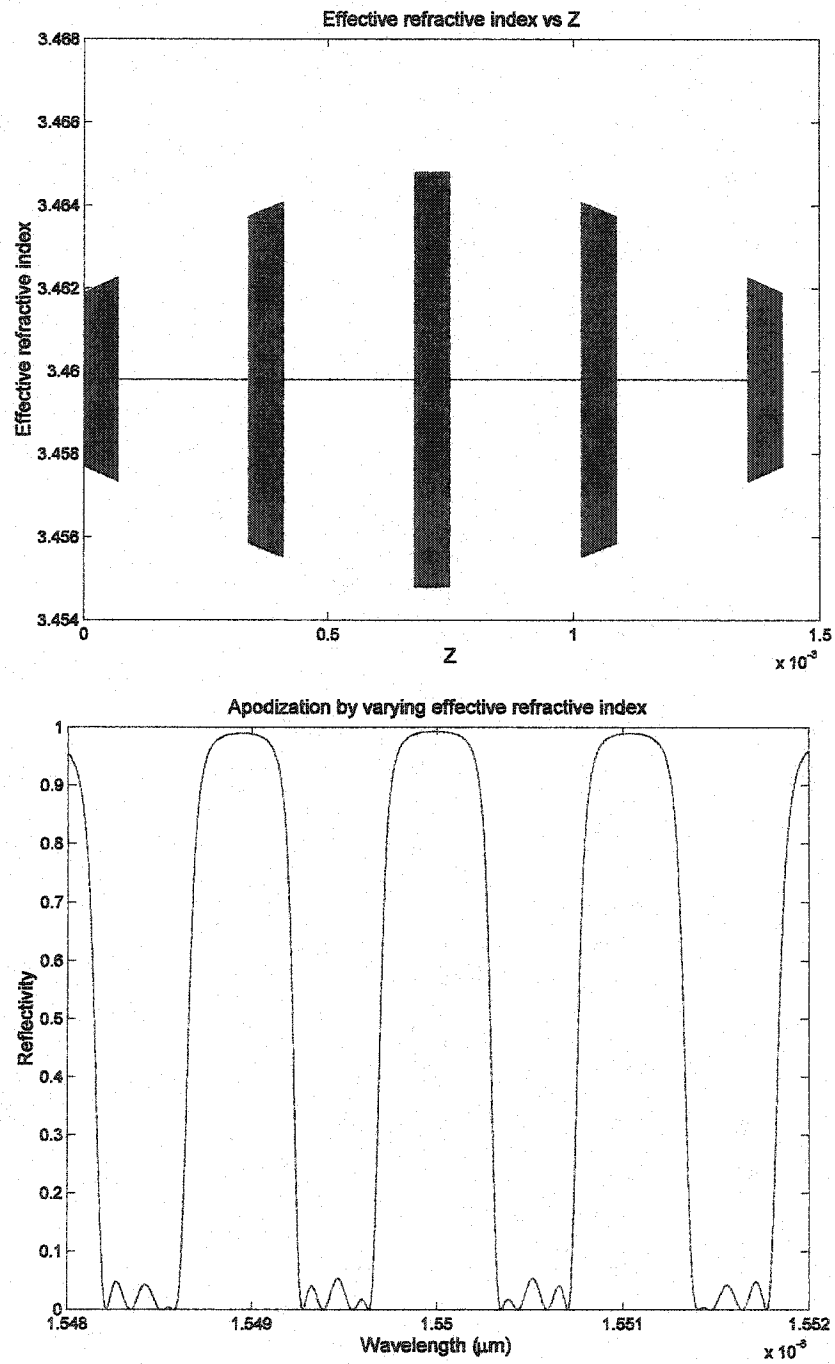
Figure 3.21: Modeling result - Case #9

From Cases #6,7,8 and 9, it could be noted that as the Gaussian variable increases the stop and pass bands become less rectangular but the 'noise' level between them is reduced. However, as for the other apodization technique discussed above, apodization results in reduction of the peak reflectivity of each stop band.

3.3.4.3 Effect of fabrication errors

Of course, there will be errors introduced during fabrication. In order to study how these errors actually affect the spectral responses of the grating structures, two types of errors were simulated. In Cases #10 - #14 below, a Gaussian distributed random error was introduced in the separation between the grating sections and in Case #15 below, a Gaussian distributed random error was introduced in the periods of the grating sections (as shown by Figures 3.22 -3.26 and Figure 3.27 respectively). Such errors are incorporated into the Transfer Matrix model by varying the parameters inside the matrix 'M'. The simplicity of this approach for studying such errors is a particularly attractive feature of the TMM.

To study the effect of spacing between the grating sections, several runs of simulations were carried out for a set Gaussian random error (Appendix IV). Each of the runs for the set Gaussian random error were plotted on the same plot to study the spectral response depending on the error the random function generates each time. The same procedure was carried out for different set Gaussian random errors. As seen from cases #10 - #14, the spectral responses from the different runs for a set random error vary depending on the error the random function generates each time. It is noted that this scatter in the desired spectral response is minimal for smaller values of random errors but increases to undesirable levels for higher values of Gaussian random errors (as seen from Figures 3.22 – 3.26). This just emphasizes that the overall spectra in a sampled grating is very much dependent on exact phase coherence (i.e., the distance must be nearly an integral number of Bragg periods) between the grating sections, which cannot just be randomly spaced. It is very much desired that the scatter in the spectral response be minimal in order to be

able to determine with reasonable accuracy the apodization required to reduce the 'noise' in the output and still achieve close to 100% reflectivity.

Case #10

No. of grating sections	Spacing between grating sections	Maximum index modulation	Gaussian random error in spacing between sections
3	268.8 μm	0.01	5 nm
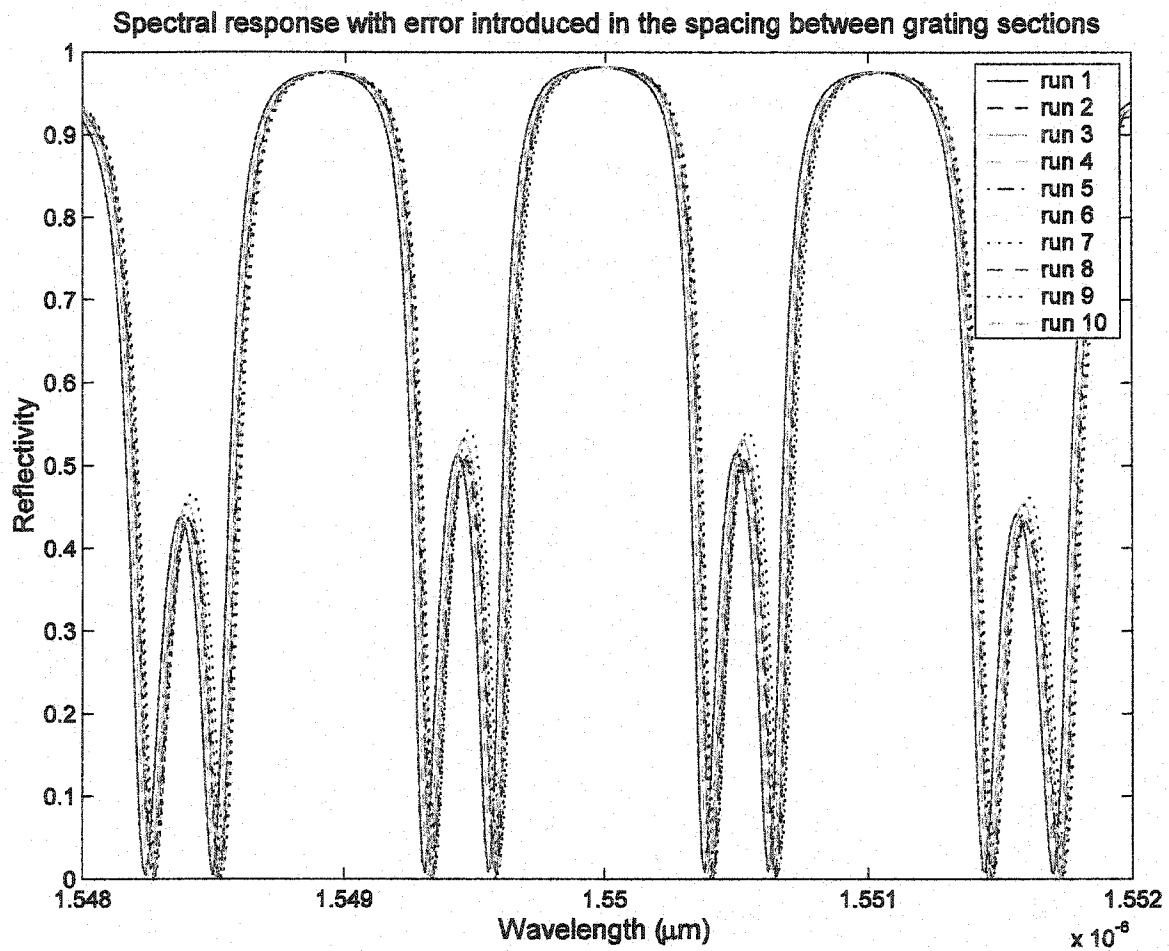
Figure 3.22: Modeling result - Case #10

Case #11

No. of grating sections	Spacing between grating sections	Maximum index modulation	Gaussian random error in spacing between sections
3	268.8 μm	0.01	10 nm
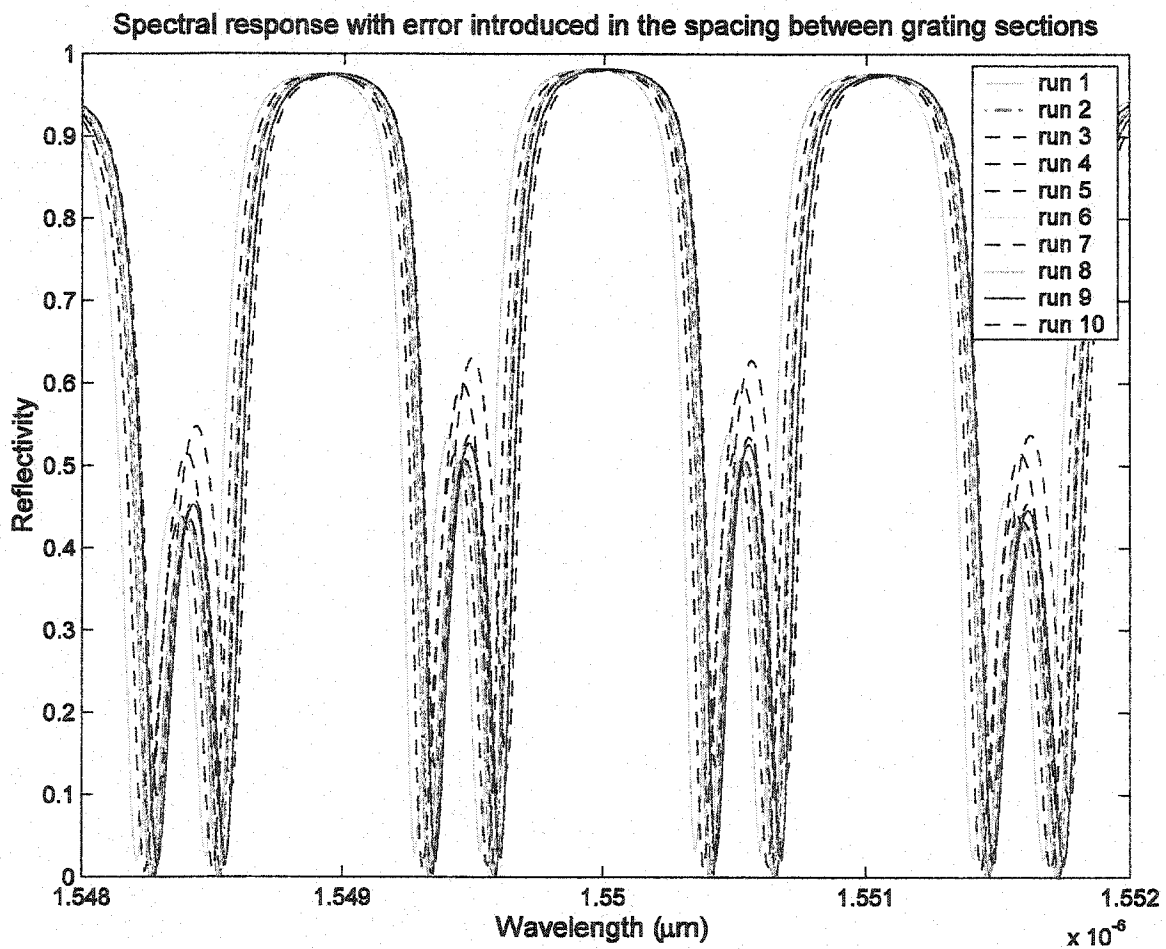
Figure 3.23: Modeling result - Case #11

Case #12

No. of grating sections	Spacing between grating sections	Maximum index modulation	Gaussian random error in spacing between sections
3	268.8 μm	0.01	15 nm
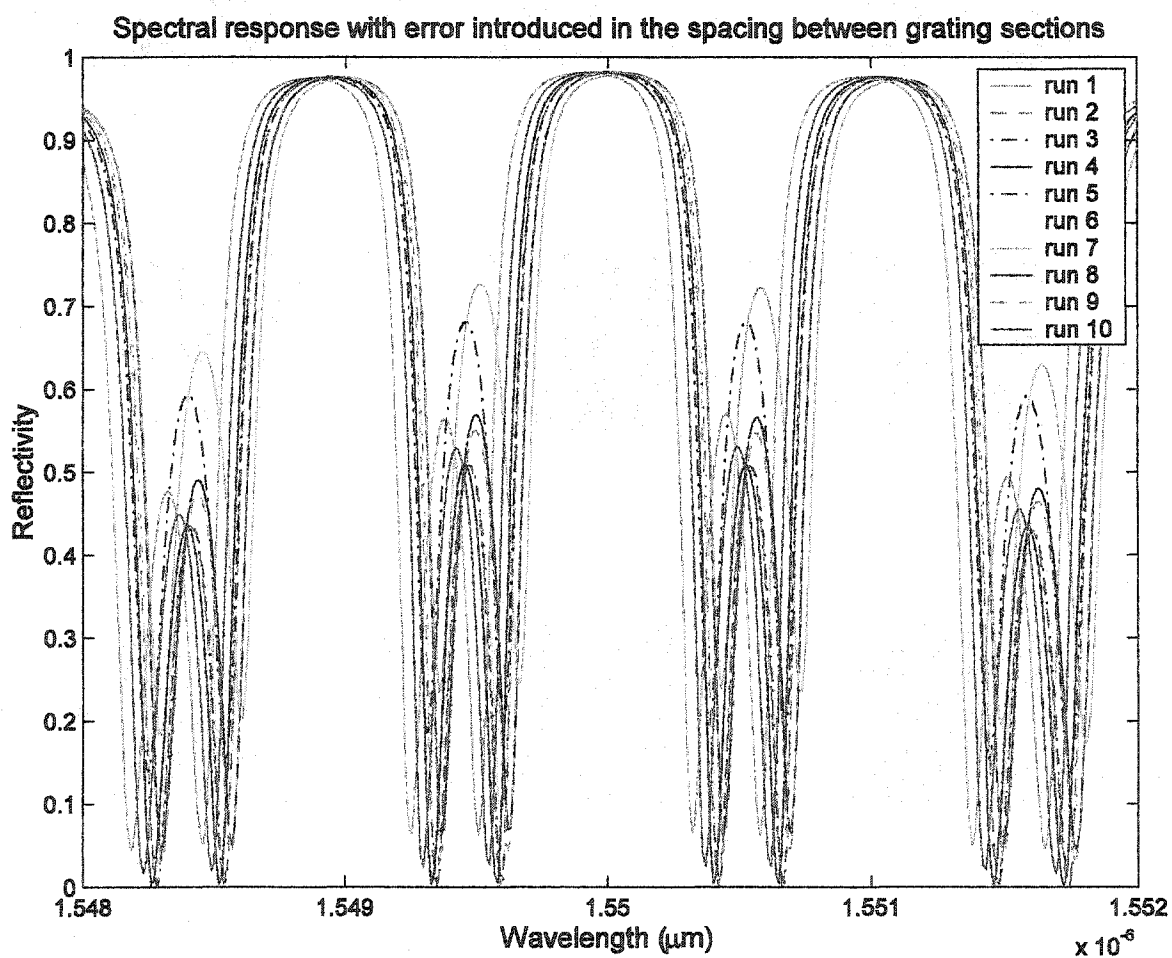
Figure 3.24: Modeling result - Case #12

Case #13

No. of grating sections	Spacing between grating sections	Maximum index modulation	Gaussian random error in spacing between sections
3	268.8 µm	0.01	20 nm
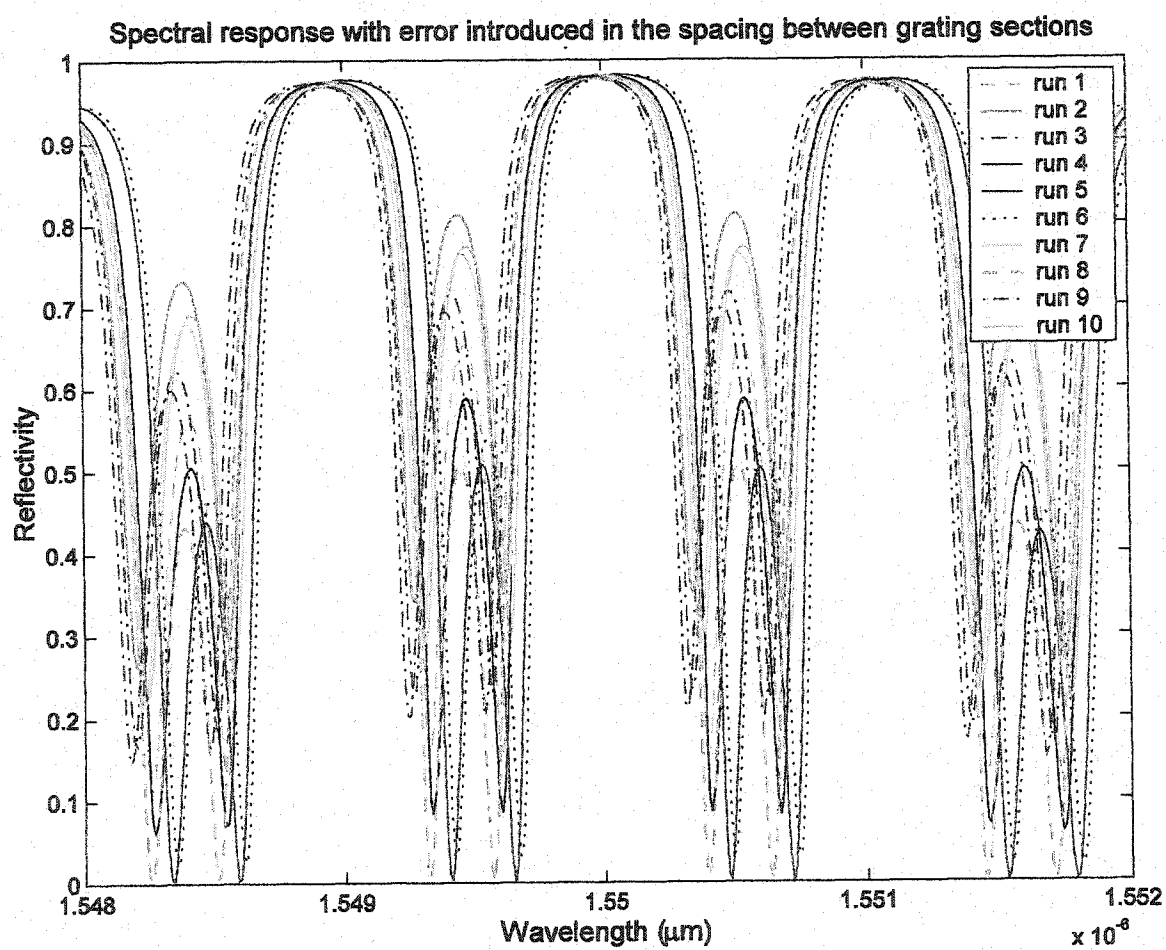
Figure 3.25: Modeling result - Case #13

Case #14

No. of grating sections	Spacing between grating sections	Maximum index modulation	Gaussian random error in spacing between sections
3	268.8 μm	0.01	30 nm
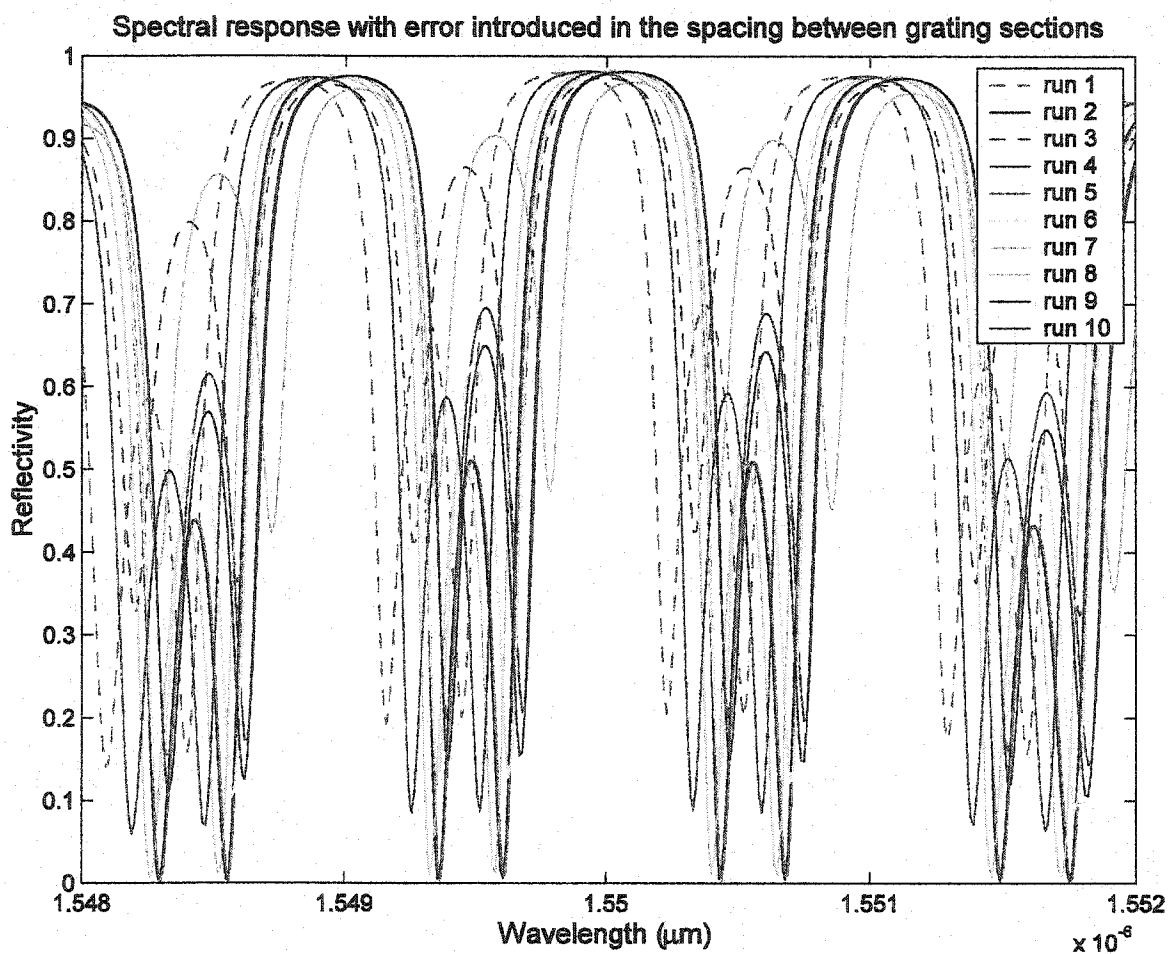
Figure 3.26: Modeling result - Case #14

The accuracy required with the spacing lengths, as seen from Cases #10 - #14, is impossible to obtain with optical lithography. An interferometric stage in the e-beam system is required in order to control the spacing of grating sections with such high accuracy.

Having studied the effect of spacing between grating sections on the spectral response and the requirement for stringent control, a simulation was carried out to study the effect of error in the period of the grating sections (Appendix V). Case #15 shows the spectral response characteristics of the gratings when a Gaussian random error of 4 nm is introduced in the periods of the grating sections.

Case #15

No. of grating sections	Spacing between grating sections	Maximum index modulation	Gaussian random error in period of gratings
3	268.8 μm	0.01	4 nm
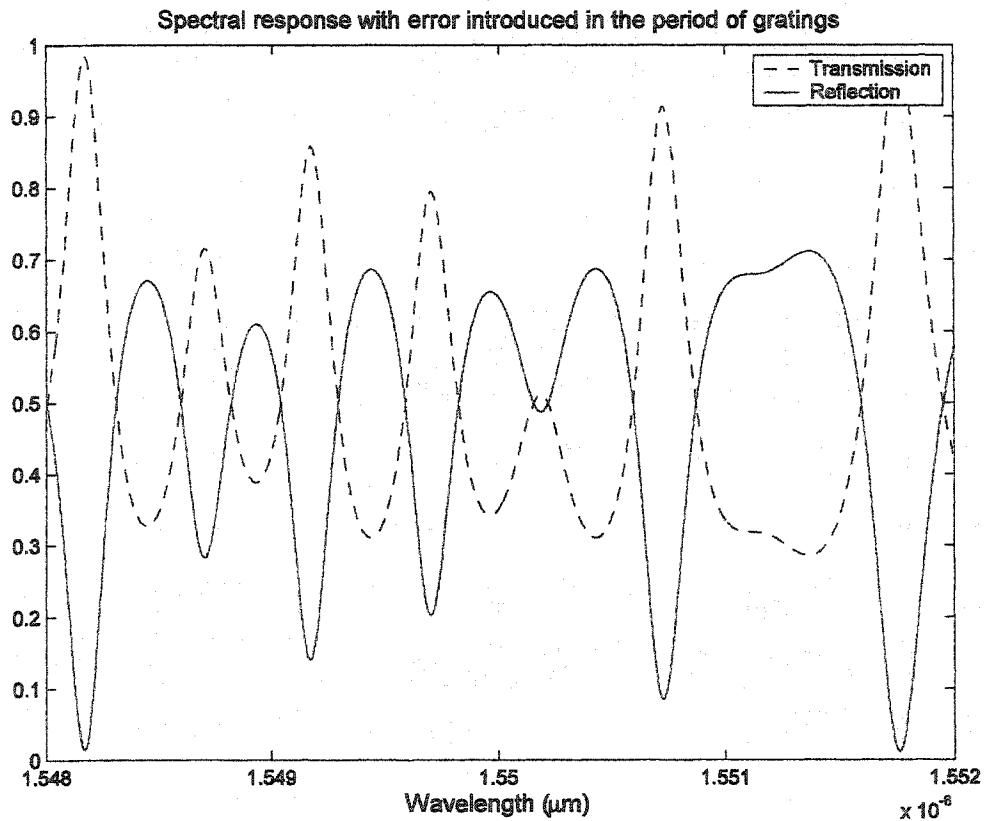
Figure 3.27: Modeling result - Case #15

It is observed from the above spectral response that even a small mean standard deviation of 4 nm in the period of the gratings destroys the desired spectral response thus emphasizing that there has to be a very tight control while writing the periods of the grating structure. This study bolsters our decision to use the high-accuracy e-beam lithographic tool to pattern the grating structure and to reduce any such errors in the grating periods.

The sampled gratings proposed in this work would provide desired results only with the use of e-beam lithography system mounted on an interferometric stage to accurately control both the grating periods and the spacing between the grating sections. However, it is worth investigating fabricating and testing these gratings without the interferometric stage in order to finalize and optimize other fabrication processes involved.

3.4 Example application

To emphasize the importance of sampled grating devices, let us now discuss an example application [82] where they could be used to realize a tunable wavelength filter. The schematic of this application is shown in Figure 3.28 . Let us demonstrate how a particular channel could be dropped in a WDM network from the input spectrum consisting of a number of channels.

Consider an input spectrum with 4 channels, and a channel spacing of 100 Ghz ($\approx$0.8 nm at 1550 nm wavelength). If one of these channels is to be dropped (filtered), this could be achieved by passing the input through 2 filter stages. Each of the filter stages consists of 2 sampled gratings whose periods are so arranged that they provide complementary outputs. Furthermore, the width of the stop bands in the second filter is exactly half of the stop band width in the first filter. The filter stages are connected by means of 2 X 2 switches as seen from the schematic in Figure 3.28.

In the first filter stage, two of the wavelengths will be transmitted and two reflected, as could be seen from the simulation of the first filter stage in the above schematic. The

grating filters in Stage 1 have stop band widths of 1.6 nm, which is twice the channel separation. By appropriately choosing the outputs from the first filter stage and coupling into the next Stage 2 of grating filters with stop band widths of 0.8 nm using the 2 X 2 switches, we can filter out one of the 2 channels transmitted from the first stage, thus filtering one of the four channel from the input spectrum.
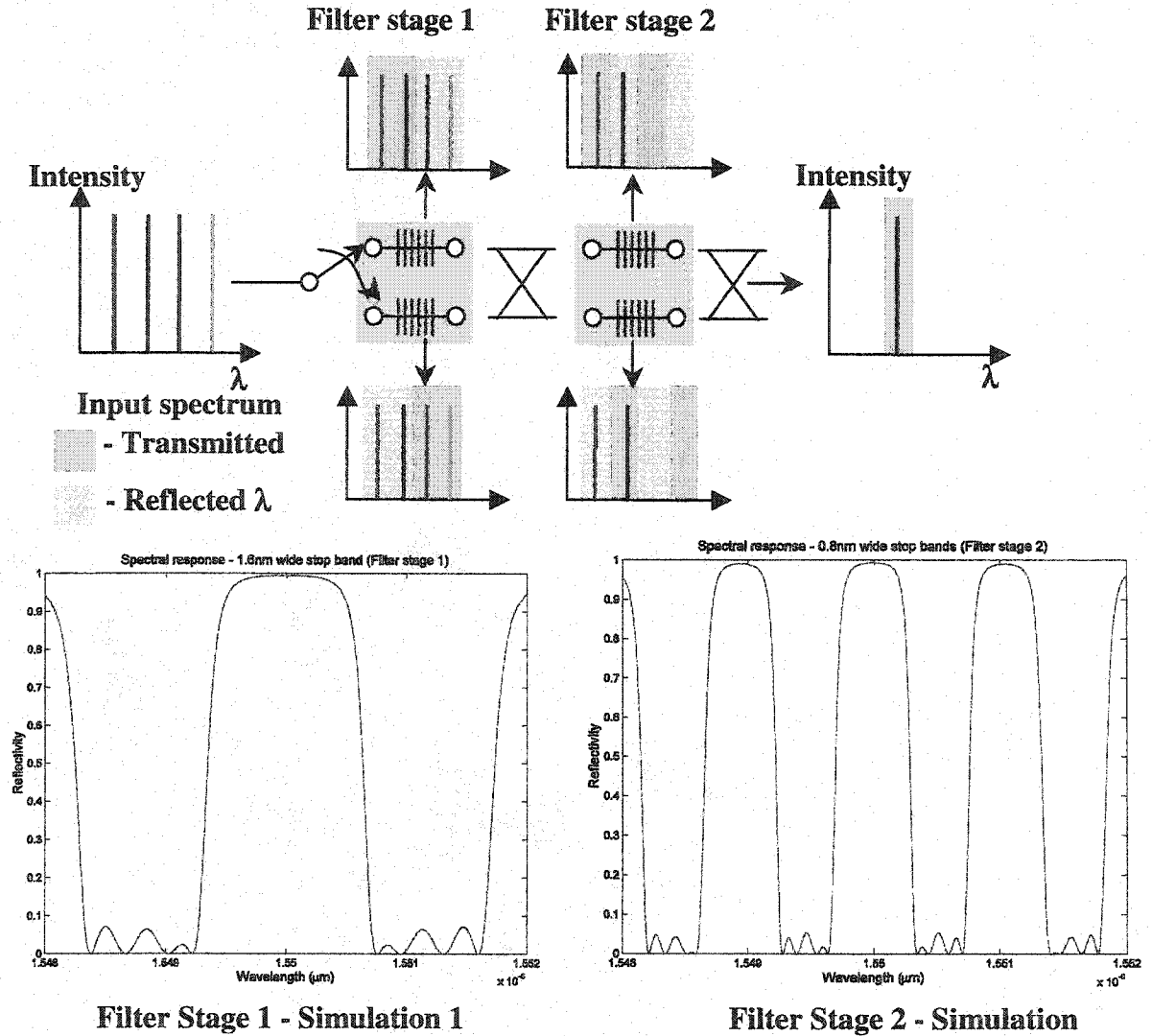
Figure 3.28 (Source [82]): Example application - Schematic

Such filtering would usually require four filter stages, however, the proposed filtering technique using our device would just require two such filtering stages. The advantage of

this technique could be further appreciated when we consider thousands of channels in the input spectrum. For example, if there were 1024 channels in the input spectrum, then, this technique of filtering would require 10 filters. This method of logarithmic filtering was proposed by Lam *et al.* [82].

Having seen the design, modeling, simulation results and advantages of this sampled grating device, the next step is to fabricate such devices. The fabrication techniques, challenges, and the processes involved will be discussed in Chapter 4.

4. Fabrication process

This chapter deals with the study and optimization of different fabrication processes involved in making grating filters on SOI waveguides. The goal was to embed gratings in waveguides that are a few millimeters long, for practical device handling and fiber coupling. Gratings need very tight control of their periods as seen in the previous chapter and e-beam is the best lithographic tool available for achieving such accuracy. However, long waveguide patterns are impossible to write without stitching errors using e-beam lithography. For this reason, two levels of lithography were proposed to realize the SOI waveguides with embedded gratings. Conventional optical lithography is used to define the waveguide pattern and e-beam lithography to write the grating corrugations. To precisely control the operation of the proposed wavelength filter, it is highly critical that even a small angular misalignment between the waveguide and the grating pattern be avoided. A simple technique is proposed to maintain such high angular alignment.

Once patterned, the waveguide and the gratings have to be etched into the silicon layer to create ribs and to realize the device. Etching usually introduces some errors into the structure in the form of rough sidewalls and loss of dimensional control (due to over etching and/or undercutting of sidewalls). To keep such errors to the minimum possible, we propose a single etching process following the optical and e-beam lithography steps. Various other techniques for the fabrication of grating-based devices using e-beam lithography and Reactive Ion Etching (RIE) have been reported in the literature [83-88].

4.1 Mask Design

A prototype mask was designed for optical lithography of the waveguide structure. Alignment marks and reference lines were also included to facilitate angular alignment during e-beam exposure. A design overview of a section of this mask layout is shown in Figure 4.1 and Scanning Electron Microscope (SEM) image in Figure 4.2.

Figure 4.1: Schematic design overview of the mask layout

Every waveguide has a long reference line on its left-hand side. In addition, two pairs of alignment marks were placed symmetrically on either side of the waveguide at a predetermined distance. The purpose of these marks will be discussed at a later stage in this chapter. The waveguides are 5 mm in length. Gaps of $\approx$70 μm were placed along the length of the waveguide pattern; in these spaces the grating pattern is subsequently formed by e-beam lithography as discussed below. The number of gaps in each waveguide is equal to the number of desired grating sections in the sampled grating structure. The 70 μm gap is chosen because of the field limitation (80 X 80 μm^2) imposed by the e-beam lithography system, to avoid stitching fields. The designed prototype mask consists of waveguide patterns with the following varying parameters: 1) Number of grating sections, 2) Spacing between the grating sections, and 3) Width of the waveguides. The designed prototype mask is summarized in Tables 4.1 and 4.2.

57

Figure 4.2(a): SEM picture showing top view of one section in the mask layout
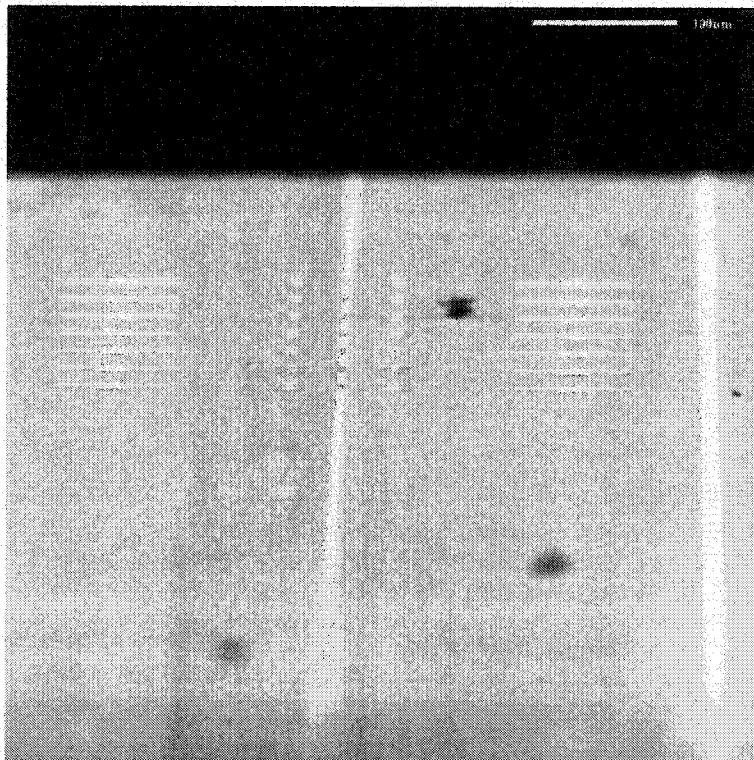
Figure 4.2(b): SEM picture of one section in the mask layout

Cell 1	Waveguides with 1 grating section	Waveguides with 3 grating sections Spacing between grating sections - 268.8μm	Cell 2
Cell 3	Waveguides with 5 grating sections Spacing between grating sections - 268.8μm	Waveguides with 7 grating sections Spacing between grating sections - 268.8μm	Cell 4
Cell 5	Waveguides with 3 grating sections Spacing between grating sections - 212.8μm	Waveguides with 5 grating sections Spacing between grating sections - 212.8μm	Cell 6
Cell 7	Waveguides with 7 grating sections Spacing between grating sections - 212.8μm	Waveguides with 3 grating sections Spacing between grating sections - 156.8μm	Cell 8
Cell 9	Waveguides with 5 grating sections Spacing between grating sections - 156.8μm	Waveguides with 7 grating sections Spacing between grating sections - 156.8μm	Cell 10
Cell 11	Waveguides with 3 grating sections Spacing between grating sections - 100.8μm	Waveguides with 5 grating sections Spacing between grating sections - 100.8μm	Cell 12
Cell 13	Waveguides with 7grating sections Spacing between grating sections - 100.8μm	Waveguides with 1 grating section	Cell 14

Table 4.1: Design details of the entire physical layout of the mask

Number of grating sections	Spacing between gratings (μm)	Widths of the waveguides for each spacing (μm)
1		
3	268.8, 212.8, 156.8, 100.8	1.0 - 3.0 (Steps of 0.2 μm) 3.3 - 5.0 (Steps of 0.3 μm) 5.5, 6.0
5	268.8, 212.8, 156.8, 100.8	
7	268.8, 212.8, 156.8, 100.8	

Table 4.2: Prototype mask layout - Feature dimensions

Note the following:

- All widths in Table 4.2 are within the minimum and maximum limitations for the existence of single-mode waveguides in SOI with device layer thickness of 3.0 μm (see Section 3.1.2).

- The various values of spacing 'L' between the grating sections were chosen based on simulation results. This is to allow flexibility to study different spectral responses with respect to their stop-band widths.

- Different number of grating sections is incorporated in the design to study the peak reflectivity. As was seen in Chapter 3, the larger the number of grating sections, the greater the peak reflectivity.

A commercial e-beam defined photomask was obtained, fabricated on a 5" X 5" X 0.09" quartz glass plate. The Critical Dimension (CD) tolerance of the fabricated mask is +/- 0.2 μm and the minimum feature size is 1.0 μm.

4.2 Optical lithography

This is the first step in the fabrication of the waveguides. After proper cleaning, the SOI substrates were coated with a standard positive optical photoresist. The resist was spun for 40 seconds at 4000 rpm to a thickness of 1.5μm. The resist thickness 'T' is dependent on the following expression [89]:

$$T = \frac{KC^{\beta}\eta^{\gamma}}{\omega^{\alpha}} \qquad (4.1)$$

where K is the overall calibration constant, C is the polymer concentration, η is the resist molecular weight and ω is the spin speed.

After coating, the sample was softbaked for 2 minutes in an oven at 115°C to remove any built-in stress. This process also improves adhesion of resist to substrate. The sample was then exposed to UltraViolet (UV) light for 5 seconds through the optical mask described earlier. The region of the resist exposed to UV light gets dissolved, leaving a replica of the pattern in the mask. The sample was then developed in a standard developer for 20 seconds. During this time, the dissolved resist was washed away leaving a trench in the exposed region constituting the mask pattern. A schematic of the various steps involved in optical photolithography is shown in Figure 4.3.

Step 1: Spinning of Optical photoresist on SOI

Step 2: Exposure to UV light through photomask

Step 3: Exposed resist on SOI after developing
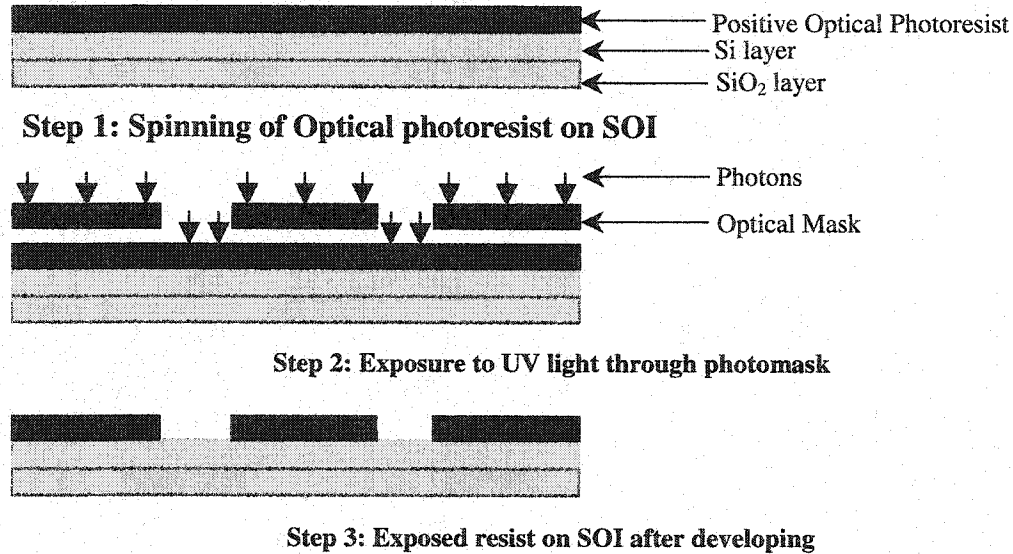
Figure 4.3: Steps involved with optical lithography process

Baking of the resists at high temperatures after spinning and proper timing of the developing process, aids in better resolution of the pattern. Improper cleaning of mask and substrate, insufficient baking, exposure time and/or developing of the exposed pattern could result in the introduction of ripples rather than the desired rectangular features. This could also result in deviation from the desired CD of the waveguide pattern. A SEM picture of a waveguide patterned by a poor optical lithographic step is shown in Figure 4.4. Note the rounding of square features.
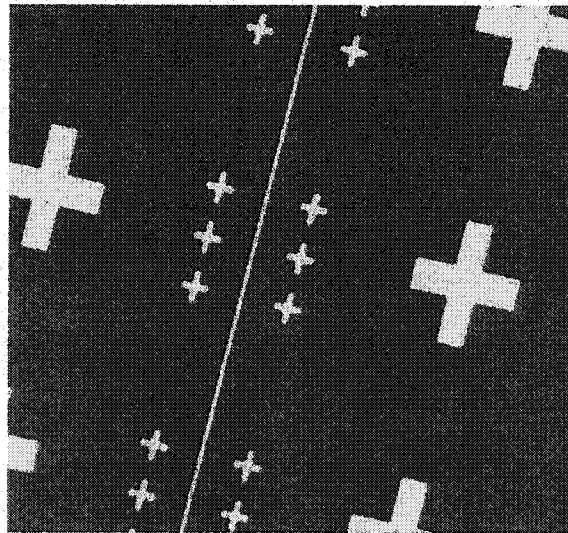
Figure 4.4: SEM picture of waveguide and alignment marks, patterned by poor optical lithography process

61

Maintaining high resolution is critical in waveguide grating fabrication. Poor resolution not only affects the waveguide dimensions but also the alignment marks. Circular corners and inadequate control of critical dimensions could result in poor alignment, leading to the introduction of gaps between the grating pattern (to be written by e-beam) and the waveguides. Such gaps create a phase shift that is highly undesirable in grating devices. This issue is discussed in detail in Section 3.3.4.3.

4.3 Liftoff for waveguide etch mask

Following optical lithography, an e-beam sensitive resist was used to define the grating pattern. As a single etch step is used in the proposed process, it was necessary to protect the already defined waveguide pattern for etching later. Thus a metal etch mask was evaporated to a thickness of 40 nm and lifted-off. Three different etch masks were considered, namely: Aluminum (Al), Chromium (Cr) and Gold (Au). The discussion of the etch mask deposition technique, the choice of the thickness and the performance of the three etch masks is left to later sections in this chapter. A schematic of the lift off process after development of the exposed resist is shown below in Figure 4.5.
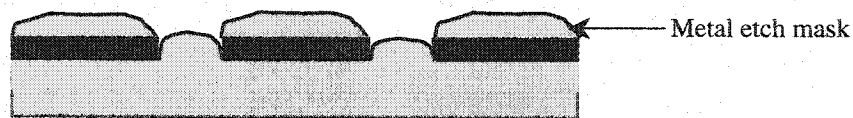
— Metal etch mask

Step 5: Evaporation of metal etch mask on the developed resist pattern
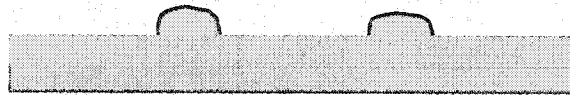
Step 6: Metal etch mask covering the pattern after liftoff

Figure 4.5: Steps involved in the metal liftoff process

In this process, a thin film of a metal etch mask is deposited after the exposure and development process of the patterned resist. The deposited metal fills up the trenches created by exposure and development and also covers the top of the unexposed resist as shown in Figure 4.5 (Step 5). The resist is then removed by dissolving in acetone. The metal sitting on top of the resist also gets stripped off along with the resist thus leaving metal in the desired pattern (Figure 4.5, Step 6). This metal layer later acts as an etch

mask during the process of dry etching and thus protects the waveguide pattern from being etched.

4.4 E-beam lithography

The next step is the all-important step of e-beam lithography where the gratings are patterned in the waveguide gaps defined in the optical litho step. The e-beam lithography is very critical as the spectral characteristics and working of the optical filter depends on the accuracy of this process. A LEO 440 SEM and Nanometer Pattern Generation System (NPGS), Figure 4.6, working at an acceleration voltage of 40kV and having a field size of 80 μm X 80 μm was used.
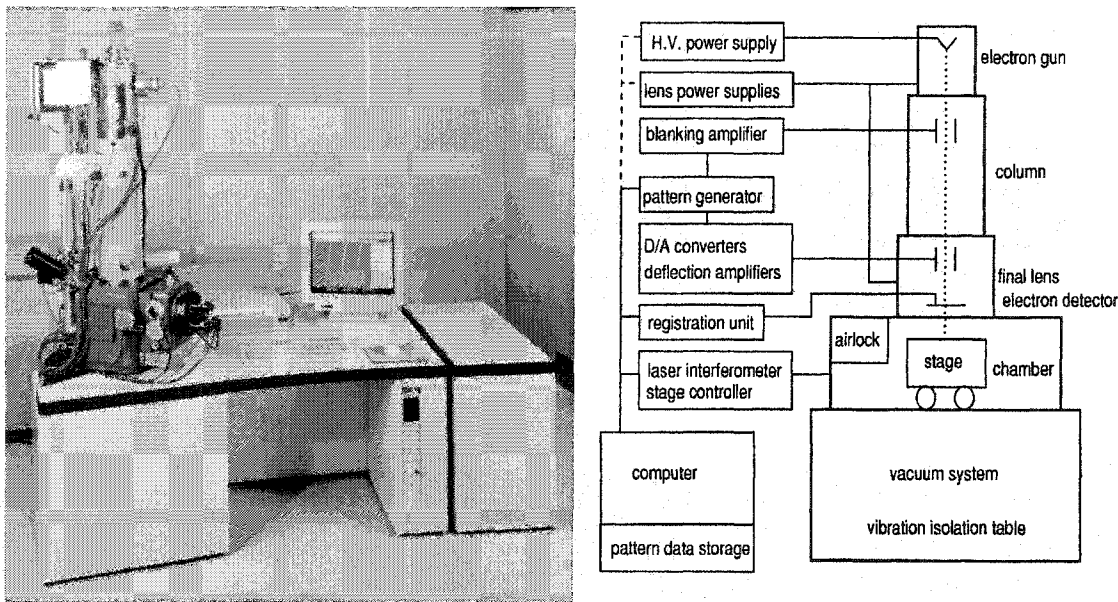
Figure 4.6: E-beam lithography system

In e-beam lithography, high-energy electrons are used for direct writing of the pattern on the wafers coated with electron sensitive resists. The ability of the system to write small feature size (beam spot diameter) of $< 600 \overset{o}{A}$ in addition to the precise control of exposure time and energy of the electrons used, are prime reasons for the high-resolution capability of the e-beam systems.

63

The e-beam lithography process could be divided into three different sections, namely:

1) Data preparation

2) Sample preparation and resist coating

3) Exposure

4.4.1 Data Preparation

Data preparation is the creation of an instruction set describing the pattern to be defined by the e-beam lithography system.

4.4.1.1 Pattern design

Patterns (gratings) were designed using DesignCAD, a commercial Computer-Aided-Design (CAD) software package. This program is a powerful tool for layout and editing of patterns of different shapes and sizes. In our case, grating patterns were designed by drawing a series of rectangles of varying dimensions corresponding to the refractive index modulation depth and duty cycle of each grating period. The pattern is then formatted to be compatible with the e-beam system for different exposure parameters (dosage type, exposure point spacing, etc.).

4.4.1.2 Run-file creation

Once the final DesignCAD pattern file is complete, a run-file is created. The run-file is used by the e-beam system. Here the different exposure parameters are set as shown in Figure 4.7. An 'area dose' is set for the grating pattern (series of rectangles). The 'area dose setting' results in the entire region within the rectangles being exposed as required for patterning. The approach of designing the pattern and the run file separately provides greater flexibility with varying the exposure conditions without having to change the pattern.
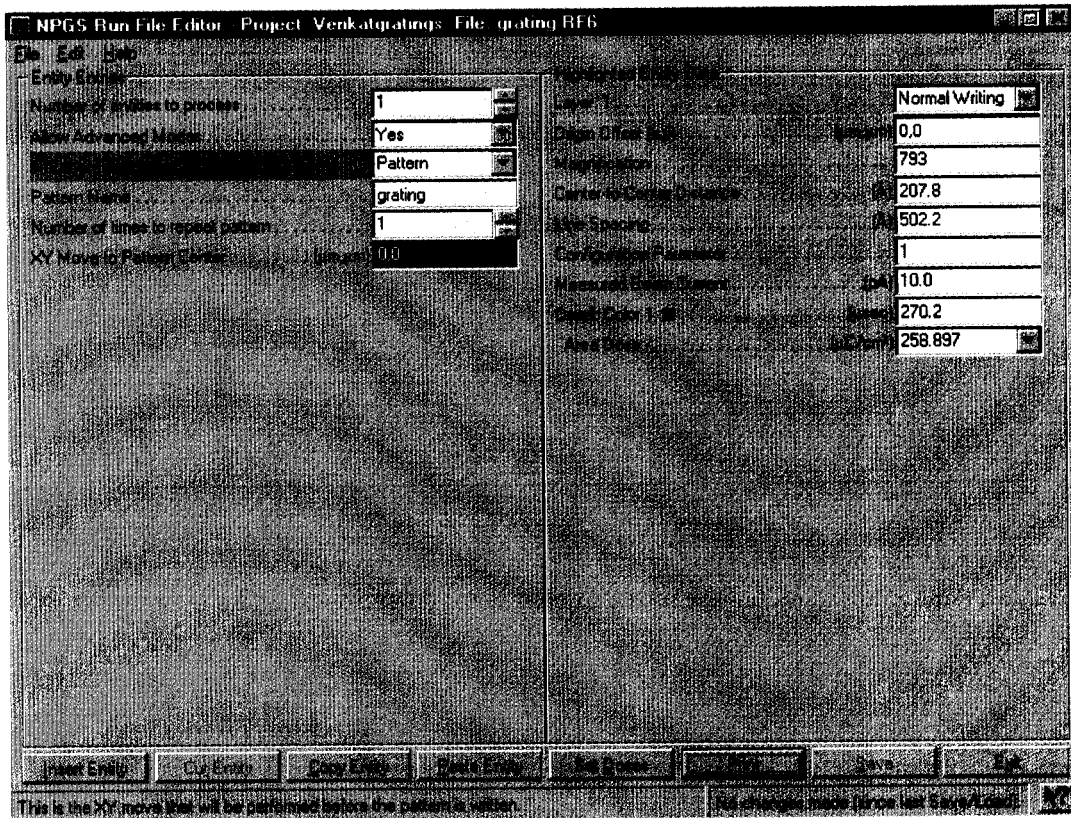
Figure 4.7: NPGS Run File editor window showing exposure parameters

4.4.2 Sample preparation and resist coating

The e-beam stage can only support samples of area 1 cm X 1 cm or smaller. Hence, the optically patterned SOI sample has to be diced into smaller sizes (<100 mm^2) to fit into the stage. These diced samples are later spun with an e-beam sensitive resist (Appendix VI), to enable direct writing of the grating pattern. The choice of proper resist depends on the following important considerations: resolution, sensitivity, tone and etch resistance. Poly Methyl MethAcrylate (PMMA), a positive resist, was chosen as the resist for our application because of its high-resolution capability. As discussed in Chapter 3, the grating response is very much dependant on the resolution of the pattern. PMMA provides flexibility in terms of its sensitivity to e-beams because of its commercial availability in different molecular weights (950K and 495K). However, PMMA is not highly resistant to dry etching. Thus a metal etch mask has to be used to protect the grating pattern during the subsequent etch steps.

65

4.5 Choice of thickness - resists and etch mask

The resolution of the e-beam lithography process not only depends on the spot size of the focused electron beam, but is also affected by the scattering of the electrons as they travel through the resist. Thus, to reduce such scattering and increase resolution, it is desirable to have a thin layer of resist. A thickness of 75-100 nm of the positive PMMA was chosen because of the strict requirement on the resolution of grating period definition. Given that another liftoff of a metal etch mask is necessary after e-beam lithography and that the resist is very thin, it is also required that the metal etch mask be very thin for good liftoff results. With the intended etch depth also being shallow as controlled by the single-mode condition (see Chapter 3), a metal thickness of 40 nm is adequate to protect the waveguide and grating patterns in the dry-etch step. Note that this is the same thickness as used for the etch mask defined in the optical lithography step.

4.6 Resist spinning

Two different concentration (C1 and C2) of PMMA were prepared. The formulations C1 and C2 represent 1% and 2% of PMMA in Chlorobenzene, respectively. The different concentration of resists yield different thickness for the same spinning speeds. Two different techniques for resist spinning were explored. In the first technique, a single layer of 950K PMMA C1 for a thickness of 75-100 nm is spun. The other technique involves spinning of two different layers of different PMMA, with the less-sensitive 950K PMMA C2 (thickness of 75 nm) spun on top of a high sensitive 495K PMMA C2 (thickness of 100 nm) as shown in Figure 4.8. The second technique is intended mainly to improve the efficiency of the liftoff process after e-beam lithography. Some plots of spin speed vs resist thickness for the 950K and 495K PMMA are shown in Figure 4.9.
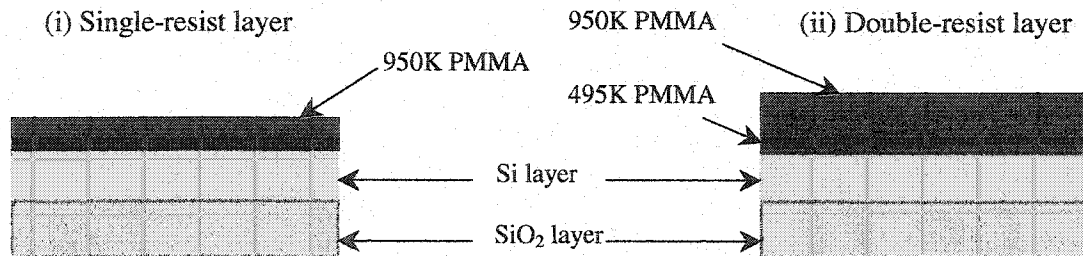
Figure 4.8: Two techniques of resist spinning
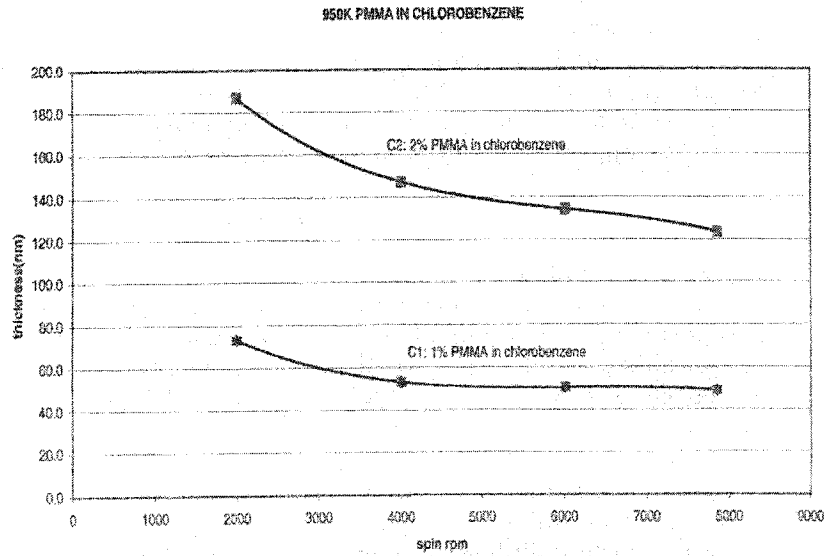
Figure 4.9:(a) Spin speed vs Resist thickness for 950K (C1 and C2) PMMA

(Source:[90])
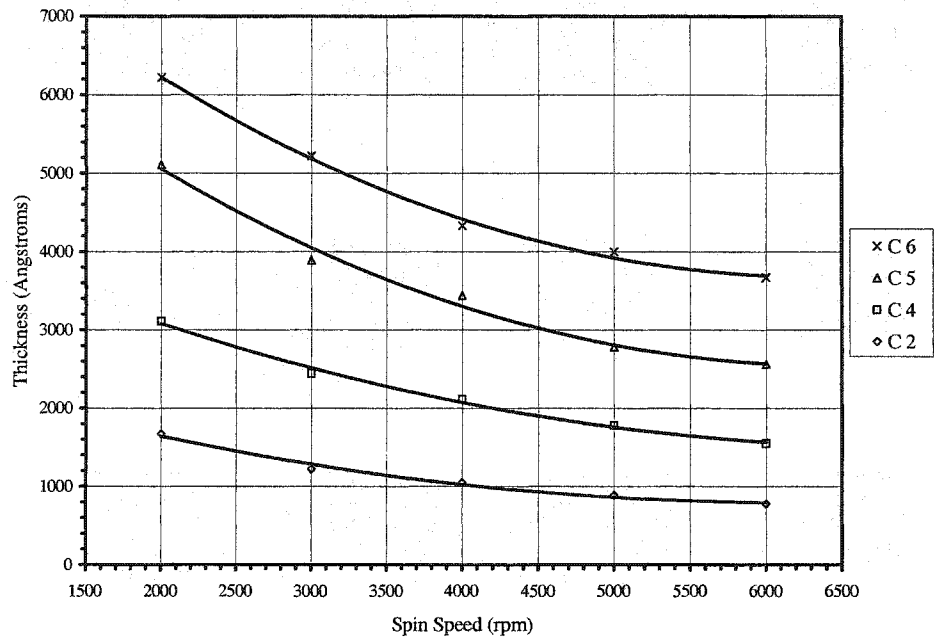
Figure 4.9(b) Spin speed vs Resist thickness for 495K (C2, C4, C5, and C6) PMMA

(Source:[90])

From the charts above, the spin speeds during resist coating for the two techniques are shown in Table 4.3:

Technique	Resist	Thickness	Spin Speed (rpm)
Single-Layer	950K C1	75 nm	2000
Double-Layer	495K C2	100 nm	4000
	950K C1	75 nm	2000

Table 4.3: Spin speeds to achieve different thicknesses for the 2 varieties of PMMA used

After coating, the resist is post-baked at 180°C for 5 minutes for better adhesion to the substrate, as was discussed in Section 4.2.

4.7 Exposure

The sample is loaded into the e-beam lithography chamber and an operating vacuum of 10^{-6} torr is achieved. The following chosen operating parameters were then set in the e-beam system:

Accelerating Voltage	40 kV
Beam Current	20 μA
Probe Current	10 pA

Table 4.4: E-beam parameters - initial setting

Probe current is the current from the e-beam reaching the sample. For high-resolution applications and samples that are sensitive to charge buildup (see Section 4.7.2) a value in the range of 10-20 pA is recommended. Small beam currents have smaller beam sizes, thus capable of writing small regions with high resolution. After the above initial settings, focusing is done on the sample to adjust the working distance and also to reduce

68

astigmatism. This is very critical as inadequate focus can badly affect the resolution of the written pattern. Improper focus results in the e-beam power being concentrated at a point outside the resist layer, as shown in Figure 4.10. The result is that insufficient energy is transferred from the electrons to the resist, thereby reducing resolution.
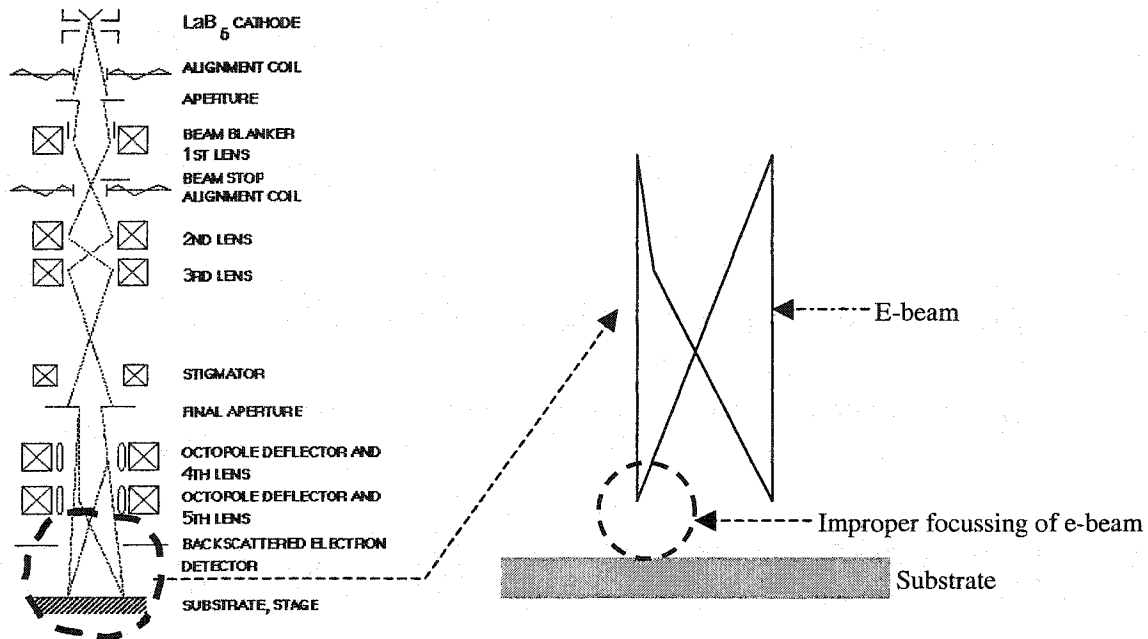
Figure 4.10: (a) Arrangement of lenses and deflection setup in e-beam lithography system, (b) Schematic showing improper focusing of the e-beam for two different scanning points

Focusing is performed on all four corners of the sample, and the average of the working distance (distance between e-beam gun and resist layer) is used. Once the focussing on the sample has been done, the substrate and the stage have to be aligned in order to maintain high angular alignment with the waveguide pattern formed previously by optical lithography.

4.7.1 Alignment

Initially, the focusing is done on the parallel reference line (see Figure 4.11). This reference line is used to ensure the substrate is in proper alignment with the stage.
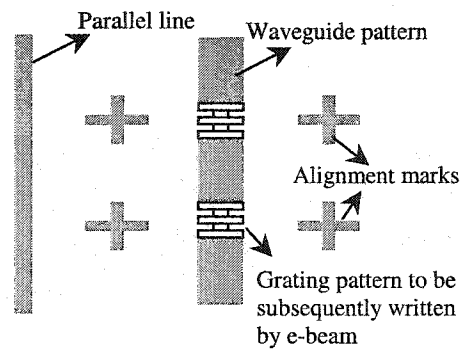
Fig 4.11 (a): Waveguide pattern written with Optical lithography
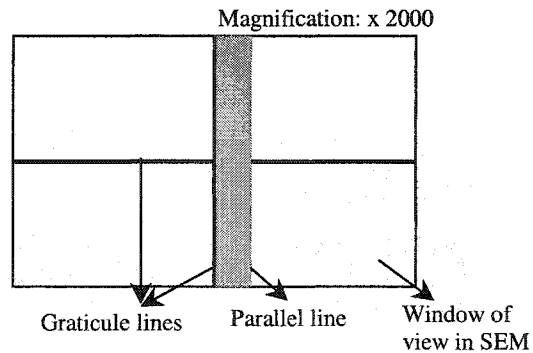
Fig 4.11 (b): Substrate is aligned for its orientation using the parallel line
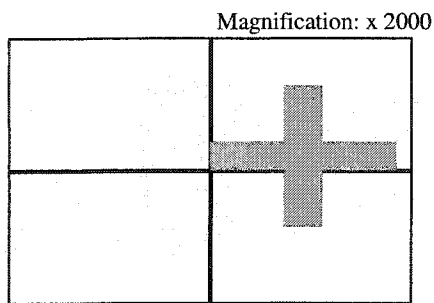
Fig 4.11 (c): Stage is moved to focus on the alignment mark
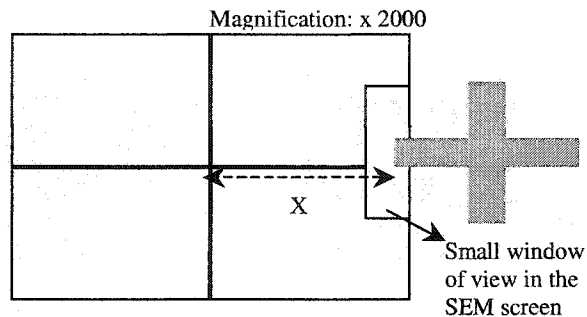
Fig 4.11 (d): Center of grating is located using the alignment mark
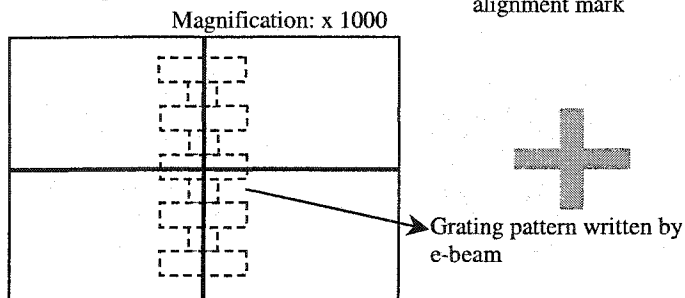
Fig 4.11 (e): The grating pattern is written at a lower magnification

Figure 4.11: Steps involved with aligning the waveguide and grating pattern using the alignment marks

Once this is done, the stage is moved to focus on an alignment mark adjacent to the grating section to be written (the crosses in Figure 4.11) (The alignment marks were

placed at a preset distance from the reference line). Focusing is done by opening a SEM window at a high magnification (x 2000) on the edges of the cross (alignment mark). Then, using the same magnification window, the stage is further moved to see the second cross marks on the other side of the grating section, which is also at a predefined distance from the first cross mark. This step is to ensure that the stage and the sample are in proper angular alignment. The beam is then blanked and the stage moved a predefined distance, to center the grating pattern within the center of the gap allotted for the grating, as shown in the Figure 4.11. The SEM control is then switched to the external computer storing the NPGS data (RUN file) of the grating pattern (Section 4.4.1.2). The exposure of gratings is done at a lower magnification (x 1000). At this time, the external computer takes control of the beam blanking and the beam deflection system and controls the writing of the pattern.

This technique of alignment and exposure will maintain the angular alignment of the grating pattern. However, there is a possibility of a slight gap being introduced between the waveguide and the grating pattern because of the small errors introduced during mask fabrication and optical lithography. A simple technique is proposed to remove this possible gap. It involves pre-compensating for this possible gap during data preparation. The end segments of the grating pattern (last rectangles forming grating duty cycles in the data) are designed to have longer dimension along the length of the grating than required. This ensures the gratings make contact (overlaps) with the waveguides. By using the two techniques above, the phase coherence of the gratings can be maintained without affecting the spectral responses.

Once exposed, the pattern is developed in a mixture of Methyl Iso Butyl Ketone (MIBK) and Isopropyl Alcohol (IPA) in a ratio of 1:1 for 30 seconds. The sample is then post-baked on a hot plate at 100°C for 60-90 seconds. A test-grating pattern with a grating period of 200 nm exposed for a different area dosage is shown in Figures 4.12 and 4.13.
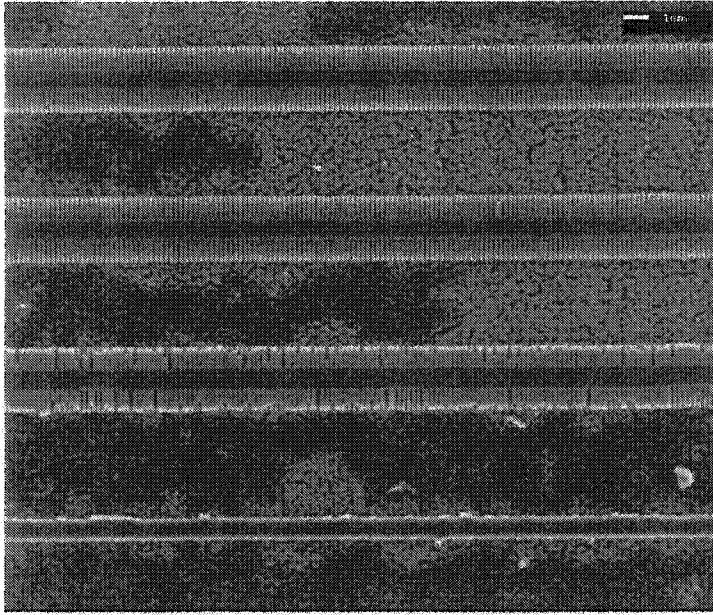
Figure 4.12: SEM picture of grating patterns written for different dosages (dose increases from bottom to top (275 $\mu C/cm^2$, 350 $\mu C/cm^2$, 425 $\mu C/cm^2$ and 500 $\mu C/cm^2$))

Figure 4.13: SEM picture showing a closer look at the grating fingers for grating pattern formed by a dose of 500 $\mu C/cm^2$

The dosages used were 500 $\mu C/cm^2$, 425 $\mu C/cm^2$, 350 $\mu C/cm^2$ and 275 $\mu C/cm^2$, respectively, for each pattern from top to bottom in the SEM Figure 4.12. It is noted that as the dosage increases, the pattern is more well-defined. Appropriate dosage level has to be chosen. Lower dosage doesn't provide enough electrons to break the molecular linear chain of the resist in the exposed regions, resulting in very poor resolution. Figure 4.13 shows a closer look of the grating fingers for the pattern written for the highest dose (500

$\mu C/cm^2$). It is seen that the width of the grating finger is 120 nm and the spacing between the fingers is 80 nm, while they were both supposed to be 100 nm each. The reasons for such overexposure are shown in the Figure 4.14.
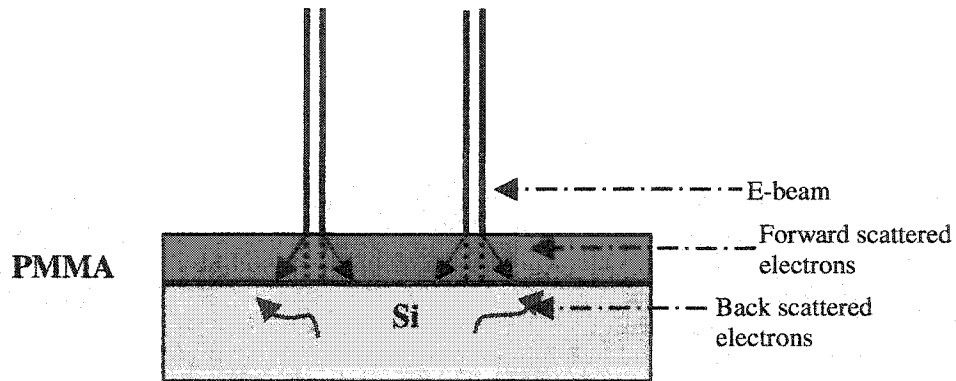
Figure 4.14: Reasons for overexposure

When the e-beam strikes PMMA, instead of it penetrating straight and dissolving the resist, electrons are scattered and expose a wider region. The sensitivity of the conventional e-beam resists (PMMA) is in the order of 10^5 C/cm^2. With electron energies of 40 kV, the free path of electrons is 10 μm. With thin PMMA thickness, most of the electrons reach the substrate and a majority of those get reflected from the atoms of the substrate. This results in a much wider region being exposed than intended and hence the cause for the over exposure seen in the SEM Figure 4.13. Such over exposures could be reduced by (i) having a very thin coat of the PMMA to reduce forward scattering, (ii) using an optimal dose to reduce back scattering, and (iii) achieving better focus to increase resolution. This explains the reason for us using a PMMA thickness of 75 nm.

4.7.2 Possible charging of substrate

Since the bulk of the highly energized electrons reach the substrate, there is a possibility that these electrons will actually penetrate the substrate and build up a charge. Such charging could effectively cause a build up of stress and result in breaking the substrate. In order to prevent such charging effects, it is a general practice to sputter a 5 nm thick

layer of Gold (Au) on top of the PMMA layer. This Au layer acts as an anti-charging layer dissipating any charge buildup. This was done in all cases discussed in this thesis.

4.8 Liftoff for grating etch mask

Following development of the PMMA resist, evaporation of the metal etch mask is carried out to a thickness of 40 nm. Both single-layer and multi-layer PMMA samples were evaporated with this metal layer, followed by a liftoff. Both of these resist techniques provided good results provided the thickness of etch masking metal was less than the resist thickness. SEM Figures 4.15 (a) and 4.15 (b) show the results of liftoff for the two techniques.

(a)   (b)
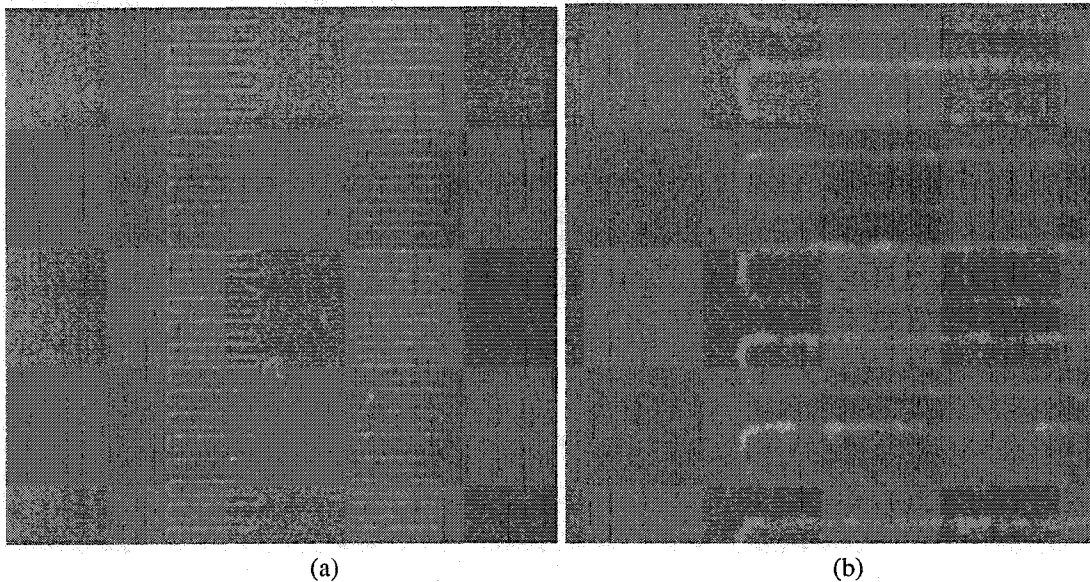
Figure 4.15: (a) SEM picture of gratings after liftoff using single-layer resist, (b) SEM picture of gratings after liftoff using double-layer resist

Though both the techniques yield good results for the liftoff, the double-layer resist technique is preferred for better liftoff repeatability. However, there is a trade-off between the liftoff quality and the effects of overexposure on the gratings, as a result of the increased resist thickness with multiple resist layers.

4.9 Pre-compensation technique for overexposure

A simple method could be adopted to overcome overexposure but still use the multiple-resist layer technique. As seen from Figure 4.13, the overexposure mainly affects the duty cycle of the gratings. The finger width increases on overexposure and the spacing between fingers gets reduced proportionately as a result. To perfectly control the spectral response characteristics of the gratings, the duty cycle of gratings have to be maintained. A simple pre-compensation technique involves compensating for the change in duty cycle during the data preparation stage itself. However, it is required to run a test writing process for a fixed set of parameters to find the amount of overexposure. Thus, it is observed that the data preparation stage is a very crucial step. It provides opportunities to compensate for this overexposure and also to ensure that the written gratings make contact with the waveguides (as discussed above).

4.10 Thin film (etch mask) formation
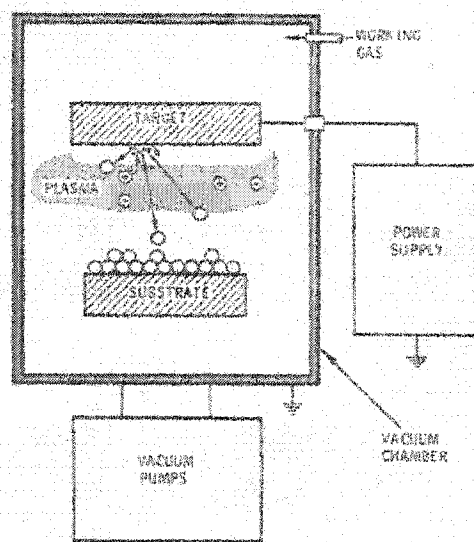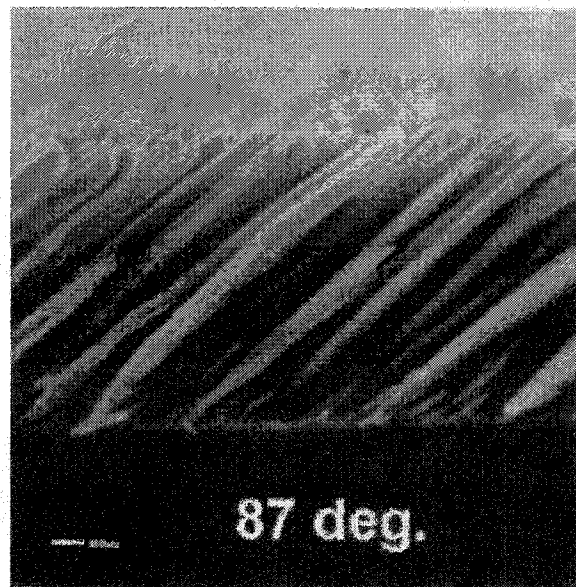
(a)   (b)

Figure 4.16: (a) Principle of Sputtering, (b) SEM picture of film formed by evaporation (Source: [91])

The choice of forming the etch mask layer by evaporation rather than sputtering is driven by the characteristics of films formed by the two methods. The irregular arrangement of the atoms in the film formed by sputtering is shown in Figure 4.16 (a).
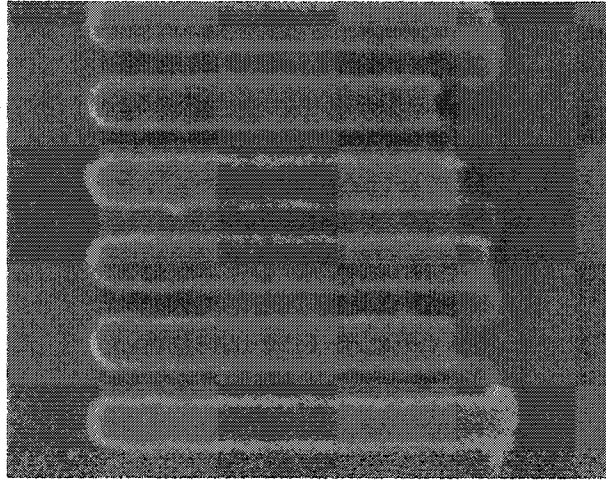
Figure 4.17: Liftoff performed on a etch masking film formed by Sputtering

Sputtered films are generally not compatible with liftoff of small features. The metal film from unintended regions also gets lifted-off as a result of this above-mentioned irregular arrangement. This is especially problematic for the ultra-thin resists used here. A SEM picture of the liftoff performed for a film formed by sputtering is shown in Figure 4.17. Evaporation, on the other hand, results in uniform columnar structure (depending on the angle of incidence) as shown in Figure 4.16 (b). Hence, liftoff of unintended regions is less of a problem for evaporated films.

4.11 Reactive Ion Etching (RIE)

To realize the final device, the wafer is etched down using the metal etch mask to form the rib and grating structure. A reactive ion etch (RIE) using Fluorine chemistry (C_4F_8 and SF_6) with Oxygen (O_2) was initially used to test and optimize the etch process. The Recipe I for this etch process is given in Table 4.5. The Figure 4.18 shows the principle of working of the RIE.
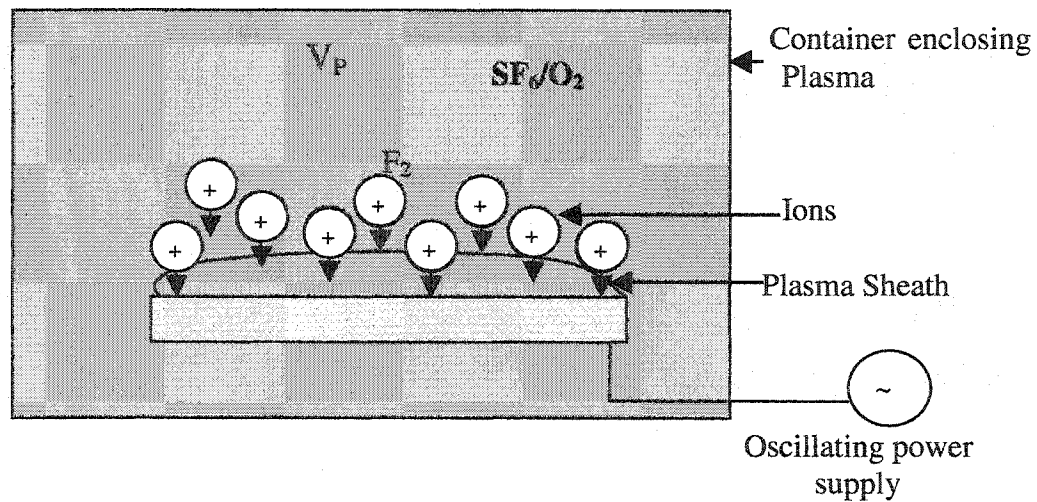
Figure 4.18: Principle of working of the RIE

Parameters	Etch step	Deposition Step
Gas flow rate (sccm)		
SF$_6$	75	
C$_4$F$_8$		50
Pressure (mTorr)	30	30
ICP Power (Watts)	450	450
He backing (Torr)	15	15
Forward Power (Watts)	50	20
Time (seconds)	5	3

Table 4.5: RIE Recipe I

Table 4.5 gives the standard commercial recipe for the two-step (etching and polymer deposition) Bosch etching process. The etched silicon (etched grating structure with Al etch mask) using this recipe I is shown in the SEM pictures Figure 4.19.
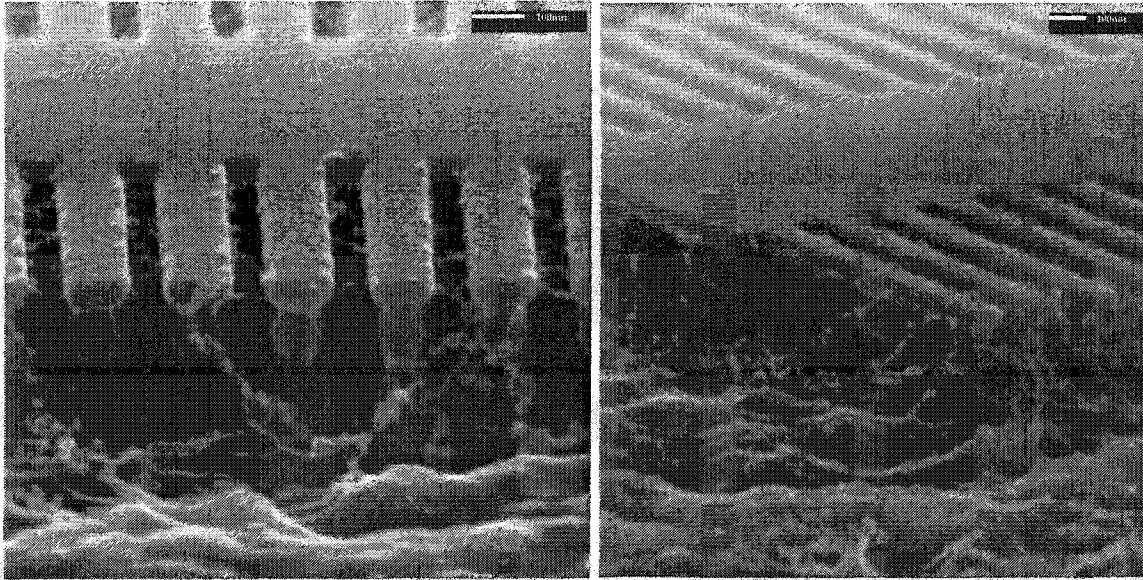
Figure 4.19: SEM picture showing etched grating structures - Etching done using Recipe I

As could be seen from Figure 4.19, it is obvious that the etching was not perfect. Even though the sidewalls are pretty much anisotropic and the edges of the gratings well defined, it is noted that the sidewalls are very rough. Such roughness could lead to a large amount of scattering loss. Some possible reasons for the improper etch are excess reactive gas (Inductively Coupled Plasma (ICP)) and too low vacuum pressure in the chamber. This results in the scattering of ions from etch mask and other Si regions creating rough sidewalls. To optimize the etch further, more tests were performed by feeding less amount of reactive gas (Table 4.6) and simultaneously other etch masking materials like Chromium (Cr) and Gold (Au) were tested.

Parameters	Chromium	Gold
SF_6 flow rate (sccm)	60	60
O_2 flow rate (sccm)	5	5
DC Bias (Volts)	38	38
Chamber pressure (mTorr)	10	10
ICP Power (Watts)	550	750
Etching time (seconds)	30	30

Table 4.6: RIE recipe II and III using Cr and Au etch masks respectively

(a)

(b)

(c)

(d)
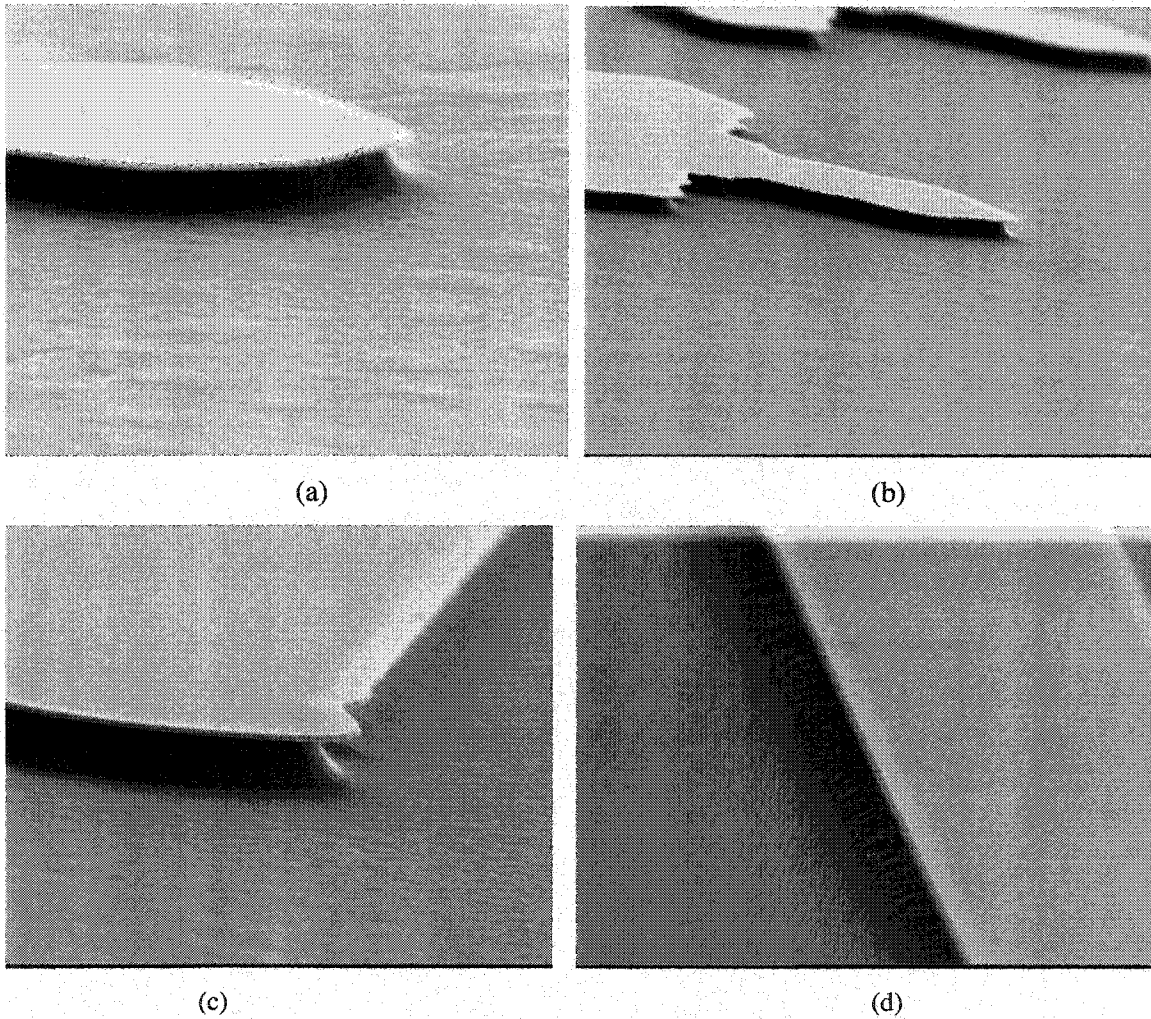
Figure 4.20: (a) and (b) Etched waveguide using Cr etch mask (Recipe II), (c) and (d) Etched waveguide using Au etch mask (Recipe III)

It is seen from Figure 4.20 that in all cases, silicon was etched much more quickly than the etch masking metal. Also, with the etch depth being very shallow, it is concluded that use of different etch masks doesn't make any difference to the quality of the etching in our case. However, it is recommended that Au be used as etch masking metal as it is easily visible through the PMMA, which helps in locating cross marks during alignment.

4.11.1 Reasons for Isotropy

The isotropy in the sidewalls in Figure 4.20 is believed to be caused by etching for a longer duration than is optimal. The initial etching is carried out by the highly energized

ions which remove Si by physical etch (i.e., the momentum of the ions physically ejects Si atoms at the surface). However, when etching is carried out for longer periods of time, then chemical etching process takes over, resulting in large undercut and isotropy of the sidewalls [92]. A possible way to reduce such undercuts and improve the verticality of the sidewalls (but still obtain the required etch depth) is to reduce the etching time, increase the flow rate of the reactive gas, and use an optimal plasma for etching. It was necessary to run numerous etch tests in order to find optimal parameter values.

4.11.2 Optimized values of etching on SOI samples

To further study the causes of undercut and isotropy, two different ICP values and a reduced etch time were chosen, and etching was carried out on SOI samples to form the rib waveguides. The etch recipes are tabulated in Table 4.7:

Parameters	Recipe IV	Recipe V
SF_6 flow rate (sccm)	60	60
O_2 flow rate (sccm)	5	5
DC Bias (Volts)	38	38
Chamber pressure (mTorr)	10	10
ICP Power (Watts)	750	550
Etching time (seconds)	20	20

Table 4.7: RIE Recipe IV and V
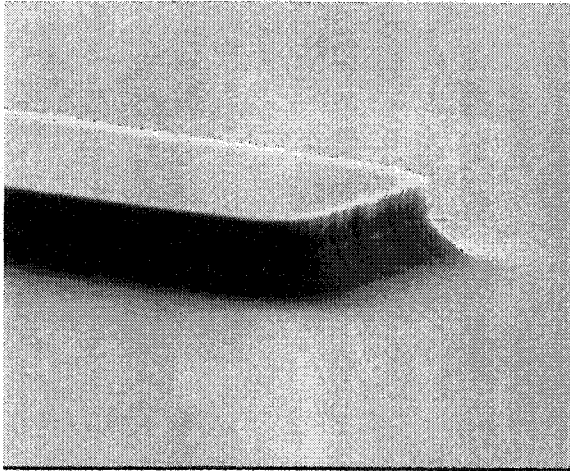
(a)
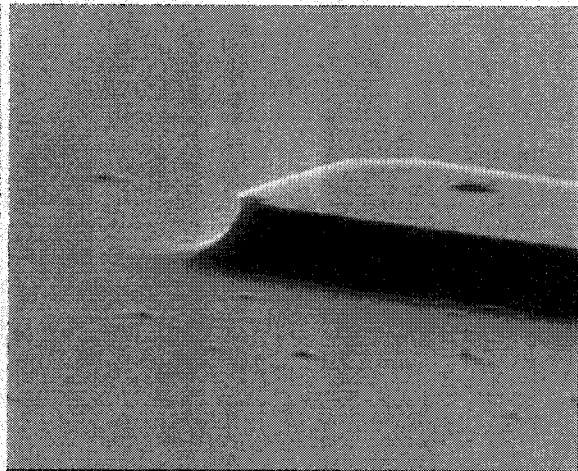
(b)
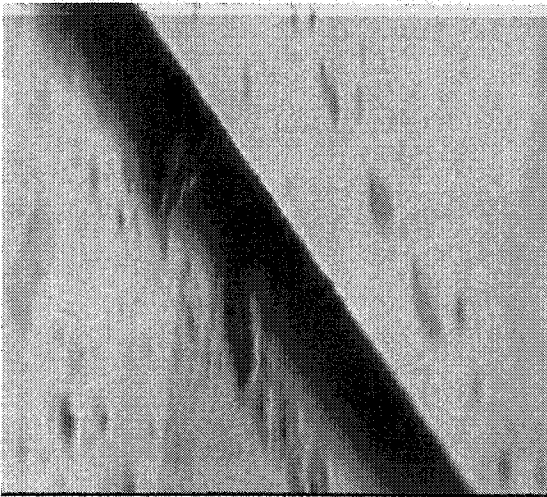
(c)
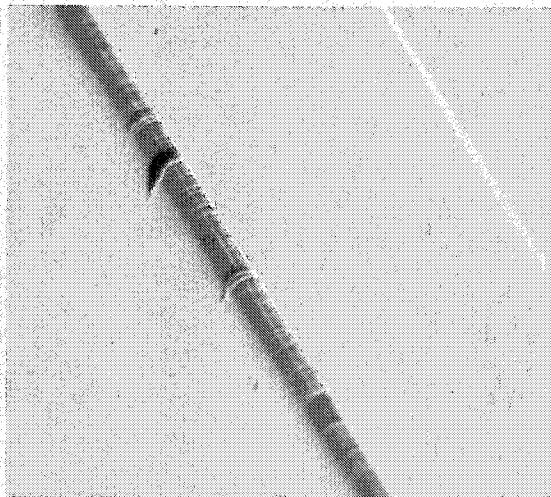
(d)

(e)
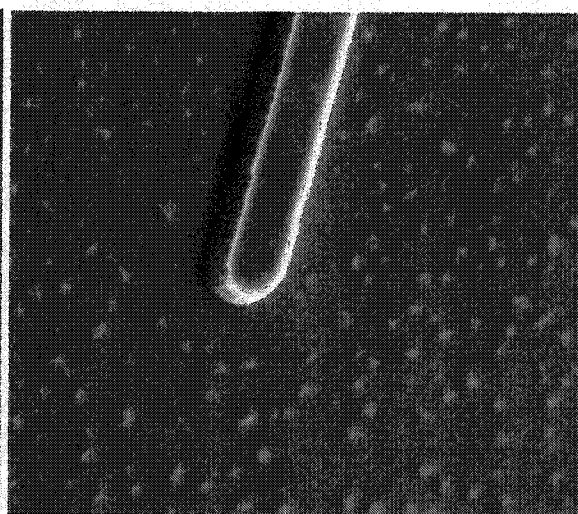
(f)

Figure 4.21 (continued)

81
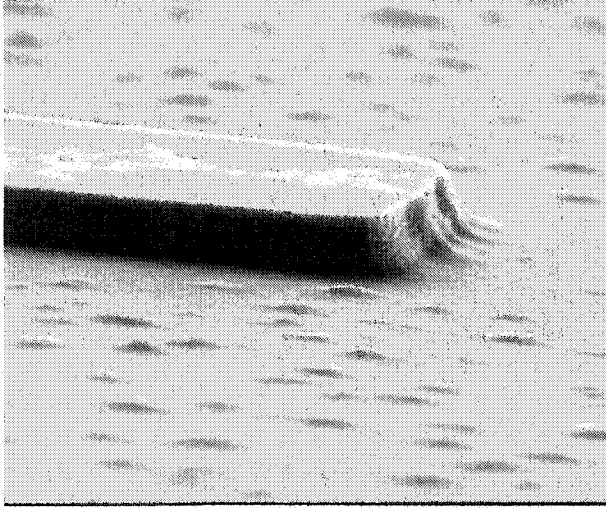
Figure 4.21: (a)-(d) Etched waveguides on SOI using Recipe IV, (e)-(g) Etched waveguides on SOI using Recipe V

(g)

On comparison of the two RIE etch results, it is confirmed that the isotropy in the sidewalls is a consequence of longer etch periods and higher ICP than required. However, the slight roughness in the sidewalls for the RIE etch with Recipe V was caused by the wet etch used to strip the metal etch mask from the top of the Si rib, to form the final waveguide.

Thus, it is concluded from our results that there is always a trade-off between the roughness of the sidewalls, etch depth and the undercut during the RIE process. A balance between all these is achieved by choosing the optimal values for the etch parameters depending on the appropriate application of the device. However, it needs to be emphasized that it is very difficult to obtain a perfect etch recipe.

4.12 Oxidation as a method for sidewall smoothening

A method to smoothen the sidewalls of the etched waveguide and grating structures by oxidation at high temperatures was explored [93]. Steam oxidation at a temperature of 1050°C was carried out to form a ~100 nm thick oxide layer. The high temperature aids in the indiffusion of the oxygen atoms into the voids of the rough sidewalls thereby smoothing them. Some SEM pictures are shown in Figure 4.22, showing the results of steam oxidation on etched features alongside those before oxidation. On comparison, it is noted that there has been some reduction in the roughness of the sidewalls after the

oxidation process. Also, the silicon surface appears to be smoother following oxidation. These preliminary results suggest that oxidation might be a promising technique for improving these Si microstructures, but further study is required. It is believed that oxidation for a longer duration of time could effectively further reduce this unevenness.

(a)   (b)

(c)   (d)
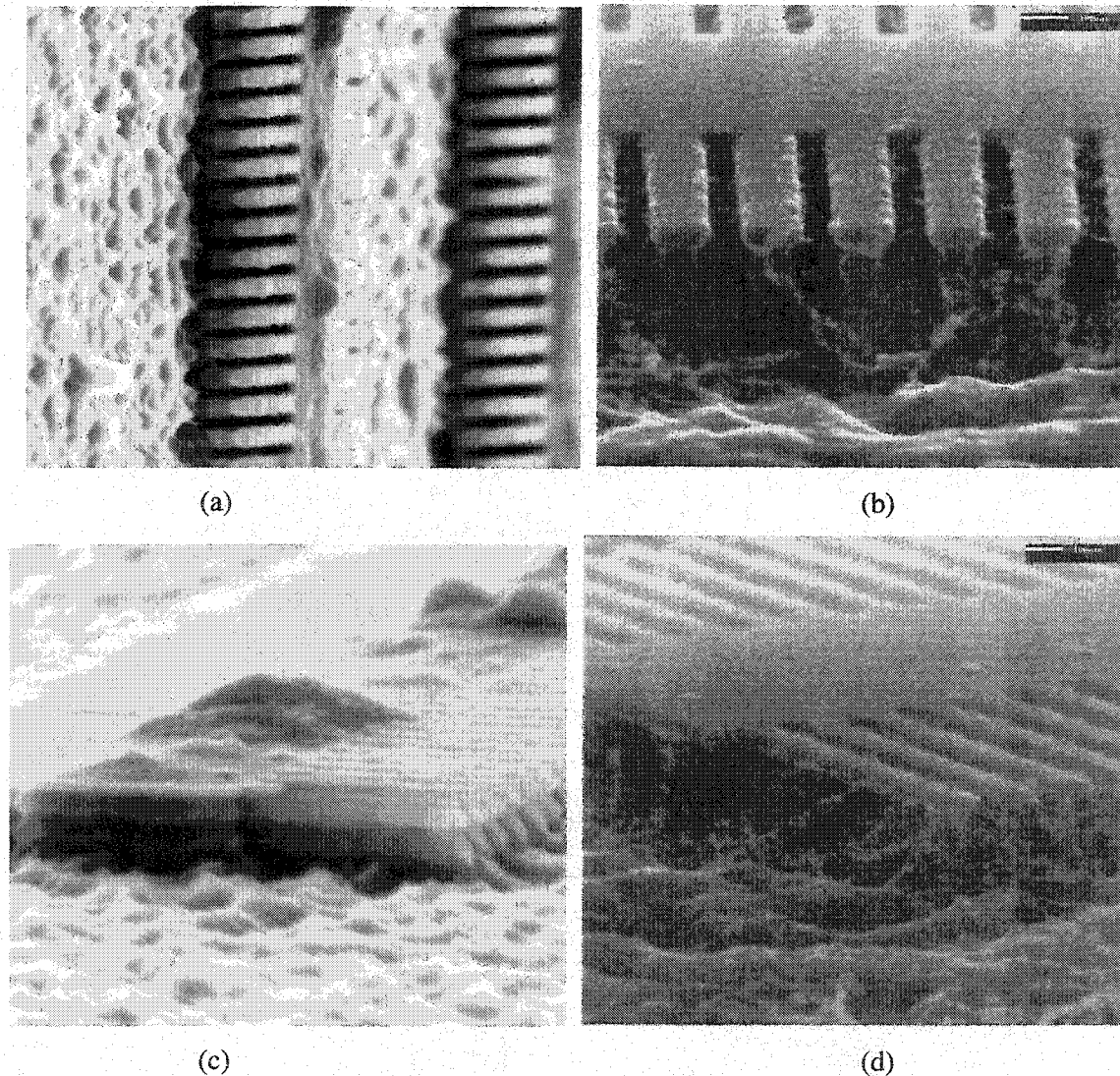
Figure 4.22: (a) and (c) Etched grating structures after oxidation, (b) and (d) Etched grating structures before oxidation

Even though the oxidation process produces improvement in the sidewall feature, they pose some difficulties. The difficulties arise with the size of the samples and the effect of a thicker oxide layer on the performance of the waveguide and the grating device. The

symmetric waveguide (with oxide layer as the substrate and the upper cladding) could actually yield a symmetric mode profile where a high percentage of the mode power is confined in the rib section. However, the oxide layer is formed at the expense of the Si layer, thereby affecting the $\frac{h}{H}$ ratio and as a consequence the single-mode condition (see Section 3.1). Thus, oxidation would need to be incorporated into the overall design of the waveguide grating structures.

5. Waveguide Characterization and Analysis

This chapter deals with the characterization of the optical rib waveguides formed on SOI substrates.
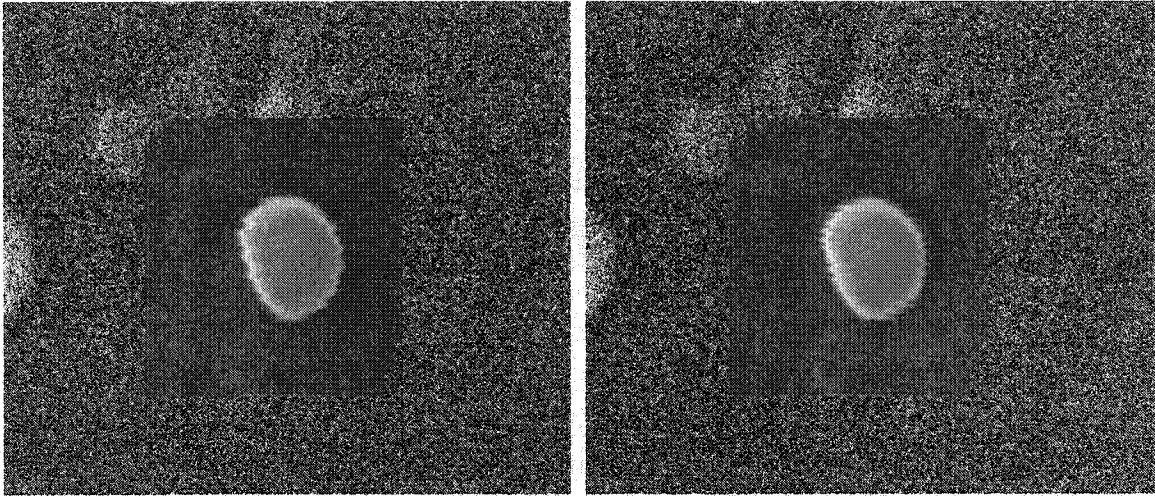
Figure 5.1: SEM pictures showing vibrations in the e-beam lithography system while focusing on circular objects on a SiCu sample

Optimization of fabrication parameters and processes was discussed in the previous chapter. However, unfortunately, the final device couldn't be fabricated because of vibrations encountered with the e-beam lithography system after the initial testing and optimization of the e-beam process (this was due to a move of the e-beam facility that occurred part way through the work). Huge vibrations in the e-beam were observed. Figure 5.1 shows SEM pictures that illustrate the vibration problems. The central features were intended to be circles with 300 nm diameter. It is seen that instead of proper circles, vibrations of approximately 40-50 nm are observed in the SEM. As was seen from the simulation results in Chapter 3, the grating devices under study require great accuracy for proper operation. With vibrations in the order of 40-50 nm, it was impossible to fabricate the final device and get any useful results to study their behavior. Thus, only the SOI rib waveguides were fabricated and tested.

5.1 SOI rib waveguide characterization

The setup used for the characterization of the SOI rib waveguides for 1550 nm wavelength is shown in Figure 5.2. It consists of the following:
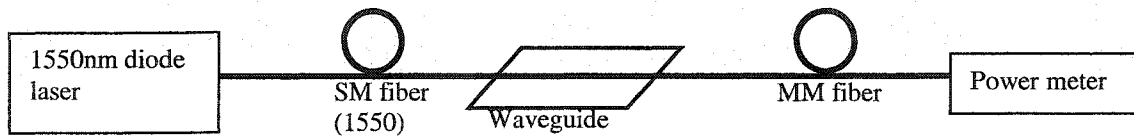
Figure 5.2: Schematic showing setup for waveguide characterization

1) A 1550 nm laser

2) A 9 μm diameter single-mode (SM) fiber to couple light into the waveguide

3) A vacuum chuck arrangement to hold the sample

4) A 50 μm diameter multi-mode (MM) pickup fiber to collect light from the other end of the waveguide and

5) A power meter to measure the power in the light emerging from the waveguide

5.1.1 Characterization procedure

To measure the amount of power launched into the waveguide, the input SM 1550 nm fiber and the output MM fiber were brought in close proximity and were moved around until the power meter reading showed a maximum. The power launched from the SM fiber was 10.5 mW. Once the input power was measured, the light was coupled into the waveguides through the set up shown in Figure 5.2. The input and the output fibers were attached to micropositioners, which were adjusted for optimal transmission through the test waveguide.

The results of the characterization are tabulated in Table 5.1:

Input power: 10.5 mW

Waveguide Width (μm)	Output Power for 5 mm long waveguides (mW)	Output Power for 2.5 mm long waveguides (mW)
1.0		
1.2	No output observed	No output observed
1.4		
1.6	0.25	0.26
1.8	0.30	0.30
2.0	0.32	0.33
2.2	0.33	0.28
2.4	0.38	0.39
2.6	0.43	0.47
2.8	0.48	0.49
3.0	0.54	0.55

Table 5.1: SOI rib waveguide characterization results
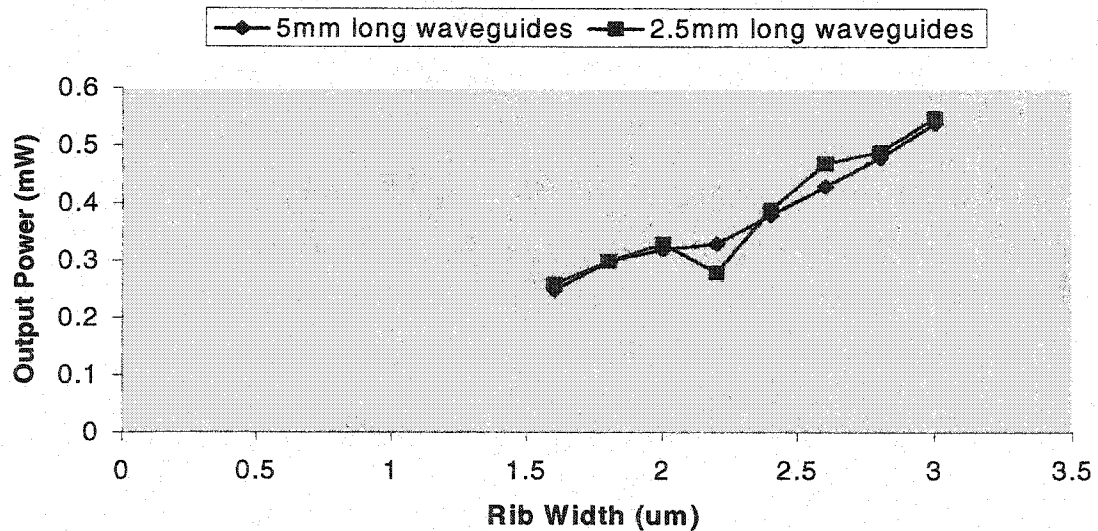
Figure 5.3: Plot of rib width vs. output power

5.2 Analysis of results

It is seen from Figure Table 5.1 that, for the waveguide with the rib width of 3 μm, a 13 dB loss is observed. It can also be seen from Table 5.1 and Figure 5.3 that the length of the waveguides actually doesn't make much difference to the power transmitted by the waveguides. This implies that propagation loss (including scattering and material absorption) is negligible relative to the coupling loss.

The main sources of the 13 dB insertion loss (for the 3 μm wide waveguide) are discussed in the following sections.

5.2.1   Coupling loss

It could be seen from the results of characterization in Table 5.1 that the main source of insertion loss is inefficient coupling from the fiber to the rib waveguide. Some of the general forms of coupling loss usually encountered shown in Figures 5.4, 5.5 and 5.6. In the figures, two identical waveguides are illustrated. However, the same general arguments hold for coupling between fiber and an SOI waveguide, as is the case here. As discussed below, the mode mismatch between fiber and the SOI waveguide is a main source of coupling loss.
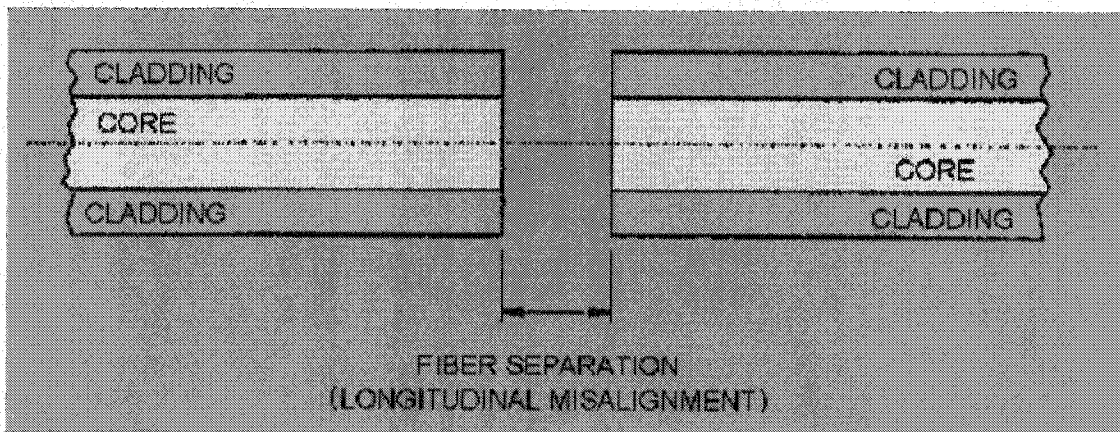
Figure 5.4: Schematic of source for coupling loss as a result of waveguide separation (Source [94])
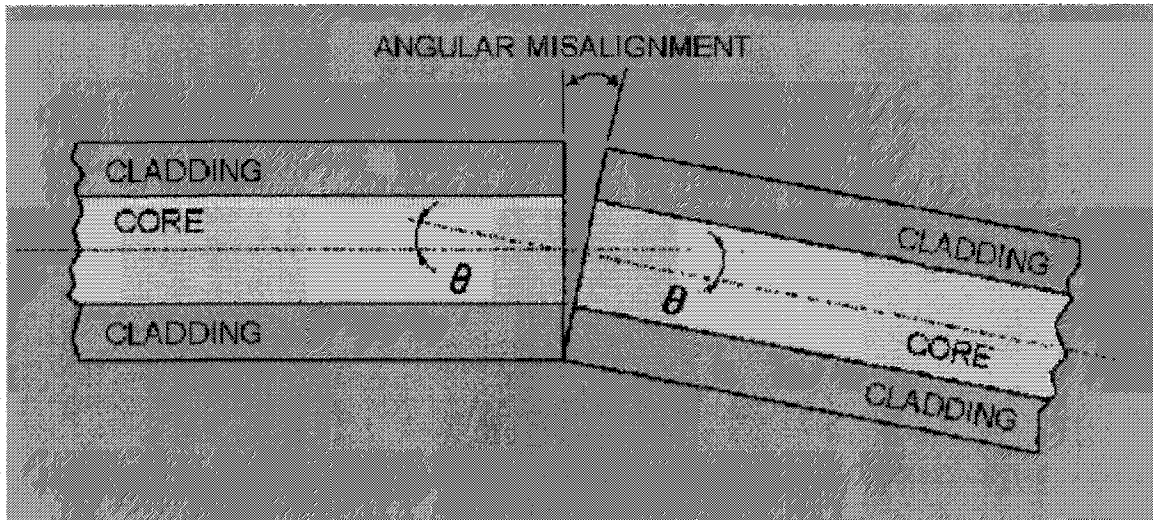
Figure 5.5: Schematic of source for coupling loss as a result of angular misalignment (Source [94])
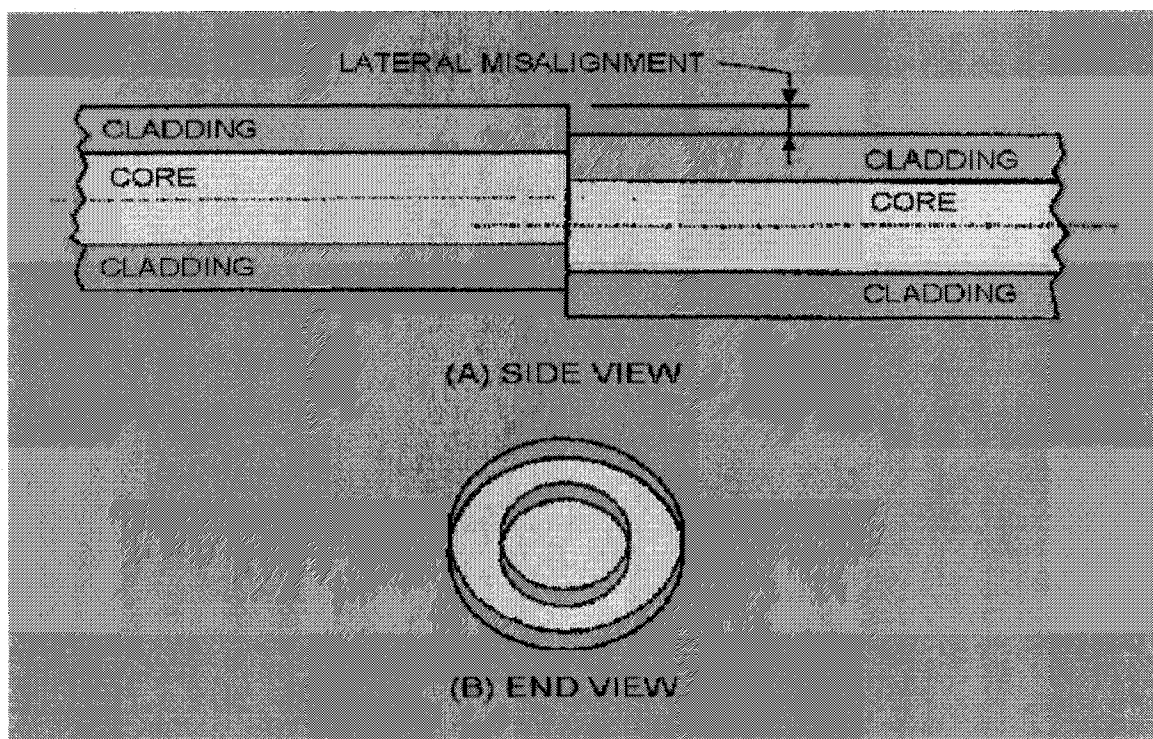
Figure 5.6: Schematic of source for coupling loss as a result of lateral misalignment (Source [94])

As noted above, a 9 µm diameter fiber was used to couple light into the SOI waveguides. The large difference in the fiber diameter and the rib width as well as the shape of the

fundamental modes in the fiber and the rib guide are predicted to be the prime reason for the coupling loss. This is seen from the fact that the output power increases with increase in the rib width.

A simulation was done using a commercial software (PROMETHEUS) to study the coupling loss into different widths of waveguide from a 9 μm input fiber for a $\frac{h}{H}$ of 0.9 (see Section 3.1.2). A plot of Output power vs Rib width from this simulation for an input power of 10.5 mW is shown in Figure 5.7.
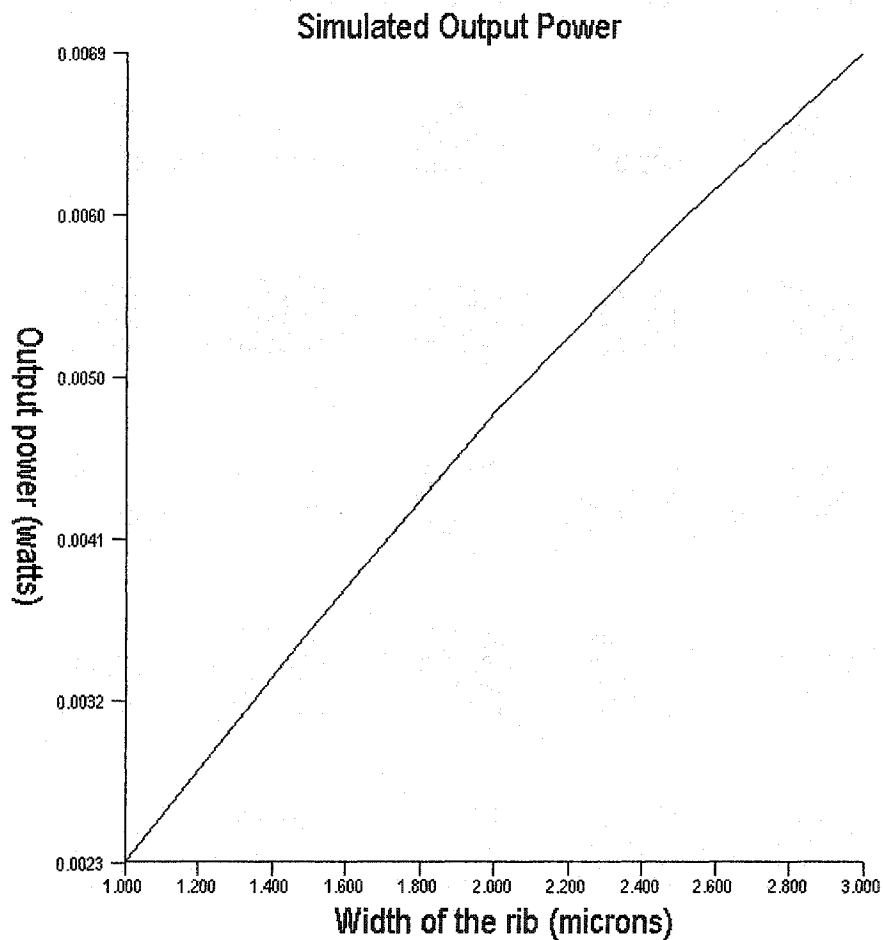
Figure 5.7: Output power vs. Rib width

It is seen from the above plot that for a rib width of 3.0 μm, the coupling loss from a 9 μm fiber is found to be ≈2.0 dB and constitutes ~15% of the 13 dB total loss observed.

5.2.2 Reflection loss

In addition to the coupling loss, optical power may be lost by Fresnel reflection. This reflection occurs when light is incident on a discrete interface between two media having different refractive indices. Fresnel reflection is caused by a step change in the refractive index that occurs at the interface. For a normal ray, the fraction of reflected to incident power is given by [95]

$$R = \frac{\left(n_1 - n_2\right)^2}{\left(n_1 + n_2\right)^2} \qquad (5.1)$$

where R is the fraction of the incident light reflected at the fiber and n_1 and n_2 are the indices of the two media. For our SOI waveguides, the amount of Fresnel reflection is calculated to be:

$$R = \frac{\left(3.5 - 1.0\right)^2}{\left(3.5 + 1.0\right)^2} = 0.308 \qquad (5.2)$$

where n_1 and n_2 are refractive indices of Si and air. Thus, it is predicted that upto 60 % (i.e. ≈ 4 dB) of the launched power is lost due to the Fresnel reflections alone (2 dB at each the input end and output interface). This again is a huge contributor (35%) for the measured losses in the waveguides.

5.2.3 Scattering loss

The third source for the losses observed is the scattering losses at the ends of the waveguide during coupling. Figure 5.8 shows SEM pictures showing surface roughness of the ends of the rib waveguide formed on SOI substrate as a result of dicing.

(a)   (b)
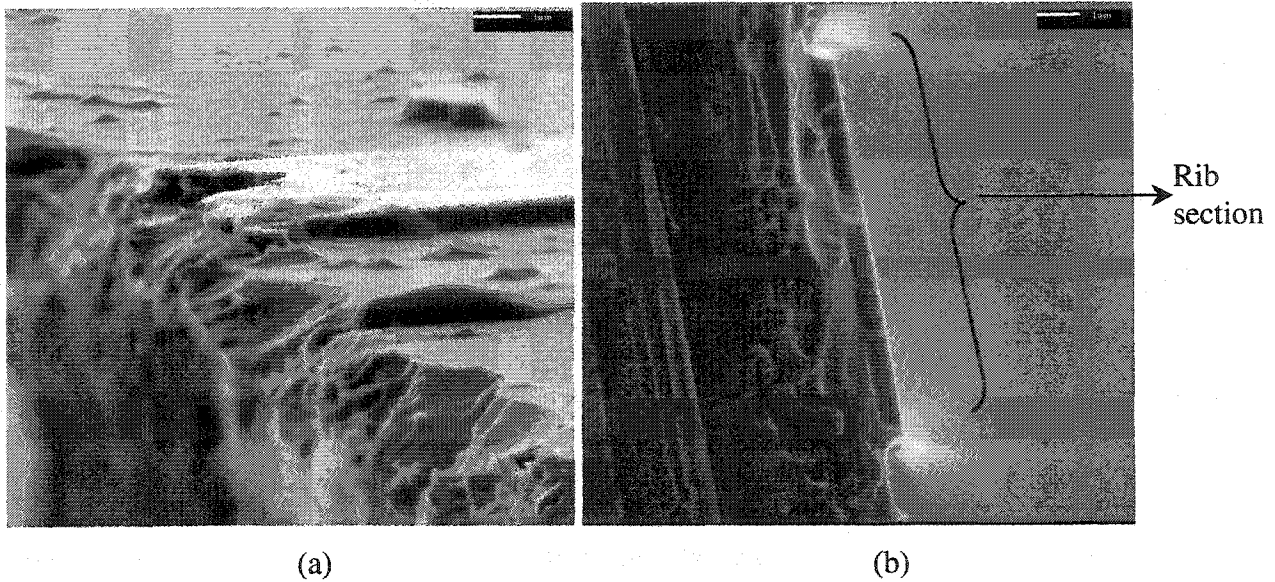
Figure 5.8: SEM pictures showing roughness at the ends of rib waveguide as a result of dicing

Such rough edges can scatter the coupled light and is a major reason for the losses measured. Based on these images, it is conceivable that the remaining loss could be attributed to this scattering.

5.3 Some possible solutions to reduce coupling losses

The coupling losses could be reduced significantly by using an input fiber with a better modal overlap to the SOI waveguides, such as a tapered fiber. Reducing the separation between the waveguide and the fiber could also reduce coupling losses. However, single-mode 1550 nm fiber with a tapered end was not available at the time the experiments were performed.

Fresnel losses can be reduced through use of an index matching gel. However, no such index matching gel is available to interface glass fibers ($n \approx 1.5$) to Si waveguide ($n \approx 3.5$).

Polishing the coupling ends of the waveguides could reduce the scattering loss. However, the diced substrates were only 5 mm X 5 mm. It is very difficult to polish such small substrates, as it is difficult to hold the sample during polishing. A possible solution

to the rough waveguide end might be to dice the wafers from the bottom part way through and 'cleave' the remainder of the way through. Another possible solution would be to make longer waveguides so that the chips are easier to cleave and polish.

6. Conclusions

The main goal of this thesis was the development of processes for the fabrication of passive sampled grating filters on SOI substrates. Filter devices capable of filtering multiple wavelengths are important elements for DWDM networks. Also, SOI substrates are very promising for future optoelectronic integrated circuits. The other main theme investigated was the possibility of embedding gratings in the sides of a rib waveguide. This approach has the advantage that non-uniformity in grating strength, pitch and phase can be realized in a single-etch fabrication process.

The waveguide parameters, especially rib width, for the existence of single-mode condition for two different SOI substrates were found using the effective index method. It was found that an index modulation as high as 0.01 is obtained for the gratings realized by modulating the rib widths. A numerical study of the spectral characteristics for these gratings was conducted for various parameters such as number of grating sections, spacing between grating sections and different index modulations. According to simulation results, the reflectivity (strength) of gratings is proportional to the number of grating sections and the index modulation. Also, the width of the stopbands is dependent on the spacing between the grating sections. Wider stopbands are obtained for smaller spacing lengths between grating sections. Thus, it was found that the spectral characteristics could be tuned to filter desired wavelengths by changing these parameters. To reduce the amount of 'noise' in the spectral response, two different methods of apodization were implemented in the simulations. From the simulation results, it was found that apodization helped a great deal in reducing the 'noise' level. However, this reduction in 'noise' was accompanied by a reduction in the peak reflectivity for different wavelengths. Thus, it was observed that there is a tradeoff between the peak reflectivity and the 'noise' level in the spectral response of these gratings.

Furthermore, simulations were done to study the effects of fabrication errors in the grating periods and the spacing between the grating sections. The simulation results

showed that the performance of the gratings was highly dependent on the fabrication errors and tight control was required to achieve the desired spectral response.

Various processing steps involved with the fabrication of gratings on SOI rib waveguides were investigated; optical lithography, e-beam lithography, liftoff and RIE. It was found that each of these steps is critical for the successful fabrication of gratings. An alignment technique was proposed to maintain angular alignment between the gratings written by e-beam lithography and waveguides patterned by optical lithography. It was observed that an optimal dose, proper focus, and optimal e-beam resist thickness was required for high accuracy of the gratings patterned by e-beam lithography. Different etch masks were investigated and it was found that for shallow rib waveguides, the choice of etch mask did not make much of a difference. It was also found that evaporation of etch masking metals resulted in better liftoff results than sputtering. Various etching recipes for the RIE were studied and it was observed that etch periods have to be controlled to avoid isotropic etching of sidewalls. A method to reduce the sidewall roughness by steam oxidation at high temperatures was investigated. Initial studies showed encouraging results. Because of the vibrations observed with e-beam lithography system due to the move of the e-beam facility after our mask fabrication, a final sampled grating filter could not be fabricated.

Experimentally, rib waveguides with different waveguide lengths were fabricated on SOI substrates using optimized values of etching, and were subsequently characterized by coupling light from a 1550 nm wavelength laser. A high amount of loss was observed and the reasons were attributed to coupling, reflection and scattering losses. Because of the non-availability of tapered single-mode 1550 nm fibers, and due to difficulty in polishing the end faces of very small samples, the coupling loss and the scattering loss at the end faces could not be reduced. By measuring waveguides of two different lengths, it was determined that propagation losses were relatively negligible.

Our study of the various fabrication steps and processes for embedding gratings on the sides of SOI rib waveguides show that it is actually possible to realize such grating filter

devices. However, an e-beam lithography system free from vibrations and an interferometric stage [96] to accurately pattern grating structures are required.

6.1 Future Work

The first appropriate step towards the continuation of this thesis would be to integrate the two lithography steps and fabricate and characterize a final grating filter on SOI substrates. This would provide a greater insight into the feasibility of fabricating such grating filters and the accuracy of our proposed alignment technique.

A better modeling of the gratings by incorporating a more rigorous approach (vector model) could predict the grating characteristics with much higher accuracy.
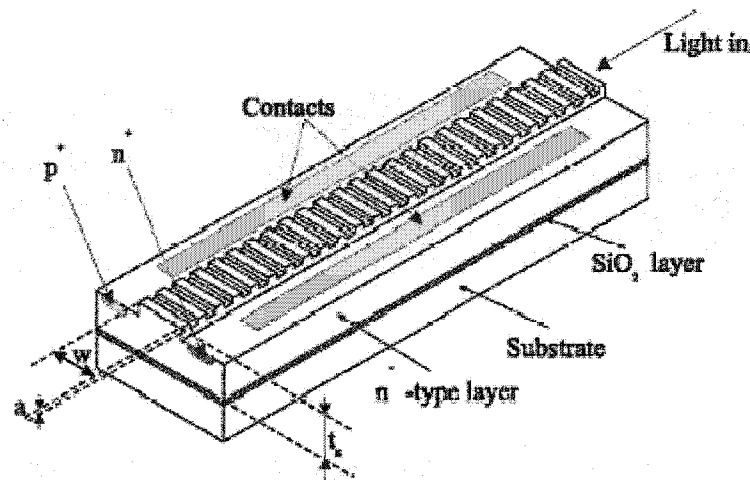
Figure 6.1: Structure of a rib waveguide Bragg grating with carrier injection arrangements (Source: [97])

Further, this passive grating filter device could be made into an active tunable filter by using the thermo-optic effect or carrier injection in Si (see Figure 6.1). Thermo-optic coefficient of silicon is $\sim 1.8 \times 10^{-4}$ K^{-1} (see Table 2.2), which is promising enough for tuning integrated circuits, mainly due to the small size of the integrated circuits. The response time in thermo-optic control is in the order of ms, which should be fast enough

for many applications identified for tunable filters in future optical networks. A schematic of a rib waveguide Bragg grating with carrier injection arrangement is shown in Figure 6.1 [97]. Such active tunable filters can greatly improve the flexibility of the grating device for filtering different wavelengths, and also allow relaxed fabrication tolerances.

References

1. F. M. Mims III. "Alexander Graham Bell and the Photophone: The Centennial of the Invention of Light-Wave Communications, 1880-1980." *Opt. News* 6, no. 1, pp 8-16, 1980

2. G. P. Agarwal, <u>Fiber-Optic Communication systems</u>, Wiley Series, 1997

3. K. O. Hill, Y. Fujii, D.C. Johnson, and B. S. Kawasaki, "Photosensitivity in optical fiber waveguides: Application to reflection filter fabrication", *Appl. Phys. Lett.*, vol. 32, pp. 647-649, 1978

4. B. S. Kawasaki, K. O. Hill, D. C. Johnson, and Y. Fujii, "Narrow-band Bragg reflectors in optical fibers", *Opt. Lett.*, vol. 3, pp. 66-68, 1978

5. D. K. W. Lam and B. K. Garside, "Characterization of single-mode optical fiber filters", *Appl. Opt.*, vol. 20, pp. 440-445, 1981

6. G. Meltz, W. W. Morey and W. H. Glenn, "Formation of Bragg gratings in optical fibers by a transverse holographic method", *Opt. Lett.*, vol. 14, pp. 823-825, 1989

7. I. Bennion, J. A. R. Williams, L. Zhang, S. K. and N. J. Doran, "Tutorial Review, UV - written in-fiber Bragg gratings", *Optic. Quantum Electron.*, vol. 28, pp.93-135, 1996

8. B. Poumellec, P. Nijay, D. M., and J. F. Bayon, "The UV-induced refractive index grating in $Fe:SiO_2$ performs: Additional CW experiments and the macroscopic origin of the change in index", *J. Phys. D. Appl. Phys.*, vol. 29, pp. 1842-1856, 1996

9. D. L. Lee, "Electromagnetic Principles of Integrated Optics", New York: John Wiley & Sons, Inc., 1986

10. R. G. Hunsperger, Integrated Optics: Theory and Technology, Springer series in Optical Sciences, 1984

11. R. G. DeCorby, "EE682 notes", Department of Electrical Engineering, University of Alberta, Canada, Winter 2002.

12. U. Fischer, B. Schuppert, K. Petermann, "Optical Wave-Guide Switches In Silicon-Based On Ge-Indiffused Wave-Guides," IEEE Photon. Tech. Lett., vol. 6 (8): 978-980 Aug 1994

13. P. K. Wei, W. S. Wang, "Fabrication Of Lithium-Niobate Optical Channel Wave-Guides By Nickel Indiffusion," Microwave And Optical Technology Letters, vol. 7 (5): 219-221 Apr 5 1994

14. N. A. F. Jaeger, L. Young, "Voltage-Induced Optical Wave-Guide Modulator In Lithium-Niobate," IEEE Journal Of Quantum Electronics, vol. 25 (4): 720-728 Apr 1989

15. R. A. Soref, J. Schmidtchen, and K. Petermann, "Large Single-Mode Rib waveguides in GeSi-Si and Si-on-SiO$_2$", J. Quant. Electronics, vol.27, n.8, 1991

16. R. Symms, "Optical Guided Waves and devices," McGraw-Hill, New York, 1992.

17. M. K. Smit, "Challenges and opportunities for photonic integration", Proceedings of the 1999 Pacific Rim Conference on Lasers and Electro-optics, Seoul, Korea, vol. 4., 1999

18. E. McGoldrick, S. D. Hubbard, G. Maxwell, N. Thomas, "passive optical silica-on-silicon waveguide components," Integrated Optics and Optoelectronics II, San Jose, CA, USA, vol. 1374, pp. 118-125

19. T. Shimizu, S. Nakamura, K. Ueki, I. Ohyama, "Silica-based waveguide devices", Furukawa-Review, n.11 Sep 1992, pp. 50-54

20. C. J. Sun, K. M. Schmidt, "Building passive components with silica waveguides," Proceedings of the 1999 Terahertz and Gigahertz Photonics, Denver, CO, USA, vol. 3795, 1999, pp. 313-319

21. A. Kilian, J. Kirchhof, B. Kuhlow, G. Przyrembel, and W. Wischmann, "Birefringence free planar optical waveguide made by flame hydrolysis deposition (FHD) through tailoring of the overcladding," J. Lightwave Technology, vol.18, 2000, pp.193

22. E. Wildermuth, C. Nadler, M. Lanker, W. Hunziker, and H. Melchior, "penalty-free polarization compensation of SiO2/Si arrayed waveguide grating wavelength multiplexers using stress release grooves."Electronics, Letters vol.34, 1998, pp.1661

23. K. S. Chiang and W. P. Wong, "Rib waveguides with degenerate polarized modes," Electronic letters, vol.32, 1996, pp.1098

24. W. P. Wong and K. S. Chiang, "Design of Optical strip-loaded waveguides with zero modal birefringence." J. Lightwave Technol. vol.16, 1998, pp.1240

25. K. Worhoff, B. J. Offrein, P. V. Lambeck, G. L. Bona, and A. Driessen, "Birefringence compensation applying double-core waveguiding structures," IEEE Photonics technol. Letters, vol.11, 1999, pp.206

26. Y. Inoue, H. Takahashi, S. Ando, T. Sawada, A. Himeno and M. Kawachi, "Elimination of polarization sensitivity in silica-based wavelength division multiplexer using a polyimide half-wave plate," J. Lightwave Technol. vol.15, 1997, pp. 1947

27. R. Satre and A. Costela, "Polymeric solid-state dye lasers", Adv. Mater. 7, 198 (1995)

28. L. Eldada, R. Norwood, R. Blomquist, L. W. Shacklette and M. McFarland, "Thermo-optically active polymeric photonic componnets," proc. Optical fiber communication conference, P124 (2000)

29. L. Eldada, K. Beeson, D. Pant, R. Blomquist, L. W. Shacklette and M. McFarland, "Polymeric components for all-optical networks," Proc. SPIE, 3950, 2000, pp.78

30. L. Eldada, K. Beeson, D. Pant, R. Blomquist, L. W. Shacklette and M. McFarland, "Thermo-optically active planar polymeric components for telecommunications applications," Porc. SPIE 3939, 2000, pp.69

31. L. Eldada, S. Yin, C. Poga, C. Glass, R. Blomquist and R. A. Norwood, "Integrated multi-channel OADMs using polymer Bragg grating MZIs," IEEE Photonics Technol. Lett. vol.10, 1998, pp.1416

32. L. Eldada, R. Blomquist, M. maxfield, D. Pant, G. Boudoughian, C. Poga, and R. A. Norwood, "Thermo-optic planar polymer Bragg grating in OADMs with broad tuning range," IEEE Photonics technol. Lett. vol.11, 1999, pp. 448

33. L. Eldada, "Polymer-based filters for DWDM applications," OSA TOPS WDM Components vol. 29, 1999, pp.105

34. J. F. Viens, C. L. Callender, J. P. Noad, and L. Eldada, "Compact wide-band polymer wavelength-division multiplexer," IEEE Photonics Technol. Lett., vol. 12, 2000, pp.1010

35. K. Worhoff, P. V. Lambeck, and A. Driessen, "Design, tolerenec analysis, and fabrication of SiON based planar optical waveguides for communication devices," J. Lightwave Technol. vol. 17, 1999, pp.1401

36. B. J. Offrein, R. Germann, F. Horst, H. W. M. Salemink, R. Beyeler, and G. L. Bona, "Resonant coupler-based tunable add-after-drop filter in silicon oxynitride technology for WDM networks," IEEE J. Sel. Top. Quantum Electron. 5, 1999, pp.1400

37. D. Wiesmann, C. David, R. germann, D. Erni, and G. L. Bona, "Apodized surface-corrugated gratings with varying duty cycles," IEEE Photonics Technol. Lett. vol. 12, 2000, pp. 639

38. E. Fluck, F. Horst, B. J. Offrein, R. germann, H. W. M. Salemink, and G. L. Bona, "Compact versatile thermooptical space switch based on beam steering by a waveguide array," IEEE Photonics Technol. Lett. vol. 11, 1999, pp.1399

39. B. J. Offrein, F. Horst, G. L. Bona, R. Germann, H. W. M. Salemeink, and R. Beyeler, "Adaptive gain equalizer in high-index-contrast SION technology," IEEE Photonics Technol. Lett. vol.12, pp.504, 2000

40. R. Alferness, "Titanium-diffused lithium niobate waveguide devices," Guided wave optoelectronics, 2nd ed., pp 145

41. T. Tamir, Ed., Springer-verlag, New York 1990, T. J. Wang, and W. S. Wang, "Wide-angle Ni-indiffused LiNbO$_3$ abrupt waveguide bend with a proton exchanged microprism," IEEE J. Sel. Top. Quantum Electron, vol. 6, pp. 132, 2000

42. M. Zirngibl, C. H. Joyner, and P. C. Chou, "Polarization compensated waveguide grating router on InP," Electron. Lett. vol. 31, pp. 1662, 1995

43. C. R. Doerr, C. H. Joyner, L. W. Stultz, and R. Monnard, "Wavelength-division multiplexing cross connect in InP," IEEE Photonics Technol. Lett. vol.10, pp. 117, 1998

44. K. Nakatsuhara, T. Mizumoto, S. Hossain, S. H. Jeong, Y. Tsukishima, B. J. Ma, and Y. Nakano, "GaInAsP-InP distributed feedback waveguides for all-optical switching," IEEE J. Sel. Top. Quantum Electron., vol. 6, pp. 143, 2000

45. L. Eldada, N. Zhu, M. N. Ruberto, M. Levy, R. Scarmozzino, and R. M. Osgood, Jr., "Rapid direct fabrication of active electro-optic modulators in GaAs," J. Lightwave Technol. vol. 12, pp. 1588, 1994

46. M. Levy, L. Eldada, R. Scarmozzino, R. M. Odgood, Jr., P. S. D. Lin, and F. Tong, "Fabrication of narrow-band channel-dropping filters," IEEE Photonics Technol. Lett. vol. 4, pp. 1378, 1998

47. M. Cada, and J. He, "Fast, all-optical bistable swtich made in GaAs/AlAs," Laser Focus World 2, 1994

48. J. P. Colinge, "Silicon -On-Insulator Technology: Materials to VLSI. Boston, MA: Kluwer Academic, 1991

49. L. Peters, "SOI takes over where silicon leaves off", Semiconductor Int., vol 16, pp 48-51, 1993

50. U. Fischer, T. Zinke, J. R. Kropp, F. Arndt, and K. Peterman, "0.1 db/cm waveguide losses in single-mode SOI rib waveguides," IEEE Photon. Trechnol. Lett., vol. 8, pp. 647-648, May 1996

51. P. D. Trinh, S. Yegnanarayanan, F. Coppinger, and B. Jalali, "Silicon-On-Insulator (SOI) phase-array wavelength multi/demultiplexer with extremely low polarization sensitivity," IEEE Photo. Technol. Lett., vol. 9, pp. 940-942, July 1997

52. G. V. Treyz, "Silicon mach-zhender waveguide interferometers operating at $1.3\mu m$," Electron. Lett., vol. 27, pp 118-120, Jan 17, 1991

53. P. D. Trinh, S. Yegnanarayanan, and B. Jalali, "Integrated optical directional couples in silicon-on-insulator," Electron. Lett., vol. 31, pp. 2097-2098, Nov. 23, 1995

54. H. H. Hosack, T.W. Houston, G.P. Pollack, "SIMOX Silicon-On-Insulator – Materials and Devices," Solid State Technology, (33 (12): 61-66, 1990

55. H. Baumgart, T. J. Letavic, R. Egloff, "Evaluation of wafer bonding and etch back for SOI technology," Philiphs Journal of Research, 49 (1-2): 91-124, 1995

56. M. Bruel, "A new silicon-on-insulator material technology," Electron. Lett., vol. 31, no 14, pp. 1201-1202, 1995

57. B. Jalali, S. Yegnanarayan, T. Yoon, T. Yoshimoto, I. Rendina, and F. Coppoinger, "Advances in Silicon-On-Insulator Optoelectroics," IEEE J. of Quant. Elec., vol. 4, mo. 6, 1998, pp. 93-947

58. AccuCorp Technical Services Inc.(http://www.accucorpts.com/index2.htm)

59. L. Eldada, "Advances in telecom and datacom optical components," Opt. Eng., vol. 40 (7) pp. 1165-1178, 2001

60. B. S. Kawasaki, K. O. Hill, D. C. Johnson, and Y. Fujii, "Narrow-band Bragg reflectors in optical fibes," Opt. Lett., vol. 3, pp. 66-68, 1978

61. G. Meltz, W. W. Morey, and W. H. Glenn, "Formation of Bragg gratings in optical fibers by a transverse holographic method," Opt. Lett., vol. 14, pp. 832-825, 1989

62. P. J. Lemaire, R. M. Atkins, V. Mizrahi, and W. A. Reed,"High pressure H_2 loading as a technique for achieving ultrahigh UV photosensitivity and thermal sensitivity in GeO_2 doped optical fibers," Electron. Lett., vol. 29, pp. 1191-1193, 1993

63. F. Bilodeau, B. Malo, J. Albert, D. C. Johnson, K. O. Hill, Y. Hibino, M. Abe, and M. Kawachi, "Photosensitization of optical fiber and silica-on-silicon/silica waveguides," Opt. Lett., vol. 18, pp. 953-955, 1993

64. A. Othonos, X. Lee, "Novel and improved methods of writing Bragg gratings using phase masks," IEEE Photonics Tech. Lett., 7(10: 1183-1185, 1995

65. Z. Xiong, G. D. Peng, B. Wu, and P. L. Chu, "Effects of the Zeroth-Order Diffraction of a Phase Mask on Bragg Gratings," Journal of Lightwave Technology, vol. 17, no. 11, 1999

66. J. Ferrera, J. N. Damask, V.V. Wong, H. I. Smith, H. A. Haus, "High-coherence QWS gratings for optoelectronic devices: why spatial-phase-locked e-beam lithography is necessary", *Optical Fiber Communication Technical Digest* 4, pp.139-141, 1994

67. S. P. Pogossian, L. Vescan, and A. Vonsovici, "The single-mode condition for semiconductor rib waveguides with large cross section," J. Light. Technol. vol.16, n.10, 1998

68. Soitec Inc., http://www.soitec.com/

69. Analog Devices Inc., http://www.analog.com/

70. G. B. Hocker and W. K. Burns, Applied Optics vol. 16, pp. 113, 1977

71. C. R. Pollock, "Fundamentals of optoelectronics," Irwin publications Inc., 1995

72. S. P. Pogossian, H. L. Gall, J. Gieraltowski, and J. Loaec, "Determination of the parameters of rectangular waveguides by new effective index methods," J. Modern Opt., vol. 42, no. 5, pp. 403-409, 1995

73. A. Kumar, D. F. Clark, and B. Culshaw, "Explanation of errors inherent in the effective index method for analyzing rectangular-core waveguides," Opt. Lett., vol. 13, no. 12, pp. 1129-1131, 1988

74. N. G. R. Broderick, and C. Martin de Sterke, "Theory of grating superstructures," The Am. Phy. Soc., vol. 55, n. 3, 1997

75. B. J. Eggleton, P. A. Krug, L. Poladian and F. Ouellette, "Long periodic superstructure Bragg gratings in optical fibers," Electron. Lett., vol. 30, n. 19, 1994

76. V. Jayaraman, Z-M. Chuang, and L. A. Coldren, "Theory, design, and performance of extended tuning range semiconductor lasers with sampled gratings," J. Quant. Elec., vol. 29, n. 6, 1993

77. D. Marcuse, "Coupled-mode theory for anisotropic optical-waveguides," Bell System Technical Journal, 54(6): 985-995, 1975

78. G. Coppola, A. Irace, A. Cutolo, and M. Iodice, "Effect of fabrication errors in channel waveguide Bragg gratings," App. Optics, vol. 38, n. 9, 1999

79. M. A. Muriel, A. Carballar, and J. Azana, "Field distributions inside fiber gratings," J. Quant. Elec., vol. 35, n. 4, 1999

80. R. G. DeCorby, Department of Electrical Engineering, University of Alberta, Canada

81. M. Matsuhara and K. O. Hill, "Optical-Waveguide Band-Rejection Filters: Design," App. Optics, vol. 13, n. 12, 1974

82. C. F. Lam, R. B. Vrijen, P. P. L. Chang-Chien, D. F. Sievenpiper, and E. Yablonovitch, "A tunable wavelength demultiplexer using logrithmic filter chanins," J. Light. Technol., vol. 16, n. 9, 1998

83. M. H. Lim, T. E. Murphy, J. Ferrera, J. N. Damask, and H. I. Smith, "Fabrication techniques for grating-based optical devices," J. Vac. Sci. Technol. B vol. 17 (6), 1999, pp. 3208-3211

84. T. Aalto, S. Yliniemi, P. Heimala, and P. Pekko, "Integrated Bragg gratings in silicon-on-insulator waveguides," Proceedings of SPIE, Photonics West 2002, San Jose, California

85. R. Steingruber, and M. Hamacher, "Simultaneous exposure of filter gratings and waveguides by direct write electron-beam lithography," Microelectronic engineering vol. 35, 1997, pp. 341-344

86. R. C. Tiberio, D. W. Carr, M. J. Rooks, S. J. Mihailov, F. Bilodeau, J. Albert, D. Stryckman, D. C. Johnson, K. O. Hill, A. W. McClelland, and B. J. Hughes, "Fabrication of electron beam generated, chirped, phase mask (1070.11 - 1070.66 nm) for fiber Bragg grating dispersion compensator," J. Vac. Sci. Technol. B vol. 16 (6), 1998, pp. 3237-3240

87. C. Rogers, D. Goodchild, R. Baulcomb, M. Butler, P. Hoyle, S. Konellopoulos, S. Clements, and B. Pugh, "High perfection chirped grating phase masks by electron-beam definition," J. Vac. Sci. Technol. B vol. 17 (6), 1999, pp. 3217-3221

88. M. Naydenkov and B. Jalali, "Fabrication of high aspect ratio photonic bandgap structures on Silicon-on-insulator," Integrated optics devics IV, San Jose, CA, USA, vol. 3936, 2000, pp. 33-39

89. M. J. Madou, "Fundamentals of Microfabrication," CRC Press LLC, 2002

90. M. Solomonos, University of Alberta

91. M. Brett, "EE 642 notes", University of Alberta, Edmonton, Canada, January 2001

92. Y. Y. Tsui, Department of Electrical Engineering, University of Alberta, Edmonton, Canada

93. E. A. Taft, "Steam oxidation of Silicon," J. Electrochemical Society, 136 (11): 3476-3478, 1989

94. Internet source: http://www.tpub.com/neets/tm/108-2.htm

95. Internet source: http://www.its.bldrdoc.gov/fs-1037/dir-016/_2397.htm

96. D. Nyyssonen, M. T. Postek, "SEM-based system for calibration of linewidth SRMS for the IC industry", Proceedings of SPIE v 565, Bellingham, WA, USA p 180-186, 1985

97. G. Coppola, A. Irace, M. Iodice and A. Cutolo, "Simulation and analysis of a high-efficiency silicon optoelectronic modulator based on a Bragg mirror", Optical Engineering, vol. 40(6), June 2001, pp. 1076-1081

Appendix – I

```
% This is an m-file that calls rib4, and plots the
effective index of a rib waveguide as a function of the rib
width.   The geometrical   constraints for single-mode
propagation are used.
%
% Parameters
%
% Hrib=height of the core in the rib region
% hrib=height of the core outside the rib region
% rrib=hrib/Hrib;
% wrib=width of rib
% trib=wrib/Hrib;
%
clear NeffV
rribV=0.6:0.05:0.9;
QR=length(rribV);
for qr=1:QR
    rrib=rribV(qr);
    hrib=Hrib*rrib;
    wribmax=Hrib*rrib/sqrt(1-rrib^2);
    wribV=0.5e-6:0.5e-7:wribmax;
    wribVm=wribV*1e6;
    QW=length(wribV);
    for qw=1:QW
        w=wribV(qw);
        h=hrib;
        rib4;
        NeffV(qw)=Neff;
    end
    plot(wribVm,NeffV)
    grid
    hold on
end
```

The matlab file rib4 called by this program is attached in the following pages.

rib4.m

```
% this m-file codes the effective index method for
analyzing a rib waveguide.
% the guide is assumed to be single-mode, so that only the
fundamental mode is solved. The guide is assumed to have
same material for upper and lower cladding
% the outputs are the effective modal index, the
approximate field patterns, the approximate confinement
factor for the mode.
%
% w=the width of the rib
% H=height of the rib in the core section
% h=height of the core material outside the rib
% ncore=refractive index of the core material
% nclad=refractive index of the cladding
% lambda=wavelength
%
lambda=1.55e-6;
ncore=3.5;
nclad=1.5;
H=1.5e-6;


k0=2*pi/lambda;
%
% calculate the maximum value of transverse wave vector in
core, based on total
% internal reflection
kapmax=sqrt(k0^2*(ncore^2-nclad^2));
%
% calculate starting guesses for transverse propagtion
vectors, based on
% the one-half-wavelength between reflecting boundaries
condition
kaprib0=pi/(2*H);
kapout0=pi/(2*h);
if kaprib0>kapmax
kaprib0=kapmax;
end
if kapout0>kapmax
kapout0=kapmax;
end
%
% solve numerically for the propagation vectors of
fundamental modes
```

```
%
kaprib=fminsearch('eigensymm',kaprib0,[],H,k0,ncore,nclad);
betarib=sqrt(k0^2*ncore^2-kaprib^2);
gammrib=sqrt(k0^2*(ncore^2-nclad^2)-kaprib^2);
Neffrib=betarib/k0;
%
kapout=fminsearch('eigensymm',kapout0,[],h,k0,ncore,nclad);
betaout=sqrt(k0^2*ncore^2-kapout^2);
gammout=sqrt(k0^2*(ncore^2-nclad^2)-kapout^2);
Neffout=betaout/k0;
%
% use the effective indices to analyze transverse
waveguiding properties
%
kaptran0=pi/(2*w);
%
kaptran=fminsearch('eigensymmTM',kaptran0,[],w,k0,Neffrib,N
effout);
betatran=sqrt(k0^2*Neffrib^2-kaptran^2);
gammtran=sqrt(k0^2*(Neffrib^2-Neffout^2)-kaptran^2);
Neff=betatran/k0;

function y=eigensymm(kap,h,k0,ncore,nclad)
y=abs(tan(kap*h/2)-(1/kap)*sqrt(k0^2*(ncore^2-nclad^2)-
kap^2));

function y=eigensymmTM(kap,h,k0,Neffrib,Neffout)
y=abs(tan(kap*h/2)-
(Neffrib/Neffout)^2*(1/kap)*sqrt(k0^2*(Neffrib^2-
Neffout^2)-kap^2));
```

Appendix – II

```
% This is an m-file that calculates the reflection and
transmission coefficients
% of a one-dimensional waveguide grating structure.  It can
be used to describe the
% propagation in a fibre or waveguide bragg grating
assuming that the guide is
% single-moded, and that the index profile reflects the
effective index for the
% propagating mode.
% THIS FILE is for cascaded, but non-phase-shifted
gratings.
% The number of sections is accepted
% as an input to the simulation, as is the number of
periods in each section.
% FOR MAXIMUM Generality, grating period and index
modulation in each section are
% also accepted as inputs to the simulation.
% THIS FILE ASSUMES A SQARE GRATING PROFILE, to shorten
simulation times.
% THIS FILE calculates field distributions.
% THIS FILE does NOT include absorption.
% THIS FILE calculates group delay.
%
%
% INPUT PARAMETERS provided to the simulation.
%
% n0=the effective modal index in the input region, to the
left of the grating.
n0=3.4598;
% nL=the effecitve modal index in the output region, right
of the grating.
nL=3.4598;
% mgrat=the number of constant phase grating sections.
mgrat=5;
% ngrat=a vector, with length mgrat, specifying the number
of periods in each
% grating section.
ngrat=[313 1200 313 1200 313];
% delgV=a vector describing the grating period in each
section
delgV=[224e-9 224e-9 224e-9 224e-9 224e-9];
% ng=base modal index in the grating region.
% dngV=vector for amplitude of the index modulation in each
grating section.
dngV=[0.01 0 0.01 0 0.01];
```

```
% kap=effective extinction coefficient
% lambda=input vector of free-space wavelengths
lambda=[1.548e-6:0.0001e-6:1.552e-6];
%
% initialize data space
clear k0
clear Z
clear nz
clear zn
clear mpdet
clear mp11
clear mp12
clear mp21
clear mp22
clear Eplus
clear Eminu
clear r
clear t
clear R
clear T
clear A
clear tphase
clear tgroup
clear Epmag
clear Emmag
clear Itot
%
% generate vector of free-space propagation constants
k0=2.*pi./lambda;
% generate vector of frequencies
frequency=3e8./lambda;
%
% generate vector of aggregate length after each grating
section
%
Ltot=sum(ngrat.*delgV);
Ltg(1)=ngrat(1)*delgV(1);
for q=2:mgrat
Ltg(q)=Ltg(q-1)+ngrat(q)*delgV(q);
end
%
%
% generate vector of indices based on input index function
%
zn(1)=ngrat(1)*2;
for q=2:mgrat
zn(q)=ngrat(q)*2+zn(q-1);
```

```
end
%
% generate vector of coordinates
Z(1:zn(1))=0:delgV(1)/2:Ltg(1)-delgV(1)/2;
delzV(1:zn(1))=delgV(1)/2;
for q=2:mgrat
Z(zn(q-1)+1:zn(q))=Ltg(q-1):delgV(q)/2:Ltg(q)-delgV(q)/2;
delzV(zn(q-1)+1:zn(q))=delgV(q)/2;
end
%
ZL=length(Z);
ZQ=1:1:ZL;
%
% THIS FILE assumes a square grating profile.
ngb=n0;
nz(1:zn(1))=ngb-(dngV(1)/2).*(-1).^ZQ(1:zn(1));
for q=2:mgrat
nz(zn(q-1)+1:zn(q))=ngb-(dngV(q)/2).*(-1).^ZQ(zn(q-
1)+1:zn(q));
end
Nz=nz;
%
% create for-loop to run simulation at each point in vector
of wavelengths
Q=length(k0);
tstart=clock;
for q=1:Q
%
% calculate transfer matrix for the last layer and
interface
QZ=length(Z);
%
mgrating=[exp(i*k0(q)*Nz(QZ)*delzV(QZ)) 0; 0 exp(-
i*k0(q)*Nz(QZ)*delzV(QZ))]*(1/(2*Nz(QZ)))*[Nz(QZ)+nL
Nz(QZ)-nL; Nz(QZ)-nL Nz(QZ)+nL];
%
%mp11s(QZ)=mgratings(1,1);
%mp21s(QZ)=mgratings(2,1);
%
% calculate transfer matrix for grating structure
%
for qz=QZ-1:-1:2
mgrating=[exp(i*k0(q)*Nz(qz)*delzV(qz)) 0; 0 exp(-
i*k0(q)*Nz(qz)*delzV(qz))]*(1/(2*Nz(qz)))*[Nz(qz)+Nz(qz+1)
Nz(qz)-Nz(qz+1); Nz(qz)-Nz(qz+1) Nz(qz)+Nz(qz+1)]*mgrating;
%mp11s(qz)=mgratings(1,1);
%mp21s(qz)=mgratings(2,1);
```

```
end
%
% calculate transfer matrix for the first interface and
layer and interface
%
mgrating=(1/(2*n0))*[n0+Nz(1) n0-Nz(1); n0-Nz(1)
n0+Nz(1)]*[exp(i*k0(q)*Nz(1)*delzV(1)) 0; 0 exp(-
i*k0(q)*Nz(1)*delzV(1))]*(1/(2*Nz(1)))*[Nz(1)+Nz(2) Nz(1)-
Nz(2); Nz(1)-Nz(2) Nz(1)+Nz(2)]*mgrating;
%mp11s(1)=mgratings(1,1);
%mp21s(1)=mgratings(2,1);
%
% CALCULATE SIGNAL FIELD from transfer matrices
%for qq=1:QZ
%Epluss(qq)=(mp11s(qq)/mgratings(1,1))*Esin;
%Emins(qq)=(mp21s(qq)/mgratings(1,1))*Esin;
%Etots(qq)=Epluss(qq)+Emins(qq);
%Isig(qq)=0.5*3E8*8.85E-
12*nz(qq)*(abs(Epluss(qq))^2+abs(Emins(qq))^2);
%Sflux(qq)=Isig(qq)*sw/(6.626E-34*3E8);
%end
%
% calculate the field amplitudes as a function of position
%
%for qq=1:QZ
%Eplus(q,qq)=(1/mpdet(qq))*(mp22(qq)-
mp12(qq)*mgrating(2,1)/mgrating(1,1));
%Eminu(q,qq)=(1/mpdet(qq))*(-
mp21(qq)+mp11(qq)*mgrating(2,1)/mgrating(1,1));
%end
%Emmag=abs(Eminu);
%Epmag=abs(Eplus);
%Itot=Emmag.^2+Epmag.^2;
%
% calculate the overall amplitude reflection and
transmission coefficients
%
r(q)=mgrating(2,1)/mgrating(1,1);
t(q)=1/mgrating(1,1);
%
% calculate the power reflectivity and transmissivity
%
R(q)=r(q)*conj(r(q));
T(q)=t(q)*conj(t(q));
%
% calculate phase of transmitted wave at output plane
%
```

```
tphase(q)=atan(imag(t(q))/real(t(q)));
if real(t(q))<0
tphase(q)=tphase(q)+pi;
end
if real(t(q))>0
if imag(t(q))<0
tphase(q)=tphase(q)+2*pi;
end
end
%
percentdone=(q/Q)*100
timetonow=etime(clock,tstart)
end
%
% calculate group delay in transmission
%
tgroupNG=Ltot*n0/3e8;
tgroup(1)=-(1/(2*pi))*(tphase(2)-tphase(1))/(frequency(2)-
frequency(1));
if tgroup(1)<0
tgroup(1)=-(1/(2*pi))*(tphase(2)+(2*pi-
tphase(1)))/(frequency(2)-frequency(1));
end
DF(1)=tgroup(1)/tgroupNG;
for q=2:Q
tgroup(q)=-(1/(2*pi))*(tphase(q)-tphase(q-
1))/(frequency(q)-frequency(q-1));
if tgroup(q)<0
tgroup(q)=-(1/(2*pi))*(tphase(q)+(2*pi-tphase(q-
1)))/(frequency(q)-frequency(q-1));
end
DF(q)=tgroup(q)/tgroupNG;
end
%
%subplot(2,1,1)
plot(lambda,R,'b-')
%subplot(2,1,2)
%plot(lambda,DF,'m-')
```

% This is an m-file that calculates the reflection and transmission coefficients
% of a one-dimensional waveguide grating structure. It can be used to describe the
% propagation in a fibre or waveguide bragg grating assuming that the guide is
% single-moded, and that the index profile reflects the effective index for the
% propagating mode.
% THIS FILE is for cascaded, but non-phase-shifted gratings.
% The number of sections is accepted
% as an input to the simulation, as is the number of periods in each section.
% FOR MAXIMUM Generality, grating period and index modulation in each section are
% also accepted as inputs to the simulation.
% THIS FILE ASSUMES A SQARE GRATING PROFILE, to shorten simulation times.
% THIS FILE calculates field distributions.
% THIS FILE does NOT include absorption.
% THIS FILE calculates group delay.
% THIS FILE calculates field at a single wavelength also.
% THIS FILE assumes an overall Gaussian apodization.
%
%
% INPUT PARAMETERS provided to the simulation.
%
% n0=the effective modal index in the input region, to the left of the grating.
n0=3.4598;
% nL=the effecitve modal index in the output region, right of the grating.
nL=3.4598;
% mgrat=the number of constant phase grating sections.
mgrat=9;
% ngrat=a vector, with length mgrat, specifying the number of periods in each
% grating section.
ngrat=[313 1200 313 1200 313 1200 313 1200 313];
% delgV=a vector describing the grating period in each section
delgV=[224e-9 224e-9 224e-9 224e-9 224e-9 224e-9 224e-9 224e-9 224e-9];
% ng=base modal index in the grating region.

```
% dngV=vector for amplitude of the index modulation in each
grating section.
dngV=[0.01 0 0.01 0 0.01 0 0.01 0 0.01];
% kap=effective extinction coefficient
% lambda=input vector of free-space wavelengths
lambda=[1.548e-6:0.0001e-6:1.552e-6];
Gv =1.0;
lambdaE=1.55e-6;
%
% initialize data space
clear k0
clear Z
clear nz
clear zn
clear mpdet
clear mp11
clear mp12
clear mp21
clear mp22
clear Eplus
clear Eminu
clear r
clear t
clear R
clear T
clear A
clear tphase
clear tgroup
clear Epmag
clear Emmag
clear Itot
%
% generate vector of free-space propagation constants
k0=2.*pi./lambda;
% generate vector of frequencies
frequency=3e8./lambda;
%
% generate vector of aggregate length after each grating
section
%
Ltot=sum(ngrat.*delgV);
Ltg(1)=ngrat(1)*delgV(1);
for q=2:mgrat
Ltg(q)=Ltg(q-1)+ngrat(q)*delgV(q);
end
%
%
```

```
% generate vector of indices based on input index function
%
zn(1)=ngrat(1)*2;
for q=2:mgrat
zn(q)=ngrat(q)*2+zn(q-1);
end
%
% generate vector of coordinates
Z(1:zn(1))=0:delgV(1)/2:Ltg(1)-delgV(1)/2;
delzV(1:zn(1))=delgV(1)/2;
for q=2:mgrat
Z(zn(q-1)+1:zn(q))=Ltg(q-1):delgV(q)/2:Ltg(q)-delgV(q)/2;
delzV(zn(q-1)+1:zn(q))=delgV(q)/2;
end
%
ZL=length(Z);
Zmax=Z(ZL);
Zmid=Zmax/2;
ZQ=1:1:ZL;
%
% THIS FILE assumes a square grating profile.
ngb=n0;
nz(1:zn(1))=ngb-exp(-Gv.*((Z(1:zn(1))-
Zmid)./Zmax).^2).*(dngV(1)/2).*(-1).^ZQ(1:zn(1));
for q=2:mgrat
nz(zn(q-1)+1:zn(q))=ngb-exp(-Gv.*((Z(zn(q-1)+1:zn(q))-
Zmid)./Zmax).^2).*(dngV(q)/2).*(-1).^ZQ(zn(q-1)+1:zn(q));
end
Nz=nz;
%
% create for-loop to run simulation at each point in vector
of wavelengths
Q=length(k0);
tstart=clock;
for q=1:Q
%
% calculate transfer matrix for the last layer and
interface
QZ=length(Z);
%
mgrating=[exp(i*k0(q)*Nz(QZ)*delzV(QZ)) 0; 0 exp(-
i*k0(q)*Nz(QZ)*delzV(QZ))]*(1/(2*Nz(QZ)))*[Nz(QZ)+nL
Nz(QZ)-nL; Nz(QZ)-nL Nz(QZ)+nL];
%
mp11(QZ)=mgrating(1,1);
mp21(QZ)=mgrating(2,1);
%
```

```
% calculate transfer matrix for grating structure
%
for qz=QZ-1:-1:2
mgrating=[exp(i*k0(q)*Nz(qz)*delzV(qz)) 0; 0 exp(-
i*k0(q)*Nz(qz)*delzV(qz))]*(1/(2*Nz(qz)))*[Nz(qz)+Nz(qz+1)
Nz(qz)-Nz(qz+1); Nz(qz)-Nz(qz+1) Nz(qz)+Nz(qz+1)]*mgrating;
mp11(qz)=mgrating(1,1);
mp21(qz)=mgrating(2,1);
end
%
% calculate transfer matrix for the first interface and
layer and interface
%
mgrating=(1/(2*n0))*[n0+Nz(1) n0-Nz(1); n0-Nz(1)
n0+Nz(1)]*[exp(i*k0(q)*Nz(1)*delzV(1)) 0; 0 exp(-
i*k0(q)*Nz(1)*delzV(1))]*(1/(2*Nz(1)))*[Nz(1)+Nz(2) Nz(1)-
Nz(2); Nz(1)-Nz(2) Nz(1)+Nz(2)]*mgrating;
mp11(1)=mgrating(1,1);
mp21(1)=mgrating(2,1);
%
% CALCULATE FIELD at desired wavelength from transfer
matrices
if lambda(q)-lambdaE<1e-15
for qq=1:QZ
Eplus(qq)=(mp11(qq)/mgrating(1,1));
Eminu(qq)=(mp21(qq)/mgrating(1,1));
%Etots(q,qq)=Epluss(qq)+Emins(qq);
Itot(qq)=(abs(Eplus(qq))^2+abs(Eminu(qq))^2);
%Sflux(qq)=Isig(qq)*sw/(6.626E-34*3E8);
end
end
%
% calculate the field amplitudes as a function of position
%
%for qq=1:QZ
%Eplus(q,qq)=(1/mpdet(qq))*(mp22(qq)-
mp12(qq)*mgrating(2,1)/mgrating(1,1));
%Eminu(q,qq)=(1/mpdet(qq))*(-
mp21(qq)+mp11(qq)*mgrating(2,1)/mgrating(1,1));
%end
%Emmag=abs(Eminu);
%Epmag=abs(Eplus);
%Itot=Emmag.^2+Epmag.^2;
%
% calculate the overall amplitude reflection and
transmission coefficients
%
```

```
r(q)=mgrating(2,1)/mgrating(1,1);
t(q)=1/mgrating(1,1);
%
% calculate the power reflectivity and transmissivity
%
R(q)=r(q)*conj(r(q));
T(q)=t(q)*conj(t(q));
%
% calculate phase of transmitted wave at output plane
%
tphase(q)=atan(imag(t(q))/real(t(q)));
if real(t(q))<0
tphase(q)=tphase(q)+pi;
end
if real(t(q))>0
if imag(t(q))<0
tphase(q)=tphase(q)+2*pi;
end
end
%
percentdone=(q/Q)*100
timetonow=etime(clock,tstart)
end
%
% calculate group delay in transmission
%
tgroupNG=Ltot*n0/3e8;
tgroup(1)=-(1/(2*pi))*(tphase(2)-tphase(1))/(frequency(2)-
frequency(1));
if tgroup(1)<0
tgroup(1)=-(1/(2*pi))*(tphase(2)+(2*pi-
tphase(1)))/(frequency(2)-frequency(1));
end
DF(1)=tgroup(1)/tgroupNG;
for q=2:Q
tgroup(q)=-(1/(2*pi))*(tphase(q)-tphase(q-
1))/(frequency(q)-frequency(q-1));
if tgroup(q)<0
tgroup(q)=-(1/(2*pi))*(tphase(q)+(2*pi-tphase(q-
1)))/(frequency(q)-frequency(q-1));
end
DF(q)=tgroup(q)/tgroupNG;
end
%
figure(1)
plot(lambda,R,'b-')
%figure(2)
```

```
%plot(lambda,DF,'m-')
figure(3)
plot(Z,Nz)
figure(4)
plot(Z,Itot)
```

Appendix – IV

```
% This is an m-file that calculates the reflection and
transmission coefficients
% of a one-dimensional waveguide grating structure.  It can
be used to describe the
% propagation in a fibre or waveguide bragg grating
assuming that the guide is
% single-moded, and that the index profile reflects the
effective index for the
% propagating mode.
% THIS FILE is for cascaded, but non-phase-shifted
gratings.
% The number of sections is accepted
% as an input to the simulation, as is the number of
periods in each section.
% FOR MAXIMUM Generality, grating period and index
modulation in each section are
% also accepted as inputs to the simulation.
% THIS FILE ASSUMES A SQARE GRATING PROFILE, to shorten
simulation times.
% THIS FILE calculates field distributions.
% THIS FILE does NOT include absorption.
% THIS FILE calculates group delay.
%
%
% INPUT PARAMETERS provided to the simulation.
%
% n0=the effective modal index in the input region, to the
left of the grating.
n0=3.4598;
% nL=the effecitve modal index in the output region, right
of the grating.
nL=3.4598;
% mgrat=the number of constant phase grating sections.
mgrat=5;
% ngrat=a vector, with length mgrat, specifying the number
of periods in each
% grating section.
ngrat=[313 1200 313 1200 313];
% delgV=a vector describing the grating period in each
section
delgV=[224e-9 224e-9 224e-9 224e-9 224e-9];
% ng=base modal index in the grating region.
% dngV=vector for amplitude of the index modulation in each
grating section.
dngV=[0.01 0 0.01 0 0.01];
```

```
% kap=effective extinction coefficient
% lambda=input vector of free-space wavelengths
lambda=[1.548e-6:0.00001e-6:1.552e-6];
variZ=[0.01e-6 0.01e-6 0.01e-6 0.01e-6 0.01e-6];
%
% initialize data space
clear k0
clear Z
clear nz
clear zn
clear mpdet
clear mp11
clear mp12
clear mp21
clear mp22
clear Eplus
clear Eminu
clear r
clear t
clear R
clear T
clear A
clear tphase
clear tgroup
clear Epmag
clear Emmag
clear Itot
%
% generate vector of free-space propagation constants
k0=2.*pi./lambda;
% generate vector of frequencies
frequency=3e8./lambda;
%
% generate vector of aggregate length after each grating
section
%
Ltot=sum(ngrat.*delgV);
Ltg(1)=ngrat(1)*delgV(1);
for q=2:mgrat
Ltg(q)=Ltg(q-1)+ngrat(q)*delgV(q);
end
%
%
% generate vector of indices based on input index function
%
zn(1)=ngrat(1)*2;
for q=2:mgrat
```

```
zn(q)=ngrat(q)*2+zn(q-1);
end
%
% generate vector of coordinates
Z(1:zn(1))=0:delgV(1)/2:Ltg(1)-delgV(1)/2;
delzV(1:zn(1))=delgV(1)/2;
for q=2:mgrat
Z(zn(q-1)+1:zn(q))=Ltg(q-1):delgV(q)/2:Ltg(q)-delgV(q)/2;
delzV(zn(q-1)+1:zn(q))=delgV(q)/2;
end
delzV(zn(2))=randn*variZ(2)+delgV(2)/2;
delzV(zn(4))=randn*variZ(4)+delgV(4)/2;
%
ZL=length(Z);
ZQ=1:1:ZL;
%
% THIS FILE assumes a square grating profile.
ngb=n0;
nz(1:zn(1))=ngb-(dngV(1)/2).*(-1).^ZQ(1:zn(1));
for q=2:mgrat
nz(zn(q-1)+1:zn(q))=ngb-(dngV(q)/2).*(-1).^ZQ(zn(q-
1)+1:zn(q));
end
Nz=nz;
%
% create for-loop to run simulation at each point in vector
of wavelengths
Q=length(k0);
tstart=clock;
for q=1:Q
%
% calculate transfer matrix for the last layer and
interface
QZ=length(Z);
%
mgrating=[exp(i*k0(q)*Nz(QZ)*delzV(QZ)) 0; 0 exp(-
i*k0(q)*Nz(QZ)*delzV(QZ))]*(1/(2*Nz(QZ)))*[Nz(QZ)+nL
Nz(QZ)-nL; Nz(QZ)-nL Nz(QZ)+nL];
%
%mp11s(QZ)=mgratings(1,1);
%mp21s(QZ)=mgratings(2,1);
%
% calculate transfer matrix for grating structure
%
for qz=QZ-1:-1:2
```

```
mgrating=[exp(i*k0(q)*Nz(qz)*delzV(qz)) 0; 0 exp(-
i*k0(q)*Nz(qz)*delzV(qz))]*(1/(2*Nz(qz)))*[Nz(qz)+Nz(qz+1)
Nz(qz)-Nz(qz+1); Nz(qz)-Nz(qz+1) Nz(qz)+Nz(qz+1)]*mgrating;
%mp11s(qz)=mgratings(1,1);
%mp21s(qz)=mgratings(2,1);
end
%
% calculate transfer matrix for the first interface and
layer and interface
%
mgrating=(1/(2*n0))*[n0+Nz(1) n0-Nz(1); n0-Nz(1)
n0+Nz(1)]*[exp(i*k0(q)*Nz(1)*delzV(1)) 0; 0 exp(-
i*k0(q)*Nz(1)*delzV(1))]*(1/(2*Nz(1)))*[Nz(1)+Nz(2) Nz(1)-
Nz(2); Nz(1)-Nz(2) Nz(1)+Nz(2)]*mgrating;
%mp11s(1)=mgratings(1,1);
%mp21s(1)=mgratings(2,1);
%
% CALCULATE SIGNAL FIELD from transfer matrices
%for qq=1:QZ
%Epluss(qq)=(mp11s(qq)/mgratings(1,1))*Esin;
%Emins(qq)=(mp21s(qq)/mgratings(1,1))*Esin;
%Etots(qq)=Epluss(qq)+Emins(qq);
%Isig(qq)=0.5*3E8*8.85E-
12*nz(qq)*(abs(Epluss(qq))^2+abs(Emins(qq))^2);
%Sflux(qq)=Isig(qq)*sw/(6.626E-34*3E8);
%end
%
% calculate the field amplitudes as a function of position
%
%for qq=1:QZ
%Eplus(q,qq)=(1/mpdet(qq))*(mp22(qq)-
mp12(qq)*mgrating(2,1)/mgrating(1,1));
%Eminu(q,qq)=(1/mpdet(qq))*(-
mp21(qq)+mp11(qq)*mgrating(2,1)/mgrating(1,1));
%end
%Emmag=abs(Eminu);
%Epmag=abs(Eplus);
%Itot=Emmag.^2+Epmag.^2;
%
% calculate the overall amplitude reflection and
transmission coefficients
%
r(q)=mgrating(2,1)/mgrating(1,1);
t(q)=1/mgrating(1,1);
%
% calculate the power reflectivity and transmissivity
%
```

```
R(q)=r(q)*conj(r(q));
T(q)=t(q)*conj(t(q));
%
% calculate phase of transmitted wave at output plane
%
tphase(q)=atan(imag(t(q))/real(t(q)));
if real(t(q))<0
tphase(q)=tphase(q)+pi;
end
if real(t(q))>0
if imag(t(q))<0
tphase(q)=tphase(q)+2*pi;
end
end
%
percentdone=(q/Q)*100
timetonow=etime(clock,tstart)
end
%
% calculate group delay in transmission
%
tgroupNG=Ltot*n0/3e8;
tgroup(1)=-(1/(2*pi))*(tphase(2)-tphase(1))/(frequency(2)-
frequency(1));
if tgroup(1)<0
tgroup(1)=-(1/(2*pi))*(tphase(2)+(2*pi-
tphase(1)))/(frequency(2)-frequency(1));
end
DF(1)=tgroup(1)/tgroupNG;
for q=2:Q
tgroup(q)=-(1/(2*pi))*(tphase(q)-tphase(q-
1))/(frequency(q)-frequency(q-1));
if tgroup(q)<0
tgroup(q)=-(1/(2*pi))*(tphase(q)+(2*pi-tphase(q-
1)))/(frequency(q)-frequency(q-1));
end
DF(q)=tgroup(q)/tgroupNG;
end
%
%subplot(2,1,1)
plot(lambda,T,'r--',lambda,R,'b-')
%subplot(2,1,2)
%plot(lambda,DF,'m-')
```

```
% This is an m-file that calculates the reflection and
transmission coefficients
% of a one-dimensional waveguide grating structure.  It can
be used to describe the
% propagation in a fibre or waveguide bragg grating
assuming that the guide is
% single-moded, and that the index profile reflects the
effective index for the
% propagating mode.
% THIS FILE is for cascaded, but non-phase-shifted
gratings.
% The number of sections is accepted
% as an input to the simulation, as is the number of
periods in each section.
% FOR MAXIMUM Generality, grating period and index
modulation in each section are
% also accepted as inputs to the simulation.
% THIS FILE ASSUMES A SQARE GRATING PROFILE, to shorten
simulation times.
% THIS FILE calculates field distributions.
% THIS FILE does NOT include absorption.
% THIS FILE calculates group delay.
%
%
% INPUT PARAMETERS provided to the simulation.
%
% n0=the effective modal index in the input region, to the
left of the grating.
n0=3.4598;
% nL=the effecitve modal index in the output region, right
of the grating.
nL=3.4598;
% mgrat=the number of constant phase grating sections.
mgrat=5;
% ngrat=a vector, with length mgrat, specifying the number
of periods in each
% grating section.
ngrat=[313 1200 313 1200 313];
% delgV=a vector describing the grating period in each
section
delgV=[224e-9 224e-9 224e-9 224e-9 224e-9];
% ng=base modal index in the grating region.
% dngV=vector for amplitude of the index modulation in each
grating section.
dngV=[0.01 0 0.01 0 0.01];
```

```
% kap=effective extinction coefficient
% lambda=input vector of free-space wavelengths
lambda=[1.548e-6:0.0001e-6:1.552e-6];
variZ=[4e-9 4e-9 4e-9 4e-9 4e-9];
%
% initialize data space
clear k0
clear Z
clear nz
clear zn
clear mpdet
clear mp11
clear mp12
clear mp21
clear mp22
clear Eplus
clear Eminu
clear r
clear t
clear R
clear T
clear A
clear tphase
clear tgroup
clear Epmag
clear Emmag
clear Itot
%
% generate vector of free-space propagation constants
k0=2.*pi./lambda;
% generate vector of frequencies
frequency=3e8./lambda;
%
% generate vector of aggregate length after each grating
section
%
Ltot=sum(ngrat.*delgV);
Ltg(1)=ngrat(1)*delgV(1);
for q=2:mgrat
Ltg(q)=Ltg(q-1)+ngrat(q)*delgV(q);
end
%
%
% generate vector of indices based on input index function
%
zn(1)=ngrat(1)*2;
for q=2:mgrat
```

```
zn(q)=ngrat(q)*2+zn(q-1);
end
%
% generate vector of coordinates
Z(1:zn(1))=0:delgV(1)/2:Ltg(1)-delgV(1)/2;
     for qq=1:zn(1)
     delzV(qq)=randn*variZ(1)+delgV(1)/2;
     end
for q=2:mgrat
Z(zn(q-1)+1:zn(q))=Ltg(q-1):delgV(q)/2:Ltg(q)-delgV(q)/2;
     for qq=zn(q-1)+1:zn(q)
     delzV(qq)=randn*variZ(q)+delgV(q)/2;
     end
end
%
ZL=length(Z);
ZQ=1:1:ZL;
%
% THIS FILE assumes a square grating profile.
ngb=n0;
nz(1:zn(1))=ngb-(dngV(1)/2).*(-1).^ZQ(1:zn(1));
for q=2:mgrat
nz(zn(q-1)+1:zn(q))=ngb-(dngV(q)/2).*(-1).^ZQ(zn(q-
1)+1:zn(q));
end
Nz=nz;
%
% create for-loop to run simulation at each point in vector
of wavelengths
Q=length(k0);
tstart=clock;
for q=1:Q
%
% calculate transfer matrix for the last layer and
interface
QZ=length(Z);
%
mgrating=[exp(i*k0(q)*Nz(QZ)*delzV(QZ)) 0; 0 exp(-
i*k0(q)*Nz(QZ)*delzV(QZ))]*(1/(2*Nz(QZ)))*[Nz(QZ)+nL
Nz(QZ)-nL; Nz(QZ)-nL Nz(QZ)+nL];
%
%mp11s(QZ)=mgratings(1,1);
%mp21s(QZ)=mgratings(2,1);
%
% calculate transfer matrix for grating structure
%
for qz=QZ-1:-1:2
```

```
mgrating=[exp(i*k0(q)*Nz(qz)*delzV(qz)) 0; 0 exp(-
i*k0(q)*Nz(qz)*delzV(qz))]*(1/(2*Nz(qz)))*[Nz(qz)+Nz(qz+1)
Nz(qz)-Nz(qz+1); Nz(qz)-Nz(qz+1) Nz(qz)+Nz(qz+1)]*mgrating;
%mp11s(qz)=mgratings(1,1);
%mp21s(qz)=mgratings(2,1);
end
%
% calculate transfer matrix for the first interface and
layer and interface
%
mgrating=(1/(2*n0))*[n0+Nz(1) n0-Nz(1); n0-Nz(1)
n0+Nz(1)]*[exp(i*k0(q)*Nz(1)*delzV(1)) 0; 0 exp(-
i*k0(q)*Nz(1)*delzV(1))]*(1/(2*Nz(1)))*[Nz(1)+Nz(2) Nz(1)-
Nz(2); Nz(1)-Nz(2) Nz(1)+Nz(2)]*mgrating;
%mp11s(1)=mgratings(1,1);
%mp21s(1)=mgratings(2,1);
%
% CALCULATE SIGNAL FIELD from transfer matrices
%for qq=1:QZ
%Epluss(qq)=(mp11s(qq)/mgratings(1,1))*Esin;
%Emins(qq)=(mp21s(qq)/mgratings(1,1))*Esin;
%Etots(qq)=Epluss(qq)+Emins(qq);
%Isig(qq)=0.5*3E8*8.85E-
12*nz(qq)*(abs(Epluss(qq))^2+abs(Emins(qq))^2);
%Sflux(qq)=Isig(qq)*sw/(6.626E-34*3E8);
%end
%
% calculate the field amplitudes as a function of position
%
%for qq=1:QZ
%Eplus(q,qq)=(1/mpdet(qq))*(mp22(qq)-
mp12(qq)*mgrating(2,1)/mgrating(1,1));
%Eminu(q,qq)=(1/mpdet(qq))*(-
mp21(qq)+mp11(qq)*mgrating(2,1)/mgrating(1,1));
%end
%Emmag=abs(Eminu);
%Epmag=abs(Eplus);
%Itot=Emmag.^2+Epmag.^2;
%
% calculate the overall amplitude reflection and
transmission coefficients
%
r(q)=mgrating(2,1)/mgrating(1,1);
t(q)=1/mgrating(1,1);
%
% calculate the power reflectivity and transmissivity
%
```

```
R(q)=r(q)*conj(r(q));
T(q)=t(q)*conj(t(q));
%
% calculate phase of transmitted wave at output plane
%
tphase(q)=atan(imag(t(q))/real(t(q)));
if real(t(q))<0
tphase(q)=tphase(q)+pi;
end
if real(t(q))>0
if imag(t(q))<0
tphase(q)=tphase(q)+2*pi;
end
end
%
percentdone=(q/Q)*100
timetonow=etime(clock,tstart)
end
%
% calculate group delay in transmission
%
tgroupNG=Ltot*n0/3e8;
tgroup(1)=-(1/(2*pi))*(tphase(2)-tphase(1))/(frequency(2)-
frequency(1));
if tgroup(1)<0
tgroup(1)=-(1/(2*pi))*(tphase(2)+(2*pi-
tphase(1)))/(frequency(2)-frequency(1));
end
DF(1)=tgroup(1)/tgroupNG;
for q=2:Q
tgroup(q)=-(1/(2*pi))*(tphase(q)-tphase(q-
1))/(frequency(q)-frequency(q-1));
if tgroup(q)<0
tgroup(q)=-(1/(2*pi))*(tphase(q)+(2*pi-tphase(q-
1)))/(frequency(q)-frequency(q-1));
end
DF(q)=tgroup(q)/tgroupNG;
end
%
%subplot(2,1,1)
plot(lambda,T,'c--',lambda,R,'b-')
%subplot(2,1,2)
%plot(lambda,DF,'m-')
```

Appendix – VI

Sample preparation for e-beam lithography

1. E-beam resist coating

The e-beam stage can hold only small samples of area 1 cm X 1 cm or smaller. Hence the SOI wafer with the patterned (optical lithography) alignment marks and waveguides were diced to fit inside the e-beam stage. As the length of the waveguides were 5 mm, the optically patterned SOI were diced to sizes of 5 mm X 5 mm with each diced sample consisting of a series of waveguides with different widths and different number of grating sections. Each of these samples was coated with an e-beam sensitive resist for exposure later. Poly Methyl MethAcrylate (PMMA), a positive resist, was used because of its high-resolution capabilities.

(a)   Sample cleaning

In order to get uniform coating of the resist in the region of exposure and to obtain consistency over the process, it is recommended that the samples be cleaned in Piranha (3 H_2SO_4 : 1 H_2O_2). The sample was left immersed in Piranha for ~30 minutes and then rinsed with de-ionized water. After drying the samples by blowing air, they were soft-baked in the oven for ~30 minutes at 125°C.

(b)   Resist coating

(i)   Single-resist layer

The cleaned samples were then loaded onto the resist spinner. A small vacuum chuck was fitted to the spinner to hold the samples during spinning. The cleaned sample was centrally placed on the chuck. The sample was covered with Isopropyl alcohol (IPA) and then spun to ensure a clean surface. A few drops of PMMA (950K C1) were then placed

on the sample and spun at a speed of 2000 rpm to achieve a resist thickness of 75 nm. After coating, sample is then post-baked at 180°C on a hotplate for 5 minutes for better adhesion to the substrate.

(ii)   Double-resist layer

As above, the samples were placed on the resist spinner and then cleaned with IPA. A 100 nm layer of 495K PMMA C2 was spun at a speed of 4000 rpm. It is then post-baked at 180°C on a hot plate for a longer time (20 minutes). Then a 950K PMMA C1 layer of 75 nm was spun on top of the 495K PMMA and then post-baked again for 15-20 minutes. The baking after spinning the first layer is very important because the second resist can dissolve and create an interfacial layer or destroy the first layer.